TU Delft

Delft University of Technology

Advanced Magnetocaloric Materials for Energy Conversion
Recent Progress, Opportunities, and Perspective

Zhang, Fengqi; Miao, Xuefei; van Dijk, Niels; Brück, Ekkes; Ren, Yang

DOI
10.1002/aenm.202400369

Publication date
2024

Document Version
Final published version

Published in
Advanced Energy Materials

Citation (APA)
Zhang, F., Miao, X., van Dijk, N., Brück, E., & Ren, Y. (in press). Advanced Magnetocaloric Materials for Energy Conversion: Recent Progress, Opportunities, and Perspective. *Advanced Energy Materials*, *14*(21), Article 2400369. https://doi.org/10.1002/aenm.202400369

Important note
To cite this publication, please use the final published version (if applicable).
Please check the document version above.

Copyright
Other than for strictly personal use, it is not permitted to download, forward or distribute the text or part of it, without the consent of the author(s) and/or copyright holder(s), unless the work is under an open content license such as Creative Commons.

Takedown policy
Please contact us and provide details if you believe this document breaches copyrights.
We will remove access to the work immediately and investigate your claim.

This work is downloaded from Delft University of Technology.
For technical reasons the number of authors shown on this cover page is limited to a maximum of 10.

Check for updates

ADVANCED ENERGY MATERIALS
www.advenergymat.de

Advanced Magnetocaloric Materials for Energy Conversion: Recent Progress, Opportunities, and Perspective

Fengqi Zhang, Xuefei Miao, Niels van Dijk, Ekkes Brück, and Yang Ren**

Solid-state caloric effects as intrinsic thermal responses to different physical external stimuli (magnetic-, uniaxial stress-, pressure-, and electric-fields) can achieve a higher energy efficiency compared with traditional gas compression techniques. Among these effects, magnetocaloric energy conversion is regarded as the best available alternative and has been exploited extensively for promising application scenarios in the last decades. This review systematically introduces the magnetocaloric effect and its applications, and summarizes the corresponding representative magnetocaloric materials, as well as important progress in recent years. Specifically, the review focuses on some key understandings of the magnetocaloric effect by utilizing state-of-the-art technical tools such as synchrotron *X*-ray, neutron scattering, muon spin spectroscopy, positron annihilation spectroscopy, high magnetic fields, etc., and highlights their importance toward advanced materials design and development. An overview of the basic principles and applications of these advanced techniques on magnetocaloric materials is provided. Finally, the challenges and perspectives on further developments in this field are discussed. Further in-depth understanding and manufacturing technology advancement combined with fast-developed artificial intelligence and machine learning are expected to advance the magnetocaloric energy conversion technology closer to real applications.

1. Introduction

Global warming and climate change pose a fundamental threat to human society and require urgent action to reduce carbon emissions. Technologies with a low energy efficiency need to be continuously eliminated or upgraded. Accordingly, more new sustainable energy concepts will emerge, which will result in an ever-increasing emphasis on efficiency improvement. Currently, almost a fifth of global electric energy spent relates to space cooling, and the radically rising demand for cooling consumes over 2000 terawatt hours (TWh) of electricity each year, which is 2.5 times the total electricity use of Africa.[1] One of the critical issues is that the widely used vapor-compression technique in heating-ventilation air-conditioning (HVAC) for heating or cooling has a low Carnot cycling energy efficiency, which varies enormously based on different production technologies. In particular, the 150-year-old vapor compression technology is energy intensive and reaches its efficiency limit. As shown in **Figure 1a**, one of the most important alternatives of this traditional technique is the magnetocaloric energy conversion, which is among the most efficient solid-state caloric conversion methods (together with elastocaloric ($E_{la}CE$), barocaloric (BCE), electrocaloric ($E_{le}CE$) and multicaloric ($M_{ul}CE$))[2] and the most developed so far. It can attain a substantially improved energy efficiency of more than 60%, while the best commercial vapor compressors can only achieve about 40% of Carnot efficiency.[3] In addition, as a still emerging sustainable technique, the magnetocaloric conversion is environmentally friendly because no hazardous refrigerants, like hydrofluorocarbons, are used during cycling. Considering the fact that heating and cooling contribute more than 40% of the global energy-related carbon dioxide emissions,[4] an improvement of 1% energy efficiency will save almost 2.2 million metric tons of carbon equivalent emissions.[5] Therefore the energy conversion technique based on solid-state magnetocaloric effect (MCE) is very promising and deserves to be considered seriously for carbon neutrality and decarbonizing the energy mix. It is worth mentioning that the European Union (EU) aims to achieve carbon neutrality by 2050 according to its "2050 long-term strategy",[6] and the Chinese government is committed to achieving carbon dioxide peaking by 2030 and carbon neutrality by 2060.[7]

As an intrinsic property of all magnetic materials, the MCE is the physical phenomenon where a magnetic material is heated or

F. Zhang, Y. Ren
Department of Physics
City University of Hong Kong
Kowloon, Hong Kong SAR China
E-mail: yangren@cityu.edu.hk
F. Zhang, N. van Dijk, E. Brück
Fundamental Aspects of Materials and Energy (FAME)
Faculty of Applied Sciences
Delft University of Technology
Mekelweg 15, Delft 2629JB, The Netherlands
E-mail: E.H.Bruck@tudelft.nl
X. Miao
MIIT Key Laboratory of Advanced Metallic and Intermetallic Materials Technology
School of Materials Science and Engineering
Nanjing University of Science and Technology
Nanjing 210094, China

The ORCID identification number(s) for the author(s) of this article can be found under https://doi.org/10.1002/aenm.202400369

DOI: 10.1002/aenm.202400369

 © 2024 Wiley-VCH GmbH

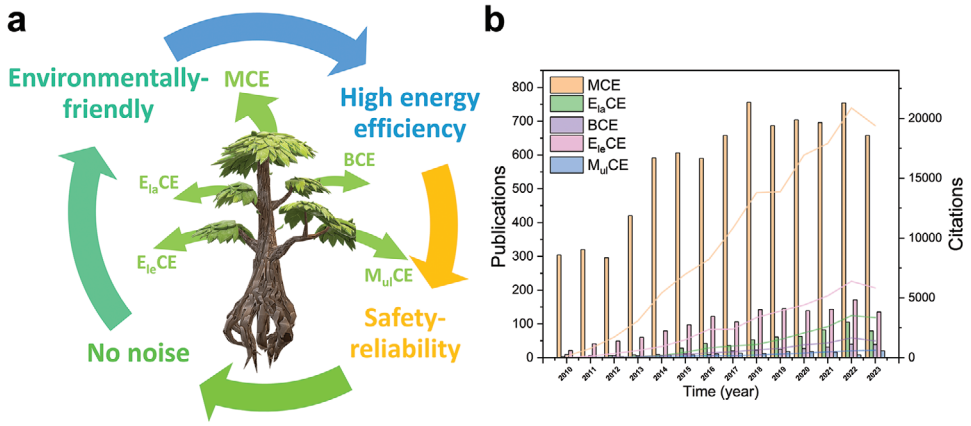

Figure 1. a) Typical solid-state caloric energy conversion including MCE, $E_{la}CE$, BCE, $E_{le}CE$, and $M_{ul}CE$, and its advantages compared with traditional vapor-compression technique. b) Research publications and citations (curves) for different caloric effects since 2010 (Data from Web of Science, February 2024). Note that the data for the last year are time-delayed.

cooled when an external magnetic field is applied or removed.[8,9] Based on this effect, several promising potential applications, such as magnetic refrigeration (cooling),[10–12] magnetocaloric heat pumps (cooling/heating),[13] and thermomagnetic generators for harvesting waste heat[14,15] have been proposed and further developed. Amongst these applications, the magnetic refrigeration technique has a relatively long history as it was first demonstrated almost 100 years ago.[16] For cryogenic applications, for instance, low-temperature cooling (below 1 K), Giauque and MacDougall have first reached a temperature of 0.25 K by demagnetizing the paramagnetic salt $Gd(SO_4)_3{\cdot}8H_2O$.[17] Experimental observations for the MCE started with Pierre Weiss and Auguste Piccard's work in 1917.[16] In their experiment, the magnetic field-induced heating effect had been noticed in ferromagnetic nickel around its Curie temperature ($T_C \approx 354$ °C). Simultaneously, theoretical investigations on adiabatic demagnetization at low temperatures had been proposed independently by Debye in 1926[18] and by Giauque in 1927.[19] Subsequently, the experimental realization of magnetic cooling was first reported by Giauque and MacDougall in 1933.[17] For this important accomplishment, Giauque received the 1949 Nobel Prize in Chemistry for his work on the thermodynamic properties of substances at low temperatures. As specifically mentioned during his presentation speech, magnetic cooling makes it possible to reach temperatures nearer to absolute zero than was possible by any earlier technique.[20] Room temperature applications were left aside until the 1970s, when Rare-Earth Gd-based prototypes were developed.[21,22] At the start of the 1990s there were sporadic, but influential studies that started to focus on magnetic cooling near room temperature, in systems like FeRh[23,24] and perovskite-type manganese oxide.[25] In Mn-perovskites[25] a large magnetic entropy change ($|\Delta s_m|$) of 5.5 J kg^{-1} K^{-1} was observed with an applied magnetic field change ($\Delta\varepsilon_0 H$) of 1.5 T at 230 K. It was pointed out that this candidate material could be suitable for magnetic refrigeration near room temperature. In the same year the breakthrough in this field came by the pioneering work on the giant magnetocaloric effect (GMCE), first proposed by Pecharsky et al., near room temperature in the $Gd_5(Si_2Ge_2)$ material.[10,26] Due to the stronger first-order magnetostructural coupling of the phase transition (orthorhombic-to-monoclinic structural transition coupled with magnetic transition) the $|\Delta s_m|$ of $Gd_5(Si_2Ge_2)$ can reach 18.5 J kg^{-1} K^{-1} for a field change of $\Delta\varepsilon_0 H = 5$ T at 276 K. Surprisingly, the strong first-order magnetic transition (FOMT) is close to reversible because of the very low thermal hysteresis ($\Delta T_{hys} = 2$ K). More historical details related to the MCE and room-temperature magnetic cooling can be found in.[27,28] Numerous FOMT magnetocaloric materials (MCMs) that demonstrate a GMCE have sprung up, including $(Mn,Fe)_2(P,X)$-based compounds (X = As, Ge, Si),[11] $La(Fe,Si)_{13}$-based materials,[12,29] Ni-Mn-X-based magnetic Heusler compounds (X = Ga, In, Sn, Sb)[30,31] and Mn-M-X (M = Co, Ni and X = Si, Ge) compounds.[32,33] In the last 25 years a continuously growing interest has resulted in growing efforts to search for MCMs with a FOMT. As presented in Figure 1b, the total number of research publications and citations referring to the term "magnetocaloric" have shown a continuous growth during the last 10 years, together with other emerging caloric effects like $E_{la}CE$, BCE, $E_{le}CE$, and $M_{ul}CE$. These solid-state caloric energy conversions have exceptional advantages such as higher energy efficiency, environmental friendliness, no noise, and safety, in comparison to gas compression. Among them, the MCE obtained considerable momentum. The rapid development of these research activities is motivated by the potential use of magnetic-field driven cooling/heating near room temperature with solid-state working materials for future solid-state gas-free cooling/heating engines. Next to MCE, also $E_{la}CE$ and BCE display large thermal changes, in response to mechanical stress or pressure. Giant $E_{la}CE$ is limited so far to shape-memory alloys with huge shear strain. Often the reversibility of the response for both $E_{la}CE$ and BCE needs further improvement. On the other hand, for $E_{le}CE$ avoiding electrical breakdown is challenging.[34] Finally, for $M_{ul}CE$ hysteresis and fatigue seem to be key issues for implementing materials into devices.[35]

Previous review papers focused on fundamental material research associated with MCE and other caloric effects,[9,34,36–38] thermodynamics perspectives,[3,39] prototypes, and manufacturing.[28,40] The present review presents recent cutting-edge progress in experiments and advanced characterization studies in this field not summarized until now. In this

© 2024 Wiley-VCH GmbH

16146840, 0, Downloaded from https://onlinelibrary.wiley.com/doi/10.1002/aenm.202400369 by Tu Delft, Wiley Online Library on [08/04/2024]. See the Terms and Conditions (https://onlinelibrary.wiley.com/terms-and-conditions) on Wiley Online Library for rules of use; OA articles are governed by the applicable Creative Commons License

Table 1. Comparison among different emerging refrigeration technologies including MC, $E_{la}C$, BC, $E_{le}C$, $M_{ul}C$, TE, SA, and acoustic refrigeration.[41–45]

Refrigeration type	MC	$E_{la}C$	BC	$E_{le}C$	$M_{ul}C$	TE	SA	Acoustic
Working force	Magnetic field	Uniaxial stress	Hydrostatic pressure	Electric field	Multiple fields	Electric field	Heat	Sound waves
Advantages	High energy efficiency; environmentally friendly; no noise; safety reliability; potential for large-scale applications	High cooling capacity; potential for compact and lightweight designs; high energy efficiency	Wide availability (general to all atomic systems); potentially high cooling efficiency; environmentally friendly; potential for miniaturization	High cooling efficiency; potential for small-scale/flexible applications; environmentally friendly; fast response time	Possibilities of enhancing thermal properties, operating temperature; reducing the field hysteresis; reducing the driving force	Compact and solid-state design; no moving parts; long lifespan; potential for small-scale/portable applications	Environmentally friendly; no vibrations; no moving parts; fewer corrosion issues; suitable for off-grid applications	Long lifespan; simple and reliable
Disadvantages	Requires strong and efficient magnetic materials; needs a reliable and efficient magnetic field source	Limited availability of suitable SMAs[a]; still very high stress; durability issues	Fatigue lifetime; challenges in achieving high pressure changes; system complexity	Limited availability of suitable dielectric materials; challenges in achieving high electric field changes; system complexity	System complexity; difficulty in obtaining experimental data	Limited efficiency compared to traditional cooling; relatively low cooling capacity; high cost	Low efficiency COP[b]; high manufacturing expenses; affected by ambient temperature and solar availability	Lower thermal efficiency; low cooling capacity; requires specific gas properties and acoustic resonators

[a] SMAs, shape memory alloys; [b] COP, coefficient of performance.

review, we comprehensively emphasize the recent advances (2013–2023) in advanced MCMs and outline the timelines of these developments. Particularly, we highlight the importance of multimodal studies by applying advanced characterization facilities for the research development of MCMs. The review is organized as follows: first, a brief introduction about magnetocaloric energy conversion is presented including: i) solid-state magnetic refrigeration; ii) Magnetic heat pump; iii) thermomagnetic generator; iv) other energy conversion methods and applications. Then, in the second part, on the basis of magnetoelastic and magnetostructural coupling strategies (coupling with different degrees of freedom among which the lattice, magnetism, and electrons), the recent experimental progress associated with first-order transition materials are reviewed, in particular the $(Mn,Fe)_2(P,Si)$-based, $La(Fe,Si)_{13}$-based, NiMn-based magnetic Heusler compounds and magnetocaloric high-entropy alloys. The recent research in magnetocaloric conversion indicates that it possesses a promising future position in the market share.[28] Therefore, with further developing advanced characterization facilities, special emphasis will be dedicated to a deeper understanding of the combinatory use of these versatile tools such as: i) synchrotron X-ray techniques; ii) neutron scattering; iii) muon spin spectroscopy; iv) positron annihilation spectroscopy; v) high magnetic fields. We aim to provide the necessary overview and guidelines for researchers in this field to properly choose suitable characterization methods to capture the key information underlying the physical mechanism. Finally, the current major challenges towards real widespread commercialization are addressed, as well as the opening opportunities for magnetocaloric energy conversion. The future perspectives for the development of advanced MCMs are presented.

2. Promising Applications of MCMs

2.1. Solid-State Magnetic Refrigeration (MR)

The world is facing a looming "cold crunch"[1] and the air-conditioning is booming. In this background, the solid-state MR near room temperature catches considerable attention and develops steadily to substitute the current outdated cooling technique, which is responsible for 40% of the total growth in building electricity demands.[1] Together with magnetocaloric (MC) refrigeration, the different emerging refrigeration technologies including elastocaloric ($E_{la}C$) refrigeration, barocaloric (BC) refrigeration, electrocaloric ($E_{le}C$) refrigeration, multicaloric ($M_{ul}C$) refrigeration, thermoelectric (TE) refrigeration, solar adsorption (SA) refrigeration, and acoustic refrigeration are listed in **Table 1**.

In **Figure 2**, a schematic diagram of the magnetocaloric cycle is demonstrated. During the full cycling, accompanied by the magnetization and demagnetization processes, the heat (Q) is continuously removed from the region of interest by MCMs and transferred through a suitable heat transfer fluid. Two pivotal performance parameters to evaluate the MCMs: the isothermal magnetic entropy change Δs_m and the adiabatic temperature change ΔT_{ad}, which can be calculated from different indirect and direct methods. These methods have been systematically introduced in other recent reviews.[3,9] Nowadays the most frequently used (indirect) way to estimate Δs_m and ΔT_{ad} is based on one of the Maxwell relations, resulting in $\Delta s_m(T,\Delta H) = \int_0^H \left(\frac{\partial M}{\partial T}\right)_H d\mu_0 H$ and $\Delta T_{ad}(T,\Delta H) = -\int_0^H \frac{T}{C_p}\left(\frac{\partial M}{\partial T}\right)_H d\mu_0 H$,[9] where T is temperature, H the magnetic field, ε_0 the permeability of vacuum, and C_p the heat capacity. However, data obtained from direct measurements are required to accurately comprehend the dynamic

© 2024 Wiley-VCH GmbH

16146840, 0, Downloaded from https://onlinelibrary.wiley.com/doi/10.1002/aenm.202400369 by Tu Delft, Wiley Online Library on [08/04/2024]. See the Terms and Conditions (https://onlinelibrary.wiley.com/terms-and-conditions) on Wiley Online Library for rules of use; OA articles are governed by the applicable Creative Commons License

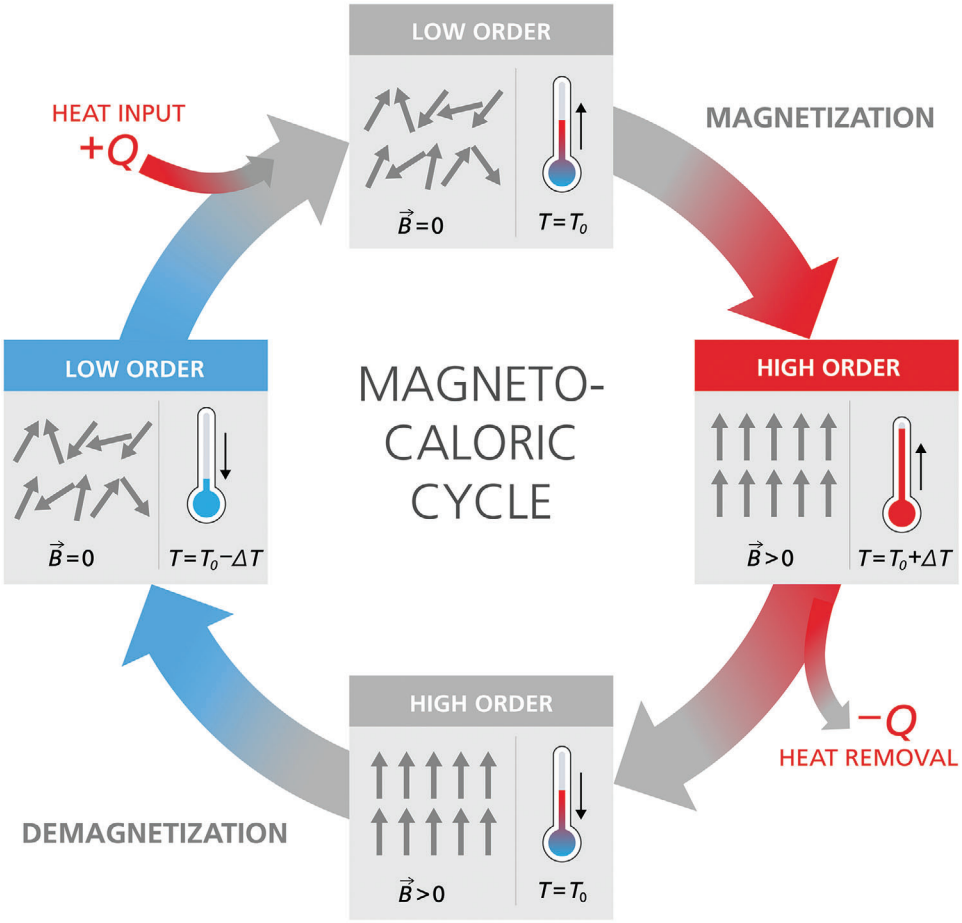

Figure 2. Schematic diagram of the magnetocaloric cycle. Reproduced with permission.[46] Copyright 2024, Fraunhofer IPM. In brief, when the MCMs with low magnetic ordering are adiabatically magnetized, the magnetic ordering is enhanced and the field-driven magnetic entropy decreases and the temperature increases; after that, the material returns to its initial temperature after heat removal (–*Q*) by a suitable heat transfer fluid; then after the material is adiabatically demagnetized, the magnetic ordering is reduced, and the temperature will decrease followed by heat input (+*Q*).

magnetocaloric properties associated with the MCMs, when the MR prototypes are applied.

Currently, the most promising magnetocaloric prototype refrigerators with a wide temperature span remain based on active magnetic regenerative (AMR) refrigeration (compared with passive regeneration),[39] therefore recent advances about MR will be offered in this direction. In recent years, several companies (like Cooltech Applications (currently known as Magnoric), General Electric (GE), Vacuumschmelze, BASF, Haier, Magnotherm, Magneto, and others) and different universities/institutes from Europe, the United States, China, Japan, and Brazil have been actively involved in the development of cold-storage devices based on MR technology.[47] For example, in 2014, GE declared that they had developed a silent MR refrigerator that could cool a bottle of beer.[48] And in 2015, in collaboration with Astronautics, BASF, and TU Delft, Haier exhibited a proof-of-concept wine cooler without a compressor at the International Consumer Electronics Show in Las Vegas.[49] Meanwhile, Cooltech Applications exhibited a commercial magnetocaloric refrigerator (MRS400), which boasts 400 W of cooling power and maintains an internal temperature between 2 and 5 °C.[50] The potential application scenarios can be in refrigerated retail displays, wine cellars, and medical facilities. In addition, in 2021 Sergiu Lionte et al. demonstrated an MR prototype equipped with more than 20 °C temperature span, about 15 kW cooling power, and about 60% Carnot COP.[51] It is claimed that it will be used for large industrial processes. The achieved very good performance is believed to be a milestone for the future of magnetocaloric coolers. Furthermore, Barbosa et al.[52] developed a magnetic wine cooler prototype (2021), which can simultaneously refrigerate up to 31 bottles of wine (10.8–25 °C). Soon after in 2023, the arrival of a magnetocaloric air-conditioning system prototype with 490 W cooling capacity and 16.8 °C temperature span was reported.[53] In the past decades, the prototype development in MR has been boosted, and has made significant advances that benefited from the close collaboration between material scientists and engineers.[40,54] Nonetheless, practical challenges such as further improving cooling capacity, enhancing system efficiency, and ensuring reliability should be addressed by optimizing the design of prototype systems (including the magnetic field utilization, heat transfer, simple design, high frequency, thermal span, and thermal management).[36] Additionally, combining advanced processing technologies such as additive manufacturing, the optimization of MCMs (like $(Mn,Fe)_2(P,Si)$, $La(FeSi)_{13}$, and

© 2024 Wiley-VCH GmbH

16146840, 0, Downloaded from https://onlinelibrary.wiley.com/doi/10.1002/aenm.202400369 by Tu Delft, Wiley Online Library on [08/04/2024]. See the Terms and Conditions (https://onlinelibrary.wiley.com/terms-and-conditions) on Wiley Online Library for rules of use; OA articles are governed by the applicable Creative Commons License

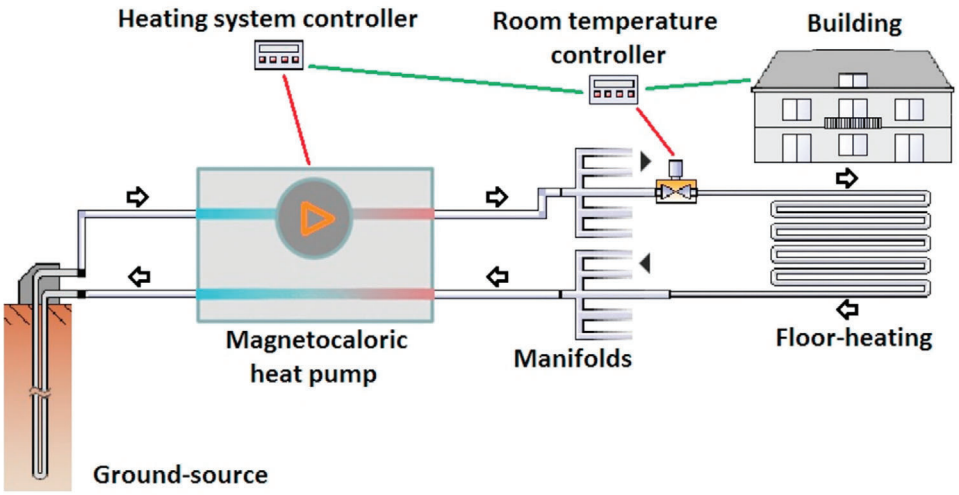

Figure 3. A demonstration of the integrated magnetic HP in single hydraulic loop with ground source heat exchanger and under-floor heating system. Reproduced with permission.[13] Copyright 2019, Elsevier.

NiMn-based Heusler compounds) is expected to achieve an optimal cooling performance in future prototypes.

In conclusion, magnetic refrigeration prototype development has made significant progress in recent years, showcasing the potential of this technology as a sustainable and efficient cooling solution. Continued efforts in research and development are expected to bring MR closer to commercialization and widespread adoption in the future.

2.2. Magnetocaloric Heat Pump (MHP)

The MHP is an emerging technology that utilizes the MCE to pump heat from a low-temperature source to a high-temperature sink. As a promising alternative to traditional gas-compression heat pump systems, the MHP can offer a heating and cooling solution with higher energy efficiency and environmental friendliness. It is worth mentioning that the MHP shares the same magnetocaloric cycle with MR, as presented in Figure 1. Compared with MR, which only focuses on cooling, however, the MHP can provide both heating and cooling protocols depending on the demand. For example, it can transfer heat from a low temperature to a high temperature for cooling purposes, and it can also reverse the process of transporting heat from a low-temperature source to a high-temperature sink for heating purposes. The MHP can provide versatility for broad applications in residential/commercial/industrial settings for HVAC systems, space warming, and water heating. As shown in **Figure 3**, Johra et al.[13,55] designed a ground source MHP system to provide the heating requirements of a building by integrating the MHP in a single hydraulic loop with a ground source heat exchanger (GSHE) and a floor heating system. Note that the GSHE is crucial to minimize the temperature span between the heat source and heat sink and is beneficial for a high COP of the heat pump systems.[55] The unique configuration endows the system without an intermediate heat exchanger or hot water storage tank, and the addition of a MHP can further simplify the piping network and reduce heat losses, as compared with the conventional ground source heat pump system, that requires two water to refrigerant heat-exchangers.[55] The developed rotary AMR MHP (which is named MagQueen and uses $La(Fe,Mn,Si)_{13}H_y$ as MCM) by Dall'Olio et al.[56] is capable of providing a heating power of 950 W at a temperature span of 5.6 K and a cycle frequency of 1.2 Hz. The heating COP ranges from 6.7 to 1.4 for temperature spans between 10.3 and 15.7 K at a frequency of 0.5 Hz. In addition, recently Quijano et al.[57] applied a 1D numerical model to study the performance of layered AMRs composed of $(Mn,Fe)_2(P,Si)$ materials arranged in three different layering strategies for the MHP. It is expected to pave the way for the application of $(Mn,Fe)_2(P,Si)$ MCMs in a real MHP prototype in the near future.[58] Simultaneously, by the current wave of electrification, the MHP system can also be inserted into some mobile scenarios like electric vehicles (EV).[59,60] For instance, Torregrosa-Jaime et al. designed an innovative air-conditioning system for an electric minibus, and the studies provide an output power reference for a MHP in the electric minibus (1.60 kW of cooling power over a span of 37 K; 3.39 kW of heating power over a span of 40 K).[60] Even so, similar to the development of MR, the commercialization of efficient MHP still faces challenges with respect to the design of the device (magnetic field source, magnetic circuit, regenerator bed geometry, heat exchangers, pumping system, etc.), the prevention of performance loss (housing heat leaks, dead volume losses, etc.) and the optimization of MCMs.[61–63]

2.3. Thermomagnetic Generator (TMG)

Globally, it is estimated that over 60% of all energy produced is rejected as waste heat. Within that, the low-grade waste heat (below 500 K) accounts for about 65% of the total waste heat.[64] What's worse is that this low-grade waste heat is usually difficult to recover because of the recycling technologies with low Carnot energy efficiencies. For instance, the conversion efficiency of thermoelectric generator, based on the Seebeck effect, will reduce significantly with the decrease of temperature difference (COP below 0.5 with 20 K span).[65] Therefore, it is important to

© 2024 Wiley-VCH GmbH

16146840, 0, Downloaded from https://onlinelibrary.wiley.com/doi/10.1002/aenm.202400369 by Tu Delft, Wiley Online Library on [08/04/2024]. See the Terms and Conditions (https://onlinelibrary.wiley.com/terms-and-conditions) on Wiley Online Library for rules of use; OA articles are governed by the applicable Creative Commons License

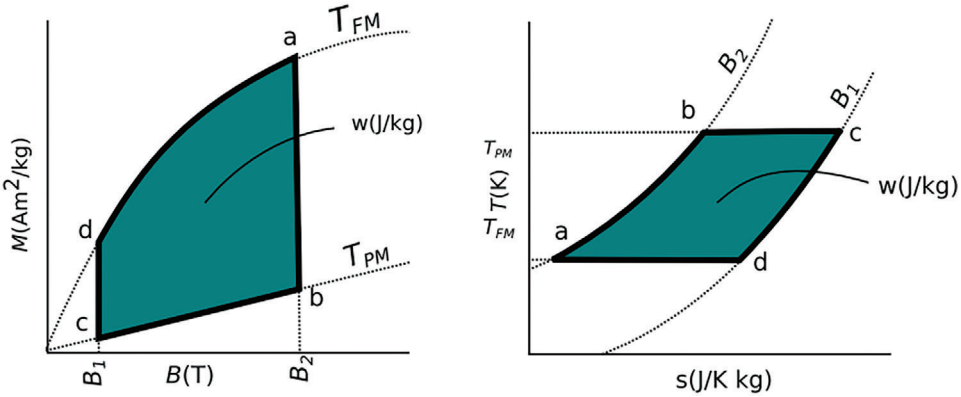

Figure 4. Idealized work cycle for the TMG: (left). An *M-B* diagram; (right). An *s-T* diagram. Reproduced with permission.[73] Copyright 2014, Elsevier.

further develop other solid-state technologies, i.e., TMG, to convert low-grade waste heat into other sustainable energy forms such as electricity. Currently, the efficiency of the TMG is still in an embryonic stage and needs to be improved further.[15]

The idea of thermomagnetic generation was originally proposed in the late 19th century by Edison,[66,67] Stefan,[68] and Tesla[69,70] and was then analytically revisited in 1948 by Brillouin and Iskenderian.[71] They derived that the theoretical conversion efficiency of TMG can even reach 55–75% of the Carnot efficiency.[71,72] The basic principle behind the TMG is to properly exploit the Faraday law of electromagnetic induction when materials cross the thermally driven magnetic phase transition.[73] The active materials used for the TMG prototype preferentially show a metamagnetic transition from a high magnetic-ordering state (i.e., ferromagnetic (FM)) to a low magnetic-ordering state (i.e., paramagnetic (PM)) to obtain a considerable change in magnetization (ΔM). For example, as present in **Figure 4**, the thermomagnetic cycle can be described in a regenerative Ericsson cycle (including two iso-thermal and two iso-field processes) from two ways (*M-B* or *s-T* diagram), where B is the external applied magnetic field ($\varepsilon_0 H$), s the specific entropy, T the temperature, and w the work done. The thermodynamic efficiency of TMG can be determined as the ratio of the output energy (the upper limit of magnetic work E_m) to the heat input (Q_{in}) for each cycle. Consequently, the thermomagnetic material efficiency (η) can be expressed as follows:[74]

$$\eta = \frac{E_m}{Q_{in}} = \frac{\mu_0 \int HdM}{Q_{in}} = \frac{\mu_0 \Delta M H}{\rho \int_{T_c}^{T_h} C_p dT} \quad (1)$$

where $\mu_0 H$ is the applied magnetic field, ρ density, T_c cooling temperature, T_h heating temperature, and C_p specific heat capacity. It is indicated that as a good criterion, the potential material candidates should have high $\frac{\Delta M}{\Delta Q}$ values. Besides this, the thermomagnetic materials (TMMs) should generally have the following properties such as i) soft magnetic materials with a low remnant magnetization; ii) adjustable T_C; iii) high thermal conductivity; iv) low-cost and non-toxicity; and v) low content of critical components.

Different TMMs have been designed and tested in a variety of different TMG devices including $3d/4f$ pure metals (Co, Fe, Ni, Gd, Tb, Dy, Ho, Er),[75–78] $(Mn,Fe)_2(P,As)$,[73] NiMn-based Heusler films,[14,79–81] $Gd_5(Si,Ge)_4$,[81] and $La(Fe,Si)_{13}$[15,81–83] compounds. Recent progress in the development of TMMs/devices is summarized below:

In 2014, Christiaanse and Brück demonstrated a proof-of-concept static TMG experimental device based on $(Mn,Fe)_2(P,As)$ material.[73] The active part of the generator consists of 48 disks of TMMs with different T_C (300, 304, 307, 310 K), and the magnetic field source was formed by a NdFeB permanent magnet. The maximum average output power was ≈0.048 mW. Fries and co-workers[84] investigated the thermomagnetic properties of refractory MnB with its pseudo-binary derivatives ($Mn_{1-x}Co_xB$ and $Mn_{1-x}Fe_xB$). The MnB compound shows a magnetization of $M = 156$ A m^2 kg^{-1} and a sharp FM to PM phase transition (without hysteresis loss) at $T_C = 567$ K. And it is reported that these materials show an iso-structural magnetoelastic effect that is easily tunable T_C (200–800 K), which is beneficial for TMG applications. In 2016, Gueltig et al.[14] exhibited an efficient thermomagnetic generation via resonant actuation of a Ni–Mn–Ga Heusler film and the device can generate an unprecedented power density of 118 mW cm^{-3}, which can compete with the best thermoelectric generators. Due to the large temperature-dependent ΔM of the films, a periodic temperature change of only 3 K is required for operation. As presented in **Figure 5a–f**, in 2018 Waske et al.[15] designed a TMG demonstrator that can improve the performance of TMG devices by orders of magnitude by introducing an appropriate topology for the magnetic circuit. Combining their experimental and modeling results, it was shown that the configuration can efficiently avoid some drawbacks of previous designs, like magnetic stray fields, hysteresis, and complex geometries of the TMMs. However, the maximum relative Carnot efficiency of TMG is not high and only reaches 1.7×10^{-3}%. In a subsequent work in 2020,[79] Joseph et al. address the key question of how the film thickness and device footprint affect power and efficiency for the Ni–Mn–Ga Heusler film-based TMG device. They studied the scaling performance of the heat intake, heat dissipation, and local temperature changes. Their results show that the electrical power per footprint can be significantly enhanced by 3.4 times when increasing the film thickness from 5 to 40 εm. Their TMG device can achieve 50 mW cm^2 as the maximum value of electrical power per footprint at a temperature change of only 3 K. Additionally, Dzekan et al.[85] built a TMMs

© 2024 Wiley-VCH GmbH

16146840, 0, Downloaded from https://onlinelibrary.wiley.com/doi/10.1002/aenm.202400369 by Tu Delft, Wiley Online Library on [08/04/2024]. See the Terms and Conditions (https://onlinelibrary.wiley.com/terms-and-conditions) on Wiley Online Library for rules of use; OA articles are governed by the applicable Creative Commons License

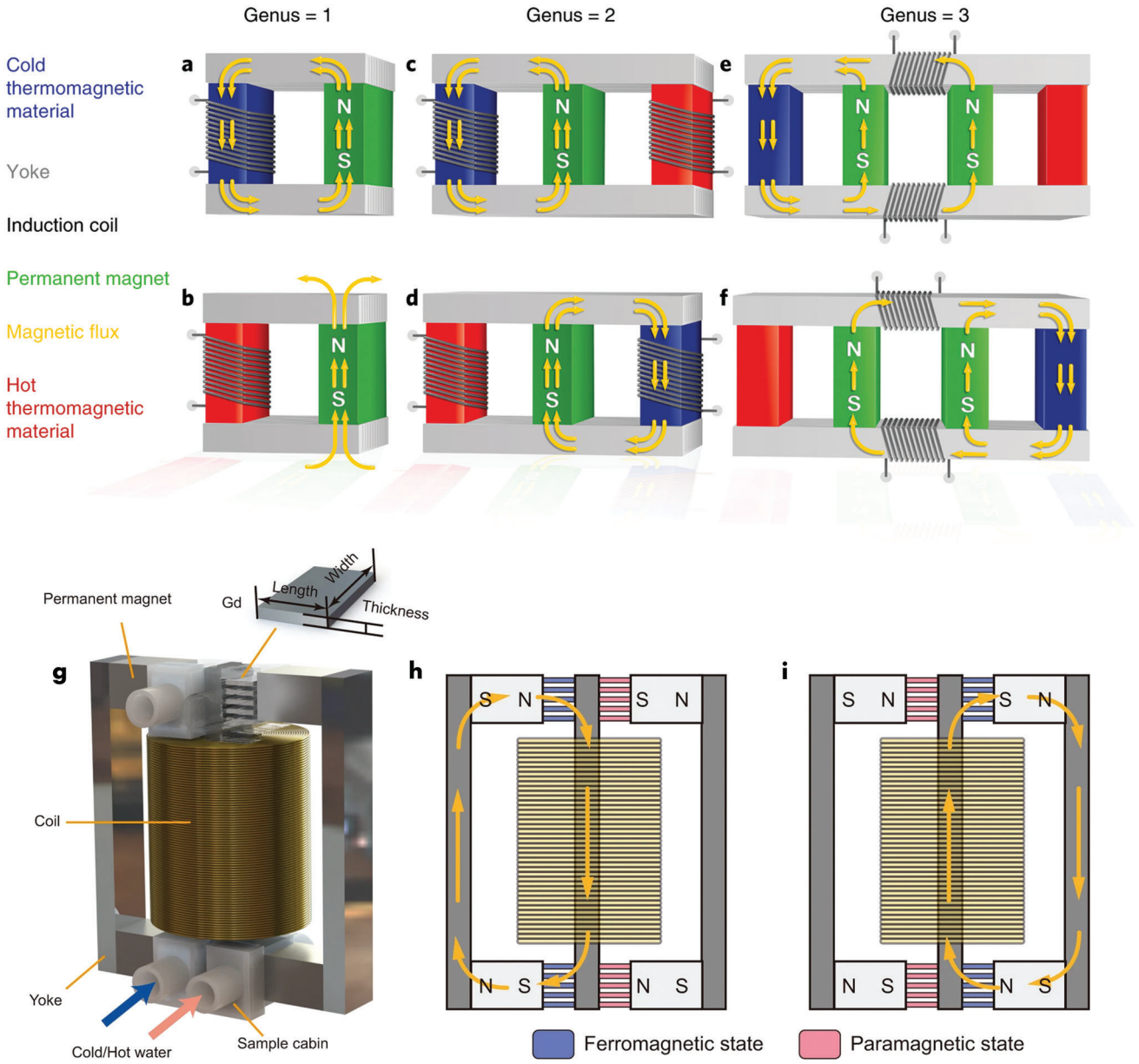

Figure 5. Different configurations of magnetic circuits of TMGs.[15,86] a) For genus = 1 in the low-temperature state, the complete flux is guided in a single circle. b) When the TMMs warm up (PM), no flux through the TMMs. c,d) For genus = 2 with only one permanent magnet but two sets of TMMs, which alternatively close the magnetic flux through them. e,f) For genus = 3, two permanent magnets are used, which allows a sign reversal of the magnetic flux within the connecting yokes when changing the temperatures of TMMs. This configuration doubles the flux change, avoids hysteresis within the yokes and realizes an easier heat exchange between the TMMs and the fluid. a–f) Reproduced with permission. Copyright 2019, Springer Nature. (g) Detailed schematic illustration of another magnetic circuit configuration. h,i) Working principle during cycling. Blue means that the TMMs are in low-temperature FM, and red means high-temperature PM. The direction of the magnetic flux in the magnetic circuit will be reversed accompanying alternating cold and hot sides of TMMs. g–i) Reproduced under the terms of the CC BY license. Copyright 2023, Author(s).

library and evaluated the potential of various TMMs in terms of efficiency and cost-effectiveness for use in motors, oscillators, and generators for converting waste heat into electricity. The conclusions suggest that the best TMMs can compete with thermoelectric materials for temperature differences up to several times 10 K. Moreover, Chen et al.[81] compared the performance of a TMG device employing different TMMs such as Gd, $Gd_5(Si,Ge)_4$, NiCoMnSn Heusler alloy, and $La(Fe,Si)_{13}H_y$/In composite. It is found that the $La(Fe, Si)_{13}H_y$/In composite exhibited the highest induced current (9.12 εA g^{-1}) and power density (0.47 mW m^{-3}). Consequently, they conclude that the $La(Fe,Si)_{13}H_y$/In composite is promising for harvesting low-grade waste heat. Recently, Liu et al.[86] designed a TMG device with a new configuration for low-temperature waste heat recovery. Different from previous TMG designs, as demonstrated in Figure 5g–i, in this new device the TMMs (Gd plates or $La(Fe,Si)_{13}H_y$/In composites) can

© 2024 Wiley-VCH GmbH

16146840, 0, Downloaded from https://onlinelibrary.wiley.com/doi/10.1002/aenm.202400369 by Tu Delft, Wiley Online Library on [08/04/2024]. See the Terms and Conditions (https://onlinelibrary.wiley.com/terms-and-conditions) on Wiley Online Library for rules of use; OA articles are governed by the applicable Creative Commons License

control the on/off of the magnetic circuit like a switch because of the temperature-dependent FM to PM transition. The optimized integration makes the magnetic flux in the induction coil change between the negative and positive maximum values, resulting in the enhancement of an induced average power ranging from 0.04 to 0.19 V. Simultaneously, a lower magnetic stray field and a lower amount of TMM (less economic cost because of rare-earth La element) has been achieved in this TMG device. This study also shed light on the fact that a higher TMG performance can be obtained by properly constructing the magnetic circuit with TMMs. Interestingly, to prove the function of their TMG device, the authors successfully lit up an LED light and it is proposed the TMG array can well convert the low-grade waste heat into electricity. So far, some progress has been made, however, there are still great challenges associated with TMG, e.g., low power density, low conversion efficiency, and lacking enough candidate materials to cover low-grade waste heat temperature window. The TMG is still in the research and development stage, and its commercial applications are currently limited. However, ongoing advancements in magnetic materials, system design, and optimization techniques hold promise for the future of TMG.

2.4. Other Applications

In addition to the promising applications discussed above, another application of the MCE is the cryogenic liquefaction of gases, which can act as energy storage media. It is known that the traditional methods of gas liquefaction can be energy-intensive and expensive, while using the MCE-based AMR could potentially be more efficient and cost-effective.[87,88] Based on specific conditions, different gases with high economic value, such as hydrogen (H_2 liquefaction temperature is 20 K), nitrogen (N_2, 77 K), oxygen (O_2, 90 K), natural gas (CH_4, 112 K at 0.1 MPa; 190 K at 4.5 MPa), propane (C_3H_8, 231 K), and air, can be sufficiently liquified at low temperature.[89–95] For example, Archipley et al. report a prototype of an active magnetic regenerative refrigerator to liquefy methane with a high-field superconducting magnet, and they can successfully liquefy pure methane with their liquefier by cooling from 285 to 135 K.[93] Barclay et al. investigated how a Gd-based AMR-cycle refrigerator moving through field changes of 2.7 T at 0.25 Hz was used to liquefy pure propane at two different supply pressures.[94] The EU project "HyLICAL" (2022–2027) will develop and validate a new magnetocaloric high-performance hydrogen liquefier prototype.[96] From a material science perspective, Terada and Mamiya recently reported that the rare-earth single metal holmium (Ho) can exhibit a GMCE in a magnetic field lower than 1 T for temperatures ranging from 20 to 50 K.[89] And Guillou et al. found a rare-earth intermetallic, Eu_2In, which shows a FOMT with a strong magnetoelastic coupling, but negligible hysteresis. This compound presents an excellent MCE performance at practical magnetic fields (<2 T), e.g., the maximum Δs_m values are −24.4 and −28.2 J kg^{-1} K^{-1} for $\Delta\mu_0 H$ of 1 and 2 T (the corresponding ΔT_{ad} are 2.2 and 5.0 K). It is proposed that Eu_2In outperforms all known MCMs in this temperature range and could be promising for N_2 liquefaction.[91]

Moreover, these solid-state phase change materials (PCMs), either with a strong magnetoelastic or magnetostructural coupling, have a great potential for a variety of thermal storage applications taking advantage of their latent heat storage properties employing a solid-solid transition.[97–100] For instance, it was introduced that PCMs with a phase change temperature greater than 200 °C can be applied in large-scale concentrated solar power (CSP) and pumped heat electrical storage plants, which are known as Carnot batteries.[101] And the PCMs provide another solution for future thermal energy storage. Similar thermal storage battery concepts have occurred in other caloric properties. Zhang et al. developed thermal batteries utilizing the strong pressure-driven first-order solid-solid transition based on BCE.[102] Furthermore, inspired by the quick thermal response of PCMs, devices like magnetocaloric heat switches can be designed.[103–106] In addition, the magnetocaloric conversion can be a useful complement to other techniques. For example, Han et al.[107] reported a solar MR seawater desalting device where solar energy can combine with the MR technology. In this device, the solar energy evaporates seawater and generates steam, while the MR manipulates and condenses the steam into fresh water. It is expected that magnetocaloric conversion will be coupled with other renewable energy sources (e.g., biomass energy) in the future.[47]

As main-stream technique of energy storage, however, Li-ion battery cells are temperature-sensitive devices and a stable working temperature is vital. Arora reviewed different emerging alternatives for traditional thermal management techniques of Li-ion batteries, including MR.[108] Al-Nimr et al. investigated how MR integrates with the thermal management of rechargeable batteries in EV by modeling.[109] An EU project ("Cool BatMan")[110] is dedicated to develop a compact and hybrid magnetocaloric cooling proof-of-principle suitable for integration as a battery thermal management system for Li-ion batteries in *e*-mobility. The interest in the functionality of MCE has been further extended to magnetocaloric-based wearable thermal management devices.[111] Last but not least, although extensive research activities have focused on the applications of bulk MCMs, the materials at lower dimensions like nanoscale are also promising in some fields such as micro-refrigerators, thermal switches, microfluidic pumps, energy harvesting devices, and biomedical applications (magnetic hyperthermia or drug delivery).[112,113] A good example may be that magnetic ferrofluid materials can be practically applied to design a micro-scale pumping system for cooling/heating.[114–118] Interestingly, the MCE can be also regarded as a sensor (as well as other caloric effects[119]) to determine the entropy landscape of the phase formation associated with quantum criticality and establish the phase diagram of unconventional superconductors[120] and has extended its applications in quantum materials.[121]

3. Critical Magnetocaloric Materials

In the past 2 decades, numerous first-order magnetic transition (FOMT) plus strong second-order magnetic transition (SOMT) MCMs that demonstrate a GMCE have sprung up, including $Gd_5(Si_2Ge_2)$,[10] $(Mn,Fe)_2(P,X)$-based compounds (X = As, Ge, Si),[11] $La(Fe,Si)_{13}$-based materials,[12,29] NiMn-X based magnetic Heusler compounds (X = Ga, In, Sn, Sb)[30] with as a special case the so-called all-*d*-metal NiCoMnTi,[122] FeRh,[123] Mn_2Sb based alloys,[124] Mn-M-X (M = Co, Ni and X = Si, Ge) alloys[32,33] and magnetocaloric high-entropy alloys (MHEAs).[125] These materials demonstrate a strong FOMT with a discontinuous change

© 2024 Wiley-VCH GmbH

16146840, 0, Downloaded from https://onlinelibrary.wiley.com/doi/10.1002/aenm.202400369 by Tu Delft, Wiley Online Library on [08/04/2024]. See the Terms and Conditions (https://onlinelibrary.wiley.com/terms-and-conditions) on Wiley Online Library for rules of use; OA articles are governed by the applicable Creative Commons License

in the first derivative of the Gibbs free energy resulting from the coupling between the magnetic and crystal lattice degrees of freedom in the form of a magnetoelastic (ME) or magnetostructural (MS) coupling. Note that the understanding about these two coupling mechanisms from different entropy contributions (the total entropy is simply written as a sum of magnetic, lattice, and electronic entropies $s_{tot} = s_{lat} + s_{mag} + s_{el}$) can be found elsewhere.[39,126] Compared with the MS coupled materials, for ME coupled materials the transition hysteresis can be more easily manipulated. In this section, recent advances related to typical ME coupled materials (including $(Mn,Fe)_2(P,Si)$-based and $La(Fe,Si)_{13}$-based compounds) and MS-coupled materials (including NiMn-based magnetic Heusler and magnetocaloric HEAs) are summarized.

3.1. ME Coupled $(Mn,Fe)_2(P,Si)$ Based Compounds

Although the first-row transition metal elements (Ti to Zn) in the periodic table of elements are chemically simple, the overlap of partially filled 3*d* and 4*s* bands provides uniqueness and complexity.[127] For example, for the transition-metal systems $(M_{1-x},M'_x)_2X$, where X = P, As or Sb and M, M' are first-row transition elements, some interesting physical properties have been discovered. Goodenough pointed out that the itinerant electron model of this system assumes that only the 3*d* bands have a finite density of states at the Fermi level, whereas the 4*s* band is empty.[127] On the other hand, the magnetic properties only reflect the number of 3*d* electrons per transition metal atom, and the existence of metalloids can sufficiently stabilize the material systems. The Fe_2P prototype material, a strongly anisotropic hexagonal ferromagnet (space group *P*-62*m*),[128] shows a first-order ferromagnetic transition with a T_C at around 216 K.[129–130] As one of the derivatives of Fe_2P the magnetic and structural properties of quaternary $(Mn,Fe)_2(P,As)$ compounds were studied by Fruchart and co-workers.[131–132] The MCE properties of the $(Mn,Fe)_2(P,As)$ compounds were originally studied by Brück and co-workers in 2000.[11] Within this work, the $(Mn,Fe)_2(P_{0.45}As_{0.55})$ compound was found to present a GMCE at the transition from the low-temperature FM state to the high-temperature PM state at about 300 K with a large $|\Delta s_m|$ of 14.5 J kg^{-1} K^{-1} and 18.0 J kg^{-1} K^{-1} for $\Delta\mu_0 H$ of 2 T and 5 T, respectively.[11] Subsequently, in response to the requirement of removing the toxic arsenic content, different $(Mn,Fe)_2(P,X)$ (X = Ge, Si) based intermetallic compounds have been developed. For instance, the so-called second-generation $(Mn,Fe)_2(P,Ge)$ and third-generation $(Mn,Fe)_2(P,Si)$ alloys were produced in 2007 and 2008, respectively.[133,134] Interestingly, the GMCE performance was almost kept stable after the metalloid's replacement of As by Ge/Si.[135,136] The differences of $(Mn,Fe)_2(P,X)$ (X = As, Ge, and Si) can be found in Ref. [137] Compared with other giant MCMs some advantages can be highlighted: an excellent GMCE performance, rare-earth free, relatively low economic costs, and the absence of toxic elements. More valuable characteristics of this series of compounds are the tunable T_C and the easily reduced hysteresis by compositional optimization. Simultaneously, an improved understanding of the physical mechanism associated with this strong magnetoelastic coupling in $(Mn,Fe)_2(P,Si)$ based materials has been achieved. On the one hand, from the fundamental crystal structure aspects, the site occupancy of different atoms has been distinguished unambiguously, as demonstrated in **Figure 6a**. Using neutron diffraction (ND), Miao et al. found that Mn atoms prefer the 3*g* site (in agreement with[138]) and that Fe atoms prefer the 3*f* site, while P/Si atoms randomly distribute on the 1*b*/2*c* sites (for the Si-rich case Si atoms show a preference for the 2*c* site).[139] On the other hand, from theoretical investigations the so-called "mixed magnetism" mechanism has been found to be responsible for the GMCE in the $(Mn,Fe)_2(P,Si)$ based MCMs. The crystallographic 3*g* and 3*f* sites of the hexagonal lattice, represent layers with relatively large stable magnetic moments (preferentially Mn) and relatively weak unstable magnetic moments (preferentially Fe), respectively. The latter shows an interesting quenching of the moment across the magnetic transition, as indicated by density functional theory (DFT),[140] ND,[139,141] and X-ray magnetic circular dichroism.[142] Combined DFT calculations and synchrotron high-resolution X-ray diffraction[143] experiments show a significant electronic charge redistribution around the Fe atoms across the ferromagnetic transition, which was attributed to the competition between magnetism and covalent bonding (electric entropy cannot be ignored). Moreover, it is found that the change in the *c*/*a* ratio of the hexagonal unit cell is closely related to ΔT_{hys}, which could be ascribed to a change in the transition-induced elastic strain energy.[144] Yibole et al. successfully grew $(Mn,Fe)_2(P,Si)$ single crystals by the tin flux method and the single crystal XRD data demonstrated the isostructural properties before and after transition. It is found that the preferred magnetization direction is along the *c* axis and the low temperature (5 K) magnetic anisotropy is determined with $K_1 = 0.28 \times 10^6$ J m^{-3} and $K_2 = 0.22 \times 10^6$ J m^{-3}.[145] Single crystals with different compositions were also obtained.[145–147] Miao et al. studied the development of magnetic moments from spatial and temporal aspects in the paramagnetic regime of $(Mn,Fe)_2(P,Si)$ by means of polarized neutron diffraction and muon-spin relaxation techniques, and investigated the dynamics between short-range magnetic correlations and long-range magnetic ordering.[148] They also observed a spin-density-wave (SDW) phase can co-exist with PM and FM phases in certain compositions of $(Mn,Fe)_2(P,Si)$ and the SDW-FM transition can be kinetically arrested at low temperature.[149] In addition, Dung and You et al.[140,150] established the complete phase diagram of magnetocaloric $Mn_xFe_{2-x}P_{1-y}Si_y$ quaternary compounds and reported the corresponding magnetic/structural properties.

Besides the above fundamentals associated with the $(Mn,Fe)_2(P,Si)$ based materials, different optimization strategies of GMCE performance have been proposed. On the one hand, chemical pressure engineering (substitutional/interstitial doping with external dopants) has been proven effective. Figure 6b, lists the reported dopants for $(Mn,Fe)_2(P,Si)$ based MCMs so far.[133,136,151–165] For example, Guillou et al.[136] pointed out that B substitution with limited concentration can efficiently decrease the ΔT_{hys} from 75 to only 1.6 K. Most importantly, the modified materials show good mechanical properties and excellent reversibility of GMCE after 10 000 cycles of magnetization/demagnetization ($\Delta T_{cyclic} \approx 2.8$ K with only $\Delta\mu_0 H$ of 1.1 T). It was found that V, Nb, and Mo substitution can also reduce the hysteresis of $(Mn,Fe)_2(P,Si)$ based MCMs, which is important as it is known that hysteresis will significantly degrade the energy efficiency of these materials in devices.[154,158–159,166] Additionally,

© 2024 Wiley-VCH GmbH

16146840, 0, Downloaded from https://onlinelibrary.wiley.com/doi/10.1002/aenm.202400369 by Tu Delft, Wiley Online Library on [08/04/2024]. See the Terms and Conditions (https://onlinelibrary.wiley.com/terms-and-conditions) on Wiley Online Library for rules of use; OA articles are governed by the applicable Creative Commons License

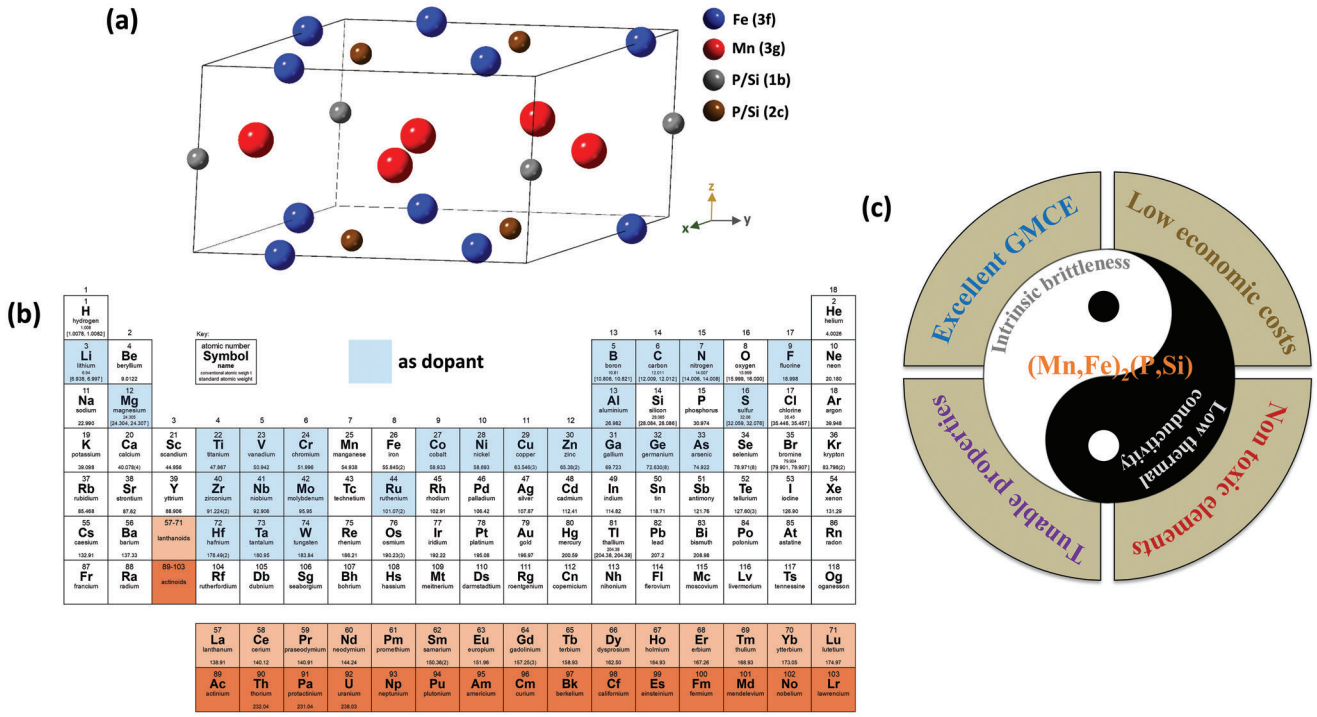

Figure 6. a) Schematic representation of the crystal structure for the $(Mn,Fe)_2(P,Si)$ based MCMs.[174] Copyright 2022, F. Zhang. b) Reported dopant for $(Mn,Fe)_2(P,Si)$ based MCMs so far. Copyright 2016, IUPAC (the International Union of Pure and Applied Chemistry). c) Schematic figure related to advantages and disadvantages about $(Mn,Fe)_2(P,Si)$ based MCMs.[174] Reproduced under the terms of the CC BY license. Copyright 2022, F. Zhang.

considering different application scenarios, tuning T_C towards a higher/lower temperature with negligible ΔT_{hys} is important for MCMs. However, alloying with doping elements does not necessarily only tune the T_C (toward a higher T_C by Li, B, C, Al, Ge, Zn, and Zr, and a lower T_C by N, F, S, V, Ni, Co, Cu, Ge, Nb, Mo, and Ru), but potentially also change the ΔT_{hys}. Typical doping elements like B, V, Nb, and Mo can even shift the strong FOMT toward the critical point between the FOMT and SOMT with a negligible ΔT_{hys}, while F doping can make the FOMT stronger with a larger ΔT_{hys}. Zhang et al. found that W and Ta substitution can act as a good strategy to solely regulate T_C and effectively maintain (or improve) the GMCE property without an increase in ΔT_{hys}.[164,165] As described earlier, interestingly, F, which possesses the highest electronegativity value among the elements, influences the metal–metalloid system differently (increased ΔT_{hys} and magnetic moments) compared with B (low electronegativity).[153] The results can further help us understand the role of the electrons for this itinerant-electron metamagnet.

On the other hand, advanced manufacturing techniques have been applied. For example, the 3D printed $(Mn,Fe)_2(P,Si)$ based MCMs using selective laser melting (SLM) have been fabricated by Miao et al.[167] The printed materials show a limited impurity phase (<2%) and a large $|\Delta s_m|$ (> 15.0 J kg^{-1} K^{-1} for $\Delta\mu_0 H = 2$ T), and the 3D printing will make these MCMs be easily shapable. However, they did not report the changes in the mechanical brittleness. Lai et al.[168] applied machine learning for composition optimization of $(Mn,Fe)_2(P,Si)$ and found a promising composition of $Mn_{1.70}Fe_{0.30}P_{0.63}Si_{0.37}$ with a transition temperature of 97 K at 1 T. The value T_C can be lowered to 73 K by substituting Fe with Co, and the corresponding large magnetocaloric performance further extends its application into the cryogenic region. Similar machine learning methods have also been applied to accelerate the design of $(Mn,Fe)_2(P,Si)$ based MCMs.[169] Moreover, except advantages, the typical obstacles for this material family are low thermal conductivity (λ) and intrinsic brittleness, as shown in Figure 6c. To solve the above issues, Miao et al.[170] proposed a promising Cu composite strategy. In brief, by continuous Cu networks within the main matrix, the formed unique microstructure is designed by hot pressing the $(Mn,Fe)_2(P,Si)$/Cu core/shell powders. The composite exhibited a high λ of 20.4 W m^{-1} K^{-1} and significantly enhanced the mechanical properties with a large maximum compressive strength of 570 MPa, which are the best comprehensive properties for room-temperature MCMs ever reported. Furthermore, utilizing high-energy ball milling Zhang et al.[112] synthesized $(Mn,Fe)_2(P,Si)$-based nanoparticles, and systematically investigated the influence of crystallite size and microstructure on the GMCE. This work may enrich the investigation of the functionality of nanoscale $(Mn,Fe)_2(P,Si)$ materials, similar as its parent compounds Fe_2P in, e.g., heterogeneous catalysis, energy storage batteries, etc.[171,172] Two reviews focused on $(Mn,Fe)_2(P,Si)$ based MCMs can be found in the literature.[37,173] With the development of advanced techniques, more new insights and optimization related to this family are expected in the following years.

3.2. ME Coupled $La(Fe,Si)_{13}$ Based Compounds

The $LaFe_{13-x}Si_x$ system has a cubic $NaZn_{13}$-type structure (space group *Fm*-3*c*), and a stable phase region for $1.4 < x < 2.6$. Note

© 2024 Wiley-VCH GmbH

16146840, 0, Downloaded from https://onlinelibrary.wiley.com/doi/10.1002/aenm.202400369 by Tu Delft, Wiley Online Library on [08/04/2024]. See the Terms and Conditions (https://onlinelibrary.wiley.com/terms-and-conditions) on Wiley Online Library for rules of use; OA articles are governed by the applicable Creative Commons License

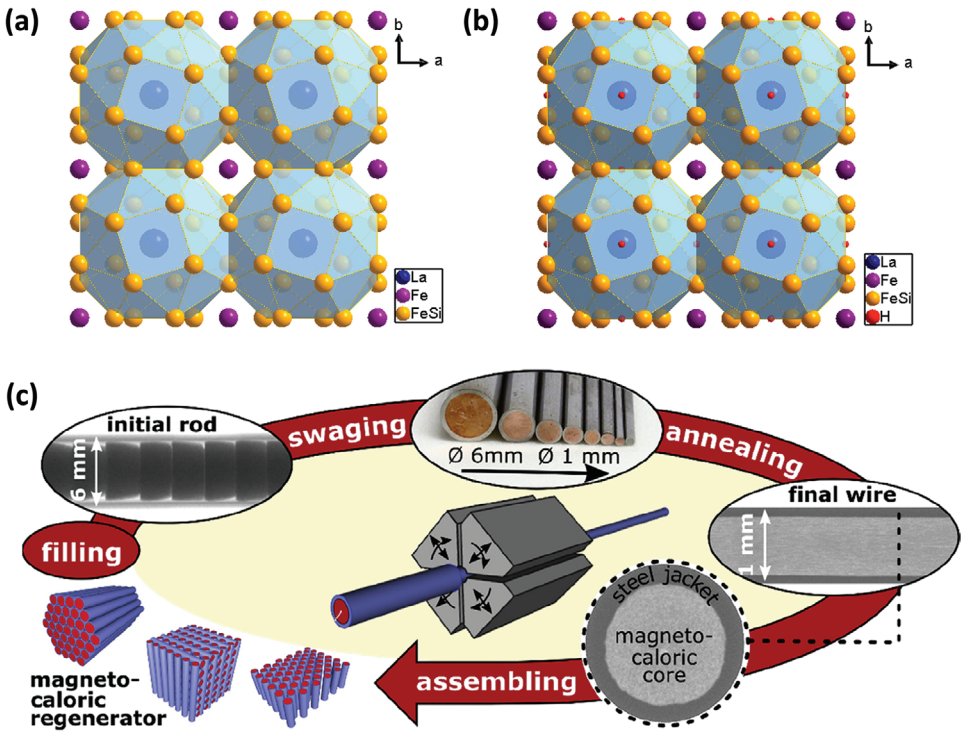

Figure 7. Schematic diagram of the crystal structure for a) $La(Fe,Si)_{13}$ and b) hydrogenated phase $La(Fe,Si)_{13}H_x$.[175] Copyright 2018, Elsevier. c) Shaping process of brittle MCMs for room-temperature application: A steel tube is filled with pre-alloyed compacted powder and swaged down to 1 mm composite wires ready to assemble in a magnetocaloric regenerator after heat treatment. Reproduced with permission.[190] Copyright 2018, Elsevier.

that the binary $LaFe_{13-x}$ cannot independently form, and Si will be helpful for stabilization, but higher Si contents ($x > 3.2$) will produce the tetragonal structure. The $LaFe_{13-x}Si_x$ compounds undergo a FOMT between the itinerant electron FM and PM state. During the transition, a large lattice volume change of about 1.5% occurs. The crystal structure and atom distribution for $La(Fe,Si)_{13}$ and the hydrogenated phase $La(Fe,Si)_{13}H_x$ are shown in **Figure** 7a,b, respectively.[175] Recent progress related to its MCE is summarized below:

Gruner et al.[176] found that for $LaFe_{13-x}Si_x$ there are significant changes in the element-resolved vibrational density of states (DOS) across the FOMT using nuclear resonant inelastic X-ray scattering and DFT calculations. They concluded that these changes originate from the itinerant electron metamagnetism of the Fe atoms and the lattice entropy cooperatively contributes to the total entropy with magnetic and electronic entropy. Shao et al.[175] applied X-ray absorption near-edge structure (XANES) spectra for the $La(Fe,Si)_{13}H_x$ materials and provided evidence of valence electron transfer from hydrogen to Fe, which indicated a close relation between different electronic surroundings. Fujita[177] investigated the hydrogen redistribution during the transition (known as the splitting phenomenon) and found that the splitting phenomenon can be influenced by the annealing conditions, e.g., it will be incompletely suppressed after a short duration of homogenization annealing, and it gradually disappeared with increasing annealing duration. Skokov et al.[178] studied a two-stage nature of the FOMT in the model $LaFe_{11.8}Si_{1.2}$ compound, which are ascribed to the properties of the itinerant electron meta-magnetic (IEM) transition. They explained the nature of the observed behavior from atomistic scale experiments (X-ray absorption spectroscopy (XAS), XMCD, and Mössbauer spectroscopy) together with first-principles calculations. Hardy et al.[179] proposed a simple thermodynamic model to describe the transition dynamics of this two-step process in the $LaFe_{13-x}Si_x$ system by considering a Gibbs free energy of the mixed state including three terms: chemical, elastic, and interfacial. In addition to these physical insights, various optimization methods toward performance improvement and microstructure modification have been implemented. It is found that magnetocaloric composites can efficiently improve their mechanical properties without sacrificing the MCE performance, by composite materials with ductile second phases like epoxy resin,[180] Al,[181] Fe,[182,183] Cu,[184,185] Sn-In-Bi Field's metal,[186] In,[187] Sn,[188] Nb/Ta,[189] etc. For example, using the hot rolling technique Miao et al. reported that the bending strength of the $LaFe_{11.6}Si_{1.4}$/Fe composite can reach up to 176 MPa (26% improvement).[183] They found that the refinement of the ductile α-Fe particles plays a key role in hindering crack propagation and enhancing the mechanical strength. Moreover, to solve the brittleness issue after long cycling, Krautz et al. applied a core-shell logic by introducing seamless austenitic steel wires with a magnetocaloric core,[190,191] as shown in Figure 7c. To this effect pre-alloyed $La(Fe,Co,Si)_{13}$ powder was filled into a AISI 316L austenitic steel tube, and then swaged to wires with an outer diameter of 1 mm. This was followed by a very short post-annealing (10 min at 1050 °C). Finally, these thin wires were assembled in different geometries. The processing is promising when combining different ductile jacket materials (such as Cu-based alloys or Nb) to improve the

© 2024 Wiley-VCH GmbH

16146840, 0, Downloaded from https://onlinelibrary.wiley.com/doi/10.1002/aenm.202400369 by Tu Delft, Wiley Online Library on [08/04/2024]. See the Terms and Conditions (https://onlinelibrary.wiley.com/terms-and-conditions) on Wiley Online Library for rules of use; OA articles are governed by the applicable Creative Commons License

thermal properties or corrosion protection. Furthermore, compared with $(Mn,Fe)_2(P,Si)$ based MCMs, it is worth mentioning that a smaller number of doping elements (light elements (H,[192] B,[193] C,[194] N[195]), Cr,[196] Mn,[197] Co,[198] Ni,[199] Ce,[200] Pr,[201] Nd,[201] Gd[202]) have been introduced and functioned in the $LaFe_{13-x}Si_x$ system, which could result from the high concentration of Fe atoms (>70 at.%). For instance, Ce substitution and hydrogenation can produce nanograins (5–50 nm) within the $LaFe_{13-x}Si_x$ matrix.[200] In these refined $(La_{1-x}Ce_x)_2Fe_{11}Si_2H_y$ alloys, the value of the hysteresis losses can be monotonously reduced from 48.3 to 0.6 J kg^{-1}. More importantly, because of the modified microstructure the excellent GMCE performance has been well maintained after 10000 magnetic cycles ($\Delta T_{ad=}$ 2.03 K for $\Delta\mu_0 H$ of 1.3 T). Interestingly, Lai et al.[197] reported that co-doping of Ce and Mn cannot only reduce the ΔT_{hys} (down to 1.5 K), but also move the T_C into the cryogenic region (30–100 K). Therefore, this material family can potentially be used for more low-temperature applications. Two reviews that focus on $LaFe_{13-x}Si_x$-based MCMs can be found in the literature.[203,204] It is worth mentioning that the volume changes due to the isostructural phase transition are around 0.01 and 0.3%, respectively, and Fe_2P type and $La(Fe,Si)_{13}$ type materials present excellent reversibility. For example, the stability of the measured ΔT_{ad} has been tested for 90 000 cycles on $La(Fe,Co,Si)_{13}$ and showed no significant changes.[205] Together with $(Mn,Fe)_2(P,Si)$ based MCMs, currently $La(Fe,Co,Si)_{13}$ type and their hydrides are the most promising alternatives without critical elements for near room-temperature application under practical magnetic fields (<2 T).[36]

3.3. MS Coupled Heusler Based Compounds

Heusler compounds were discovered and developed at the end of the 19th century,[206] and the well-known Cu_2MnAl compound found by Fritz Heusler[207,208] demonstrated fascinating ferromagnetism because all constituent elements are non-ferromagnetic. Although there is no clear definition of a Heusler compound, the nomenclature of Heusler compounds is popularly classified as Half Heusler, Full Heusler, and Inverse Heusler.[206] Nowadays, over 1500 Heusler compounds have been found, and the big family keeps expanding and remains a great scientific curiosity due to its versatile physical functionalities, which can be widely applied for various scenarios such as spintronics (or spin transport electronic) applications, thermoelectric devices, sensors and actuators, superconductors and semiconductors, topological insulator, and solid-state caloric effects.[206] As demonstrated in **Figure 8**a, the periodic table shows the potential X_2YZ type Heusler compounds with different combinations of elements. Herein, we focus on the specific Ni/Mn-based magnetic Heusler compounds, where the magnetic orderings (e.g., ferromagnetic ordering) strongly couples with the ferroelastic ordering arising from a structural phase transformation (e.g., martensitic transformation). It should be mentioned that most Heusler alloys do not exhibit martensitic transformations.[206] The so-called strong MS coupling gives rise to many novel magnetic functionalities like the giant magnetoresistance (GMR) effect, magnetostriction, magnetic shape memory effect, super-elasticity, and GMCE. Since the discovery of reversible diffusionless first-order phase transitions (by spontaneous symmetry-breaking strains) in the model Ni-Mn-Ga compounds,[209,210] more smart magnetic Heusler materials presenting GMCE have been discovered in Ni-Mn-Ga,[211,212] Ni-Mn-In/Sb,[213–215] and Ni-Mn-Sn based[216] Heusler compounds. Among these compounds, they always crystallize in the *fcc* cubic *Fm*-3*m* structure (space group 225) with the highly ordered $L2_1$ structure, like Ni_2MnGa in Figure 8b. For the fully stoichiometric Heusler compounds (X_2YZ), the *X* atoms occupy the 8*c* (1/4, 1/4, 1/4), while the *Y* and the *Z* atoms preferentially occupy the 4*a* (0, 0, 0) and 4*b* (1/2, 1/2, 1/2) sites, respectively. During the martensitic transformation the high-temperature $L2_1$ structure will transform to the low-temperature martensite with less symmetry like tetragonal, orthorhombic, or monoclinic ($L1_0$, 3(6)M, 5(10)M, and 7(14)M) types. These variants of martensite will be arranged spatially by twinning into ordered microstructures (so-called martensitic laminates).[217] In Figure 8b, the geometric relationship between the $L2_1$ austenite and the tetragonal martensite is exhibited for the case of Ni_2MnGa from different direction. In addition, when a magnetic field is applied or when the temperature is changed, the martensitic transformation can be triggered due to the magnetic difference between the weakly magnetic (paramagnetic (PM) or antiferromagnetic (AFM)) martensite and the strongly magnetic (ferrimagnetic (FIM) or ferromagnetic (FM)) austenite. The change in Zeeman energy ($E_{Zeeman} = -\mu_0 \int MHdV$, where *M* is the magnetization, *V* the unit-cell volume and *H* the external magnetic field) will destabilize the system and make the martensitic or inverse martensitic (diffusionless) phase transition happen, as illustrated in Figure 8c.[174] For magnetocaloric Heusler compounds, one always observes large thermal hysteresis of the phase-transition because of the strong magneto-structural coupling. To reduce the transformation hysteresis, one of most efficient ways is to achieve better geometric compatibility between martensite and austenite, which enables high phase reversibility.[218] Note that different chemical compositions could generate different low-temperature modulated and non-modulated (NM) martensite structures.[219] Details on the advances associated with traditional NiMn-based magnetic Heusler compounds can be found elsewhere.[30,206,220–222] In this sub-section, we mainly focus on another novel group of Heusler compounds coined as the all-*d*-metal Ni(Co)MnTi system, which was first found in 2015[122] and in recent years developed fast due to its advantages like a tunable T_C, rare-earth-free composition, non-toxicity, and excellent mechanical properties.[223,224] Interestingly, two early important works associated with Ti stabilization and decreasing the structural transition temperature towards the Ni–Mn binary system should be mentioned.[225,226] Contrary to the traditional Ni-Mn-Ga/In/Sb/Sn-based magnetic Heusler compounds, the all-*d*-metal Heusler materials contain no main group elements, and they are stabilized by covalent *d*-*d* hybridization, rather than *p*-*d* hybridization between transition elements and main-group elements,[122] which resulted in an obvious enhancement of the mechanical properties across the martensitic transition where the intrinsic brittleness of the traditional Heusler alloys could efficiently be prevented.[122,223] Therefore, the recent developments of the all-*d*-metal Ni(Co)MnTi based and some other emerging all-*d*-metal series magnetic Heusler compounds are reviewed below:

© 2024 Wiley-VCH GmbH

16146840, 0, Downloaded from https://onlinelibrary.wiley.com/doi/10.1002/aenm.202400369 by Tu Delft, Wiley Online Library on [08/04/2024]. See the Terms and Conditions (https://onlinelibrary.wiley.com/terms-and-conditions) on Wiley Online Library for rules of use; OA articles are governed by the applicable Creative Commons License

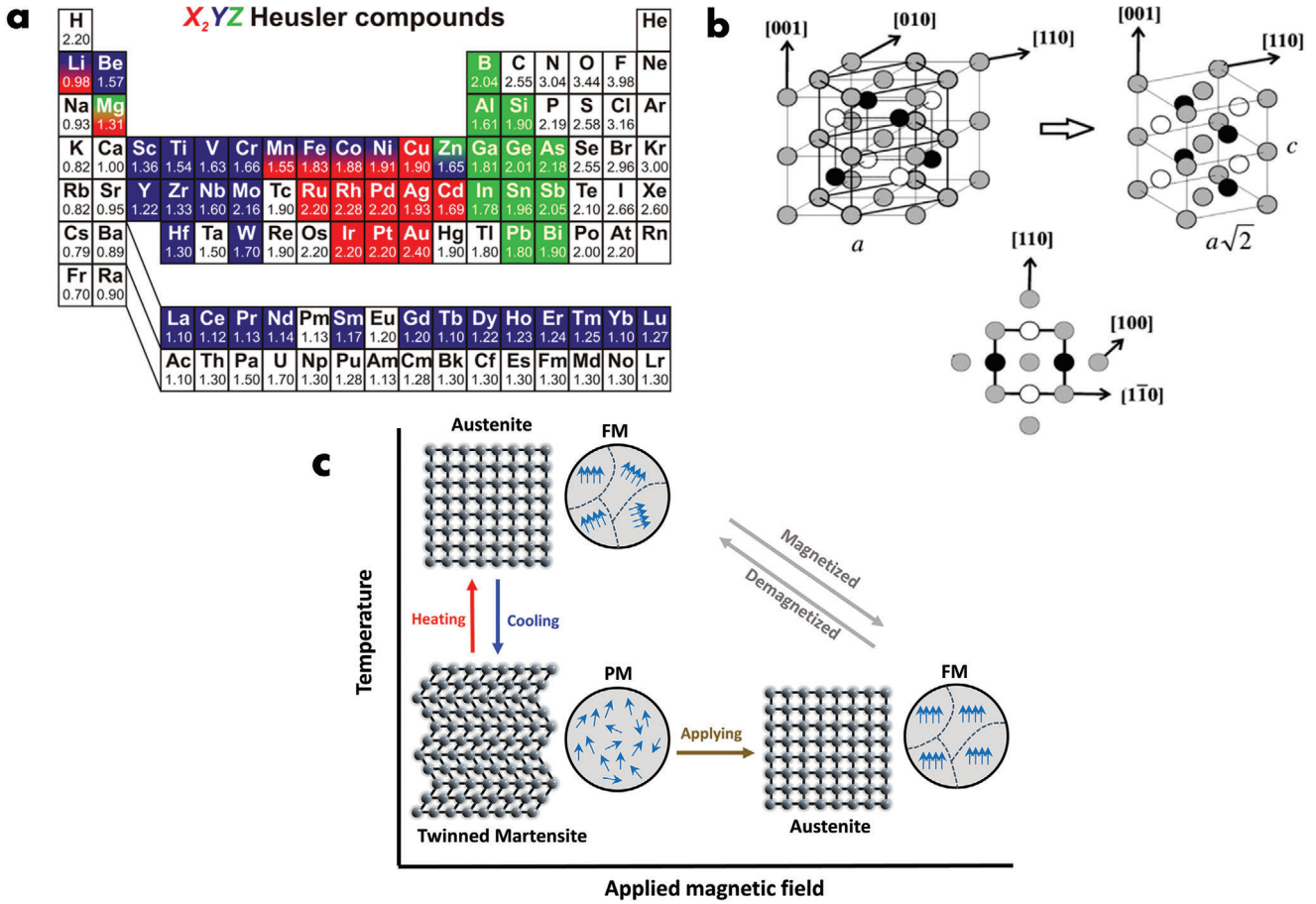

Figure 8. a) Periodic table of the elements showing different elements that can potentially form X_2YZ type Heusler compounds according to the color scheme. Reproduced with permission.[227] Copyright 2011, Elsevier. b) The $L2_1$ austenite showing the relationship with the tetragonal unit cell (martensite) for the case of Ni_2MnGa from different direction. Light grey: Ni, white: Mn, black: Ga. Reproduced with permission.[30] Copyright 2009, IOP Publishing. c) Schematic figures of the temperature- and magnetic field- induced martensitic transformation for NiMn-*X* based magnetic Heusler compounds (*X* = Ga, In, Sn, Sb).[174] Reproduced under the terms of the CC BY license. Copyright 2022, F. Zhang.

First, some studies have been reported to further optimize the experimental MCE performance of all-*d*-metal Ni(Co)MnTi based Heusler compounds, in combination with electronic structure calculations.[228,229] For example, targeting to tune the microstructure rapid-solidification techniques (e.g., melt-spinning, suction-casting, and directional solidification) are applied.[230–236] Bez and coworkers[231] demonstrated that $Ni_{37.5}Co_{12.5}Mn_{35}Ti_{15}$ ribbons show a $|\Delta s_m|$ as high as 27 J kg^{-1} K^{-1} for a moderate $\Delta\mu_0 H$ of 2 T. Guan et al.[234] manufactured the strong <001>$_A$ preferred orientation in a polycrystalline $Ni_{36.6}Co_{12.8}Mn_{34.7}Ti_{15.9}$ alloy by the directional solidification technique. The alloy shows an excellent mechanical performance at room temperature such as the maximum compressive strength of 2823 MPa and strain of 17.7%. Moreover, the good GMCE property is maintained as the maximum $|\Delta s_m|$ of 23.2 and 28.1 J kg^{-1} K^{-1} for $\Delta\mu_0 H$ of 5 and 7 T, respectively. Furthermore, Zhang et al.[236] demonstrated that suction casting can tailor the GMCE performance by modifying the microstructure. Compared with arc-melted samples, the $|\Delta s_m|$ value of the suction-casted sample shows a 67% improvement from 18.4 to 29.4 J kg^{-1} K^{-1} for a $\Delta\mu_0 H$ of 5 T. As the ΔT_{hys} has maintained a low value (5.5 K) for the enhanced first-order phase transition, a very competitive reversible $|\Delta s_m|$ of 21.8 J kg^{-1} K^{-1} is obtained for $\Delta\mu_0 H$ = 5 T. Combining high-resolution transmission electron microscopy (HRTEM) and positron annihilation spectroscopy (PAS) results, the difference in lattice defect concentration is found to be responsible for a significant improvement in GMCE for the suction-cast sample, which suggests that defect engineering can be applied to control the GMCE like in traditional magnetic Heusler compounds.[237,238] Additionally, different annealing strategies have been applied,[239,240] Taubel and co-workers[240] reported that an optimized heat treatment can significantly affect the magnetocaloric properties in $Ni_{35}Co_{15}Mn_{37}Ti_{13}$ with a $|\Delta s_m|$ of 20 J kg^{-1} K^{-1} and a maximum ΔT_{ad} of −4 K for $\Delta\mu_0 H$ = 1.93 T. In this work, specifically, the authors studied the evolution of T_C of austenite with respect to the valence electron concentration *e*/*a*. The linear relationship is much stronger compared to the flat behavior in the well-studied Ni(Co)Mn-*X* (*X* = Al, In, Sn, Sb) systems. The reason behind this is ascribed to the preferred *B*2 disordering of austenite, which results in an enhancement of the ferromagnetic exchange interactions J_{ij} between the Co and Mn atoms with an increasing amount of Mn on the Ti lattice site. The *B*2

© 2024 Wiley-VCH GmbH

16146840, 0, Downloaded from https://onlinelibrary.wiley.com/doi/10.1002/aenm.202400369 by Tu Delft, Wiley Online Library on [08/04/2024]. See the Terms and Conditions (https://onlinelibrary.wiley.com/terms-and-conditions) on Wiley Online Library for rules of use; OA articles are governed by the applicable Creative Commons License

disordering, without $L2_1$ ordering, has been observed in neutron diffraction experiments.[241] Simultaneously, the external dopant such as B,[242,243] V,[244] Cr,[245] Fe,[246–250] Cu,[251,252] Y,[253] and Gd[254] are also an efficient method to regulate the GMCE property of this all-*d*-metal NiCoMnTi family. For instance, Zhang et al.[242] found that introducing a limited amount of interstitial B atoms within the $Ni_{36.5}Co_{13.5}Mn_{35}Ti_{15}$ compound can effectively decrease the ΔT_{hys} (down to 4.4 K), and simultaneously improve the saturation magnetization (maximum 40% enhancement) for low concentrations of B doping (up to 0.4 at.%). Due to the obtained low ΔT_{hys}, the maximum reversible $|\Delta s_m|$ amounts to18.9 J kg^{-1} K^{-1} at 283 K for $\Delta\mu_0 H$ = 5 T (22.0 J kg^{-1} K^{-1} at 281 K for $\Delta\mu_0 H$ = 7 T), which is competitive to other traditional NiMn-based Heusler compounds. In DFT calculations, an enhancement of the magnetic moments is observed by B doping, and the B atoms are found to preferentially occupy the *O-I* octahedral interstitial site (24*d* site of the *Fm*-3*m* space group). Actually, the positive influence of B microalloying has also been noticed in the NiMnTi ternary system for baro/elastocaloric applications,[255–258] which possibly results from the changes in microstructure and electronic structure. For cryogenic caloric cooling, the potential of Ni(Co)MnTi based Heusler compounds has also been studied.[259,260] Beckmann et al.[260] pointed out that the dissipation losses closely related to the strong FOMT MCMs with hysteresis could significantly limit its utilization of applications at cryogenic temperature, considering the increased dissipation energy and decreased heat capacity with reducing the phase transition temperature. Furthermore, except the caloric effects, recently other fruitful physical functionalities for all-*d*-metal Heusler compounds (including Ni(Co)MnTi) have sprung up such as high-temperature shape memory effect,[261] heterogeneous catalysis,[262] giant exchange bias,[263] transverse thermoelectric application,[264] permanent magnets,[265] magnetoresistance,[252] and thermal energy storage applications.[99] Low-dimensional thin films of Ni(Co)MnTi materials have been produced.[266,267] Additionally, apart from the current experimental verification of all-*d*-metal Heusler compounds (with main attention on Ni-Mn binary system[244,268–272]), the screening strategy based on high-throughput first-principles calculations has been successfully applied to accelerate the discovery of new all-*d*-metal compounds in the Heusler family[264,265,273–276] and more interesting all-*d*-metal compounds are expected to be confirmed in the following years.

3.4. Magnetocaloric High-Entropy Alloys

The extension of the concept of high-entropy alloy (HEA) from structural materials to MCMs remarkably fosters the screening and design of novel MCMs. To define HEAs, the equation for $\Delta S_{mix} = R\sum x_i \ln x_i$ is used, where R is the gas constant and x_i is the mole fraction of the i_{th} element. It is currently accepted that $\Delta S_{mix} \geq 1.5R$ is the threshold for being considered a HEA.[125] For further details, the reader is referred to ref. [277] Compared with conventional MCMs with a limited compositional space for elemental substitution/doping, magnetocaloric HEAs offer a nearly infinite compositional space for property optimization. Besides, HEAs usually display distinct types of microstructures (e.g., solid-state solution, multi-phases, and intermetallics), which can be further tailored to optimize the magnetocaloric, thermal, and mechanical properties. Numerous magnetocaloric HEAs have been developed since 2013, which evolve from the originally equiatomic compositions (first generation) to non-equiatomic compositions (second generation) and the latest HEAs with a FOMT (third generation).[125,278]

Lucas et al.[279] reported the MCE in equiatomic FeCoNiCr HEAs in 2013. Although this new class of MCMs shows moderate magnetocaloric properties ($|\Delta s_m| < 0.4$ J kg^{-1} K^{-1} for $\Delta\mu_0 H$ of 2 T), the tunable T_C and remarkable ductility have attracted considerable attention from the magnetocaloric community. Perrin et al.[280,281] attributed the moderate MCE in FeCoNiCr HEAs to the distributed exchange interactions between magnetic atoms induced by compositional disorder, as suggested by Mössbauer spectroscopy results. The distribution of exchange interactions in FeCoNiCr HEAs can be reduced by Pd addition, resulting in an increase in T_C and an enhancement of the magnetocaloric performance.[282] Wu et al.[283] reported a pseudo-quaternary $Fe_{25}Co_{25}Ni_{25}(Mo_{0.2}P_{0.4}B_{0.4})_{25}$ high-entropy bulk metallic glass (HE-BMG), which shows a maximum $|\Delta s_m|$ of 0.98 J kg^{-1} K^{-1} for $\Delta\mu_0 H$ of 2 T around 560 K. Additionally, FeCoNiCuAlCr HEA thin films deposited by Vorobiov et al.[284] using magnetron sputtering exhibit a moderate MCE ($|\Delta s_m|$ of 0.53 J kg^{-1} K^{-1} for $\Delta\mu_0 H$ of 5 T) near room temperature. Apart from equiatomic transition-metal-based HEAs, equiatomic rare-earth-based HEAs constitute another important class of first-generation magnetocaloric HEAs. $Gd_{20}Tb_{20}Dy_{20}Al_{20}M_{20}$ HE-BMGs display a SOMT with a T_C between 45 and 112 K, which is accompanied by a maximum $|\Delta s_m|$ of 9.43, 7.25, and 5.96 J kg^{-1} K^{-1} in $\Delta\mu_0 H$ = 5 T for *M* = Co, Ni, and Fe, respectively.[285] $Tm_{20}Ho_{20}Er_{20}Al_{20}Co_{20}$ HE-BMGs show a stronger MCE than the $Gd_{20}Tb_{20}Dy_{20}Al_{20}M_{20}$.[286] The maximum $|\Delta s_m|$ reaches 15.0 J kg^{-1} K^{-1} for $\Delta\mu_0 H$ of 5 T in the former. Interestingly, rare-earth-based HEAs in the form of microwires[287,288] and ribbons[289–293] fabricated by melt-extraction techniques show a better magnetocaloric performance (larger Δs_m or wider temperature span) than their bulk counterparts. For instance, a large $|\Delta s_m|$ of 15.73 J kg^{-1} K^{-1} is obtained in $Er_{20}Tm_{20}Ho_{20}Cu_{20}Co_{20}$ amorphous ribbons for $\Delta\mu_0 H$ = 5 T, which is much larger than typical rare-earth-based BMGs.[292]

The second-generation magnetocaloric HEAs are characteristic of non-equiatomic compositions, which considerably extends the compositional space of HEAs. Sarlar et al.[294,295] reported the MCE in non-equiatomic $Fe_{26.7}Ni_{26.7}Ga_{15.6}Mn_{20}Si_{11}$ and $Mn_{27}Cr_7Ni_{33}Ge_{25}Si_8$ HEAs, which show a maximum $|\Delta s_m|$ of 1.59 and 2.49 J kg^{-1} K^{-1}, respectively, for $\Delta\mu_0 H$ of 2 T. The maximum $|\Delta s_m|$ of the $Mn_{27}Cr_7Ni_{33}Ge_{25}Si_8$ HEA is more than double that of the first-generation magnetocaloric HEAs. It should be noted that the $Mn_{27}Cr_7Ni_{33}Ge_{25}Si_8$ HEA crystallizes in an orthorhombic crystal structure (space group *Pnma*), in contrast to the first-generation transition-metal-based HEAs that commonly have face-centered-cubic (*fcc*) or body-centered-cubic (*bcc*) structures. Besides that, the $Mn_{27}Cr_7Ni_{33}Ge_{25}Si_8$ HEA contains non-metal elements (i.e., Ge and Si) that are usually absent in the first-generation magnetocaloric HEAs. Sarlar et al.[295] hypothesize that the superior magnetocaloric performance of the $Mn_{27}Cr_7Ni_{33}Ge_{25}Si_8$ HEA originated from a combination of the unconventional crystal structure and the constituent elements. Nevertheless, the T_C (412 K) of the $Mn_{27}Cr_7Ni_{33}Ge_{25}Si_8$ HEA is far above room temperature, which is unfavorable for

© 2024 Wiley-VCH GmbH

16146840, 0, Downloaded from https://onlinelibrary.wiley.com/doi/10.1002/aenm.202400369 by Tu Delft, Wiley Online Library on [08/04/2024]. See the Terms and Conditions (https://onlinelibrary.wiley.com/terms-and-conditions) on Wiley Online Library for rules of use; OA articles are governed by the applicable Creative Commons License

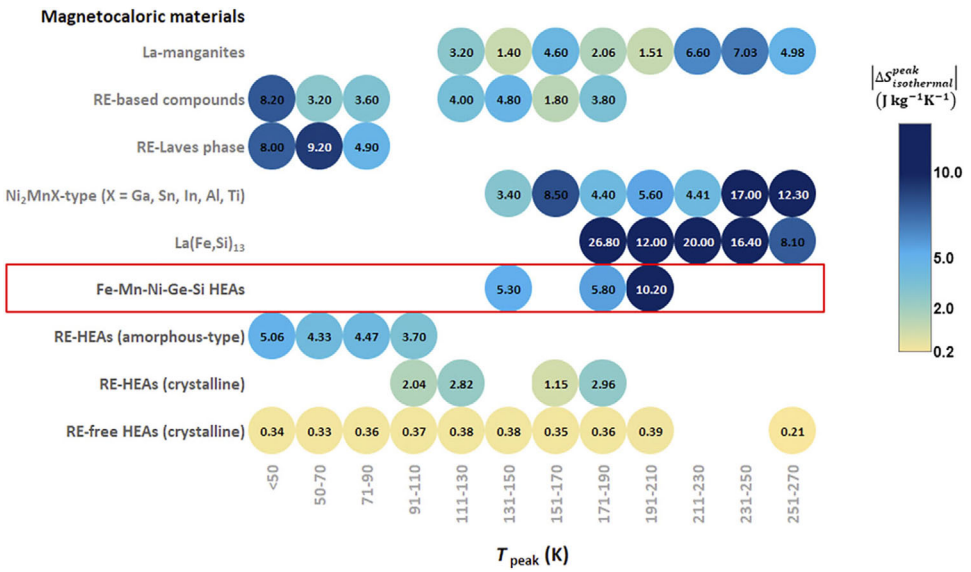

Figure 9. MCE comparison matrix for magnetocaloric HEAs *vs* high-performance conventional MCMs for 2 T.[278] Reproduced under the terms of the CC BY license. Copyright 2021, Author(s).

practical applications. A near room-temperature MCE is observed in $Al_{20}Mn_{20}Fe_{20}Co_{14.5+x}Cr_{25.5-x}$ HEAs by Zhang et al.[296,297] whereas the magnetocaloric performance is relatively moderate ($|\Delta s_m|$ of 0.6 J kg^{-1} K^{-1} in $\Delta\mu_0 H$ of 2 T). Recently, the conventional $LaFe_{11}Si_2$ MCM was turned into a magnetocaloric HEA by introducing multiple transition-metal elements (Co, Ni, Cr, and Mn) in the Fe sites.[298] The chemical disorder in the Fe sites causes local variations in bond length and magnetic exchange interaction, which broadens the SOMT and thus extends the working temperature span by 141.3%.

The evolution from equiatomic to non-equiatomic compositions also brings improved magnetocaloric performance for rare-earth-based HEAs. Yin et al.[299] reported an extended working temperature span (by 25%) in non-equiatomic $(Gd_{36}Tb_{20}Co_{20}Al_{20})_{100-x}Fe_x$ HEAs in comparison with the equiatomic counterparts, which is ascribed to the formation of an amorphous/nanocrystalline dual-phase structure. The working temperature span and $|\Delta s_m|$ of this non-equiatomic HEA can be further improved by DC current annealing,[300] compositional optimization,[301] and hydrogenation treatment.[302] Yin et al.[303] investigated the magnetic and magnetocaloric properties of two HE perovskites $(Dy_{0.25}Ho_{0.25}Er_{0.25}Tb_{0.25})FeO_3$ and $(Gd_{0.2}Dy_{0.2}Ho_{0.2}Er_{0.2}Tb_{0.2})FeO_3$ that were derived from the $GdFeO_3$ perovskite by introducing multiple rare earth elements in the Gd sublattice. The coexisting FM and AFM couplings between the disordered rare-earth and Fe sublattices induce a second-order spin-glass phase transition at low temperatures, which is accompanied by a considerable MCE over a wide working temperature range and promising for cryogenic refrigeration applications.[303]

A major challenge for magnetocaloric HEAs is the compositional disorder-induced distribution of exchange interaction between magnetic atoms, which broadens the SOMT and hence results in a moderate magnetocaloric performance. In order to offset the gap between magnetocaloric HEAs and high-performance conventional MCMs, Law et al.[125,278] proposed a property-directed strategy for the design of third-generation magnetocaloric HEAs. The key to this design scheme is to take advantage of the FOMT for magnetocaloric HEAs. In practice, this approach starts with the selection of a conventional MCM with a FOMT and subsequently turns it into the HEA category via compositional variations, while retaining the FOMT. Law et al.[304,305] successfully implemented this design strategy in *MM'X*-based magnetocaloric HEAs. A FOMT was realized in the $Fe_{22.2}Mn_{22.3}Ni_{22.2}(Ge_xSi_{1-x})_{33.3}$ HEAs, which is accompanied by a giant MCE ($|\Delta s_m|$ of 13 J kg^{-1} K^{-1} for $\Delta\mu_0 H$ = 2.5 T).[304,305] Such an outstanding magnetocaloric performance in the $Fe_{22.2}Mn_{22.3}Ni_{22.2}(Ge_xSi_{1-x})_{33.3}$ HEAs closes the long-standing gap between conventional high-performance MCMs and magnetocaloric HEAs (**Figure 9**). Zheng et al.[306] reported a GMCE ($|\Delta s_m|$ of 48.5 J kg^{-1} K^{-1} for $\Delta\mu_0 H$ = 5 T) in $(MnNiSi)_{1-x}(FeCoGe)_x$ HEAs that also belong to the *MM'X* material family. Additionally, Guo et al.[307] demonstrated that the large ΔT_{hys} in the *MM'X* material family can be significantly reduced via exploring the HEA composition space, where a ΔT_{hys} as low as 4.3 K is reached in the $Mn_{1.75}Fe_{0.25}CoNiGe_{1.6}Si_{0.4}$ HEA.

4. Multimodal Studies for the Development of MCMs

Understanding the complex functionality and intrinsic properties of MCMs, especially these coupled systems, necessitates multiple sources of information in spatial and time scales. By combining modalities that collect physical and chemical information, more detailed problems can be addressed. In recent years, advanced characterization techniques such as large-scale scientific facilities have undergone rapid development and the emergence of new experimental methods have greatly extended into the field of energy storage and conversion. In this section, we will present recent multimodal studies related to magnetic (including magnetocaloric) materials and some enlightening cases, and further highlight the importance of characteristic tools such as: i)

© 2024 Wiley-VCH GmbH

16146840, 0, Downloaded from https://onlinelibrary.wiley.com/doi/10.1002/aenm.202400369 by Tu Delft, Wiley Online Library on [08/04/2024]. See the Terms and Conditions (https://onlinelibrary.wiley.com/terms-and-conditions) on Wiley Online Library for rules of use; OA articles are governed by the applicable Creative Commons License

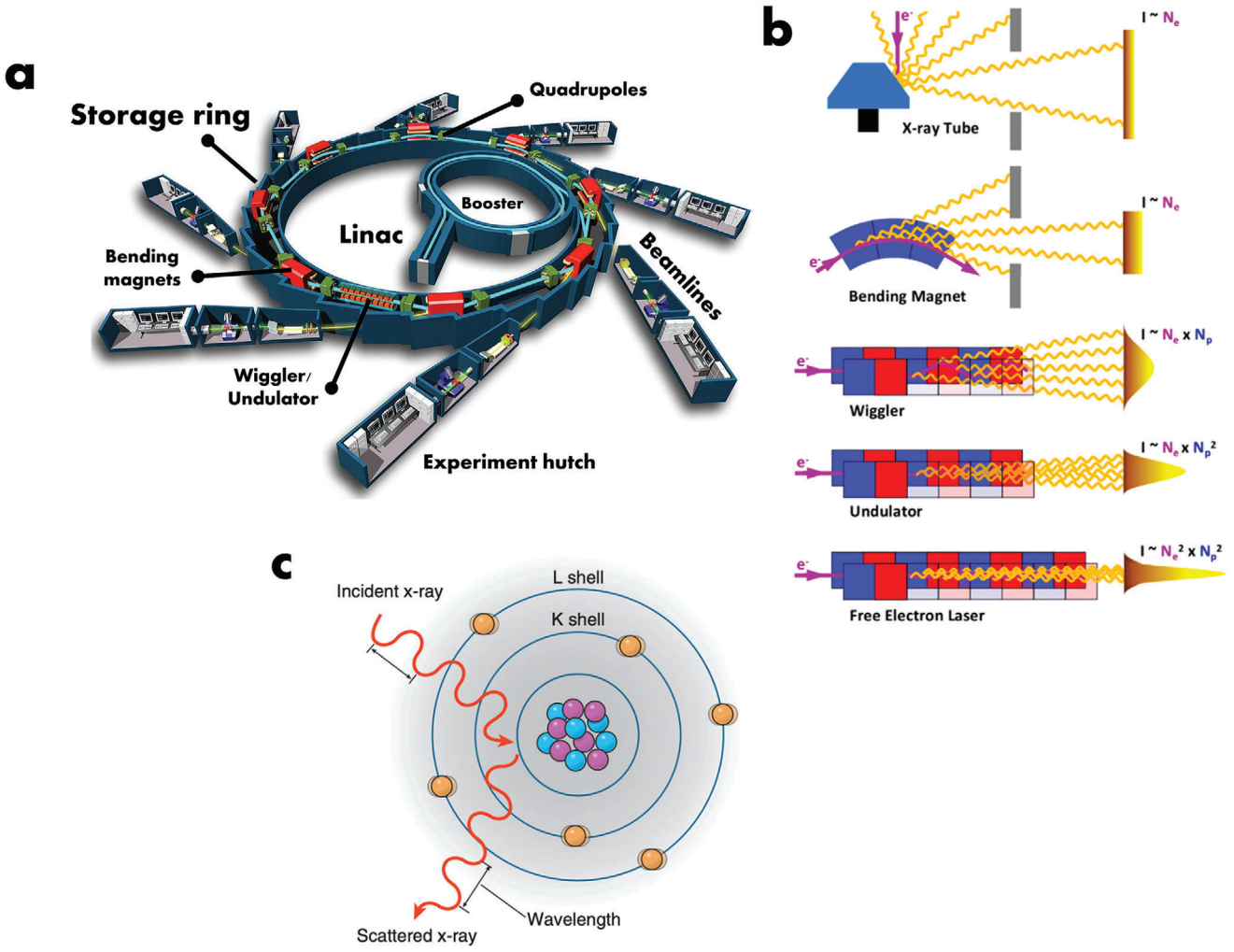

Figure 10. a) Schematic view of a synchrotron X-ray source, with main elements like linac, booster, storage ring, bending magnets, quadrupoles, insertion devices (undulator, wigglers), beamlines (tangent to the circumference) and experiment hutch. b) Principles of X-ray generation and enhanced X-ray flux in X-ray tube, bending magnet, wiggler, undulator and free electron laser. The electron beam is in purple, and the X-rays are in orange. The different colors in magnets indicate the two magnetic poles. Reproduced with permission.[312] Copyright 2015, Universität Hamburg. c) Illustration of the coherent elastic X-ray diffraction, where an incident X-ray interacts with orbital electrons rather than nucleus. For elastic diffraction there is no momentum loss, but direction changes.[313] Copyright 2012, Wolters Kluwer Health|Lippincott Williams & Wilkins.

synchrotron X-ray techniques; ii) neutron scattering; iii) muon spin spectroscopy; iv) positron annihilation spectroscopy; v) high magnetic fields for magnetocaloric research. We also briefly introduce the fundamental knowledge of different techniques and emphasize the corresponding advantages and disadvantages for the interpretation of multidimensional data acquired from multimodal studies. The combined platforms enable us to capture structural variations in unprecedented detail, underpin much more comprehensive information about materials, and help shed light on the link between structure and physical properties with the performance in advanced MCMs.

4.1. Synchrotron X-Ray Techniques

Synchrotron X-rays are produced when free electrons are traveling with relativistic velocities in an accelerator with magnetic fields.[308] The key characteristics of synchrotron radiation can be summarized as an energy/wavelength tunability, a high brightness (small cross section of the electron beam and high degree of collimation of the radiation), a natural narrow angular collimation, a high degree of polarization, a pulsed time structure, and a high beam stability.[309] According to the Planck–Einstein fundamental relation $E = \hbar\omega$, where E is the photon energy, $\hbar = h/2\pi$ the reduced Planck constant, and ω the angular frequency. for example, it indicates that photons with E from 0.01 to 10 keV will have wavelengths between 100 and 0.1 nm, respectively. Synchrotron X-rays interact with matter and can act as versatile probes (similar to neutrons, electrons, and positrons) to investigate physical/chemical properties (e.g., subtle microstructure changes, bonding, etc.). Nowadays, advanced synchrotron X-ray techniques have become ubiquitous in all the physical and natural sciences. As presented in **Figure 10**a, a typical synchrotron X-ray source includes the following main elements: linac, booster,

© 2024 Wiley-VCH GmbH

16146840, 0, Downloaded from https://onlinelibrary.wiley.com/doi/10.1002/aenm.202400369 by Tu Delft, Wiley Online Library on [08/04/2024]. See the Terms and Conditions (https://onlinelibrary.wiley.com/terms-and-conditions) on Wiley Online Library for rules of use; OA articles are governed by the applicable Creative Commons License

Table 2. Most prominent synchrotron facilities worldwide.[309,314] Copyright 2015, Springer-Verlag Berlin Heidelberg.

Light sources	Country/ area	Energy [GeV]	Current [mA]	Circumference [m]	Linear sections	Brilliance [ph/s/mrad^2/ mm^2/0.1%BW]	Website
ESRF	Europe	6.0	200	844.4	44	3.56×10^{21}	https://www.esrf.fr/
APS	USA	7.0	100	1104	40	8×10^{19}	https://www.aps.anl.gov/
Sping-8	Japan	8.0	100	1436	48	2×10^{21}	http://www.spring8.or.jp/en/
PETRA-III	Germany	6.0	100	2304	20	2×10^{21}	https://www.desy.de/
SSRF	China	3.5	300	432	27	$>10^{19}$	http://e-ssrf.sari.ac.cn/
ALBA	Spain	3.0	400	269	17	–	https://www.cells.es/en/
Diamond	UK	3.0	300	561.6	24	3×10^{20}	https://www.diamond.ac.uk/
Soleil	France	2.75	500	354	24	10^{20}	https://www.synchrotron-soleil.fr/en
Spear-3	USA	3.0	500	234	18	–	https://www-ssrl.slac.stanford.edu/
AS	Australia	3.0	200	216	19	–	https://www.ansto.gov.au/facilities/australian-synchrotron
PLS-II	South Korea	3.0	400	280	24	$\approx 10^{20}$	https://pal.postech.ac.kr/paleng/
TPS	Taiwan	3.0	400	518	24	$\approx 10^{21}$	https://www.nsrrc.org.tw/chinese/index.aspx
BESSY-II	Germany	1.7	200	240	16	5×10^{18}	https://www.helmholtz-berlin.de/
NSLS-II	USA	3.0	500	792	30	3×10^{21}	https://www.bnl.gov/nsls2/
Max-IV	Sweden	3.0	500	528	16	2.2×10^{21}	https://www.maxiv.lu.se/
SLS	Switzerland	2.4	400	288	12	4×10^{19}	https://www.psi.ch/en/sls

storage ring, bending magnets, quadrupoles, insertion devices (undulator, wigglers), beamlines (tangent to the circumference), and experiment hutch. The specific functions of these different components are introduced elsewhere.[310] Currently, the majority of third and fourth generation synchrotron sources operate in the medium-energy range (2-4 GeV) but several sources (ESRF, European Synchrotron Radiation Facility; APS, Advanced Photon Source; Spring 8, Super Photon ring-8 GeV; PETRA III, Positron-Electron Tandem Ring Accelerator III) are optimized in the high-energy range of the electron beams (6–8 GeV) to produce high-intensity X-rays. Most prominent synchrotron facilities worldwide and their corresponding characteristics are listed in **Table 2**. Benefiting by the continuous optimization and upgrading of bending magnet/wiggler/undulator components the synchrotron X-ray flux has continuously increased. Figure 10b shows the principles of X-ray generation and the enhancement of X-ray flux from a lab-based X-ray tube, a synchrotron light source to a free electron laser source. In addition, as shown in Figure 10c it is worth mentioning that X-rays interact with the electrons of atoms via the electro-magnetic interaction, which is the basic difference (the different elemental scattering cross section) in comparison to neutrons (that interact with atomic nuclei via very short-range strong nuclear forces).[311]

The synchrotron techniques can be roughly distinguished into hard X-ray (> 5 keV) and soft X-ray (<3 keV) categories based on their photon energy.[315] Herein the soft X-ray characterization techniques focused on surface science will not be introduced. Actually, the fundamental parameters that we use to perceive the physical world (such as energy, momentum, and position) can correspond to three broad categories of synchrotron experimental techniques (spectroscopy, scattering, and imaging). Moreover, each technique can further be coupled in a timing fashion by manipulating the short pulse lengths of synchrotron radiation. As shown below in **Figure 11**, we illustrate the categories of selected synchrotron techniques and their main applications for magnetic and caloric materials from different energy, momentum, and position domains.

4.1.1. Synchrotron Radiation X-Ray Diffraction (SR-XRD)

Due to the availability of monochromatic high flux and highly collimated beams at synchrotron sources, compared with lab-based XRD, the SR-XRD technique has the unique properties of a high signal/noise ratio, no $K_{\alpha 2}$ diffraction peaks, and a high angular resolution, which allow to capture complex microstructural details. The extremely high signal/noise ratio of the diffraction peaks is especially suitable for Rietveld refinement to resolve minor changes in the crystal structure. For powder-based SR-XRD experiments, the capillary geometry is most commonly applied because of its advantages: i) it is easily performed and aligned; ii) the resolution can be controlled by the capillary (normally smaller diameter means higher resolution and quartz capillaries are the best choice); iii) the sample environment can efficiently be conditioned based on different requirements; iv) the rotation speed of the capillary (samples) is tunable. Recently, some successful cases utilizing SR-XRD associated with magnetic and caloric materials have been obtained:

Yan et al.[316] implemented the SR-XRD experiments for the $Ni_2Mn_{1.44}In_{0.56}$ magnetic Heusler compound and determined the crystal structure of the modulated martensite. As shown in **Figure 12a**, the refinement indicated that the martensite had an incommensurate 6M modulated structure (super-space group $I2/m(\alpha 0\gamma)00$) with lattice parameters $a = 4.3919(4)$ Å, $b = 5.6202(1)$ Å, $c = 4.3315(7)$ Å, and $\beta = 93.044(1)°$. They further indicated that this 6M super-structure model could be representative for the off-stoichiometric Ni(Co)MnIn modulated martensite with a martensitic transition, even though the

© 2024 Wiley-VCH GmbH

16146840, 0, Downloaded from https://onlinelibrary.wiley.com/doi/10.1002/aenm.202400369 by Tu Delft, Wiley Online Library on [08/04/2024]. See the Terms and Conditions (https://onlinelibrary.wiley.com/terms-and-conditions) on Wiley Online Library for rules of use; OA articles are governed by the applicable Creative Commons License

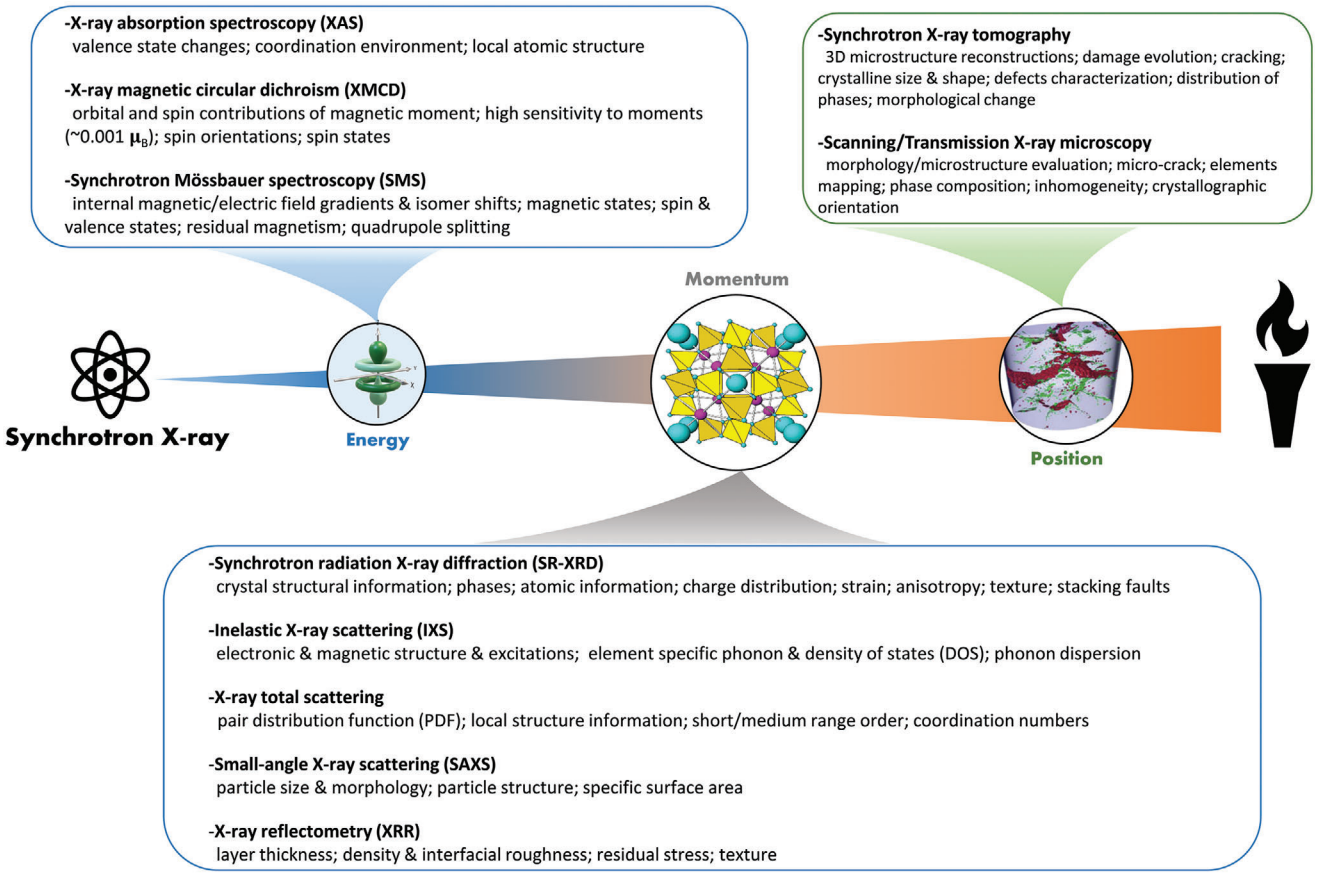

Figure 11. Schematic demonstration and categories of selected synchrotron techniques and their applications for magnetic and caloric materials from different energy, momentum, and position domains.

modulated structure highly depends on specific experimental conditions. The determination of the incommensurate modulated structure of low-temperature martensite by SR-XRD enables a more detailed understanding of the underlying mechanisms governing the MS coupling and other magneto-responsive properties in NiMn-based magnetic Heusler compounds. Interestingly, by analyzing the intensities and the full width at half maximum (FWHM) of the SR-XRD patterns, the studies by Singh et al.[317] demonstrate that NiMn-based magnetic Heusler compounds are highly sensitive to the residual stresses introduced during crushing of the ingot into powder over a wide temperature range. It was found that the martensite phase can be stabilized by the stresses. This finding highlights the sensitivity of the MS coupling in Heusler compounds for the internal stress state. Moreover, Huang et al.[318] found that the coexistence of two FM phases can occur in the arc-melted model $LaFe_{11.5}Si_{1.5}$ compound, which could be connected with different experimental conditions. The results obtained from SR-XRD, combined with magnetic measurements and Mössbauer spectroscopy provide experimental evidence that the two coexisted FM phases hold a different T_C, e.g., the phase with T_C = 216 K corresponds to a Si-rich phase with small lattice volume, and another one with T_C = 185 K is a Si-poor phase large lattice volume. Additionally, as mentioned before, the consideration of electron entropy change is always neglected during the entropy calculation. However, Boeije and co-workers[143] presented experimental evidence in $(Mn,Fe)_2(P,Si)$ based materials that the origin of the giant entropy change is also related to an electronic reconstruction caused by the competition between magnetism and bonding. The effect manifests itself as a redistribution of the electron density, which was measured by SR-XRD on $(Mn,Fe)_2(P,Si,B)$. For instance, the charge difference map (CDM) before and after the transition extracted from the SR-XRD experiments (Figure 12b) is in good agreement with the results from DFT calculations (Figure 12c). Similar studies have further confirmed this observation in this family.[319] The electronic redistribution is consistent with the formation of a covalent bond, resulting in a large drop in the Fe magnetic moments (so-called "Fe moment quenching"). The simultaneous change in bond length and strength, magnetism, and electron density contributes to the basis of the GMCE. The proposed new understanding of the mechanism of first-order magneto-elastic phase transitions provides an essential step for new and improved magnetic refrigerants, and it may also be suitable for other strong ME/MS coupling families. Furthermore, it is known that the hysteresis cannot easily be tamed for most first-order phase transformation structural materials. However, Chen and co-workers[320] reported that magnetic NiCoFeGa single crystals with a large superelasticity can exhibit a non-hysteretic mechanical response, a small temperature dependence, a high-energy-storage capability, and a cyclic stability over a wide temperature range (123–423 K), as presented in Figure 12d. From Figure 12e, the SR-XRD patterns under in

© 2024 Wiley-VCH GmbH

16146840, 0, Downloaded from https://onlinelibrary.wiley.com/doi/10.1002/aenm.202400369 by Tu Delft, Wiley Online Library on [08/04/2024]. See the Terms and Conditions (https://onlinelibrary.wiley.com/terms-and-conditions) on Wiley Online Library for rules of use; OA articles are governed by the applicable Creative Commons License

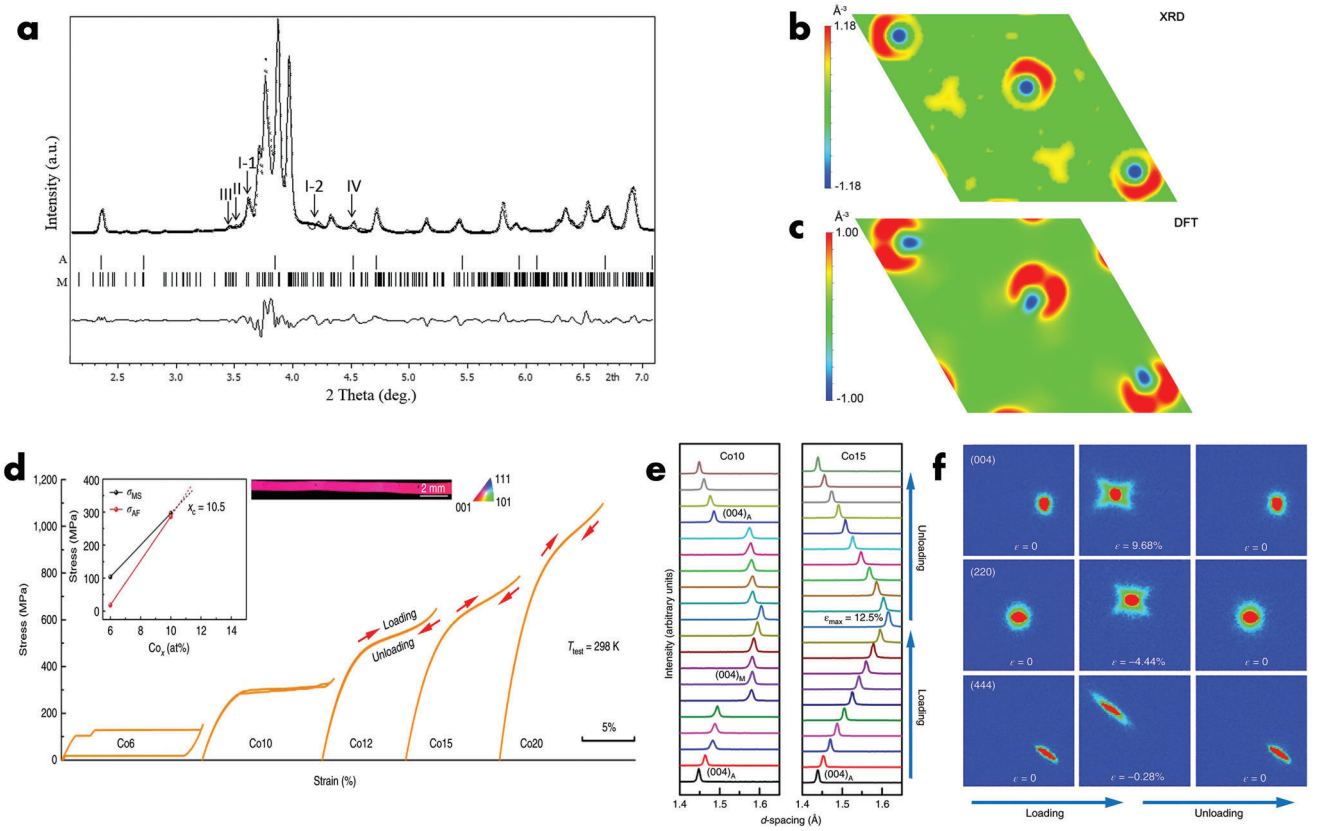

Figure 12. a) Refined SR-XRD patterns of $Ni_2Mn_{1.44}In_{0.56}$ alloy at room temperature. The vertical arrows I-1, I-2, II and III indicate $(\bar{1}21\bar{1})_M$, $(\bar{1}211)_M$ $(\bar{1}21\bar{2})_M$ and $(\bar{1}21\bar{3})_M$ satellite peaks of martensite, respectively, whereas the IV indicates the $(311)_A$ reflection of austenite. Reproduced with permission.[316] Copyright 2015, Elsevier. b) CDM across the FM transition from SR-XRD at 350 and 150 K. The unit cell is uniformly scaled when subtracting the FM and PM phases. Structure invariant indicates that the relative Fe coordinate is fixed. The difference between the FM state (blue) and the PM state (red) is clearly shown from scale bar. c) Corresponded CDM from the DFT calculations, which is in good agreement with the experimental one. b,c) Reproduced with permission[143] Copyright 2016, American Chemical Society. d) Room temperature stress-strain curves for different $Ni_{55-x}Co_xFe_{18}Ga_{27}$ alloys on loading and unloading. It is found that the superelasticity transforms from the typical martensitic transformation with a pronounced hysteresis to the trilinear response with non-hysteresis from low to high Co content. Left inset: the stress state for martensite (σ_{MS}) and austenite (σ_{AF}) as a function of Co concentration. Right inset: the orientation map of the Co20 fiber in the axial direction, indicating that the sample is a single crystal with the $[001]_{L21}$ orientation parallel to the fiber axis. e) Intensity changes of the $(004)_A$ crystal plane in the *d*-spacing during *in-situ* loading and unloading cycles for Co10 (left) and Co15 (right) fibers. It can be noticed the distinct discontinuous and continuous structural phase transformation characteristics. f) Two-dimensional XRD patterns of the (004), (220), and (444) reflections in three different states (before loading, under high strain, and after unloading) for Co20 fiber. d–f) Reproduced with permission[320] Copyright 2020, Springer Nature.

situ loading and unloading conditions clearly show the distinct discontinuous and continuous structural phase transformation characteristics for Co10 (left) and Co15 (right) fibers, respectively. In addition, the two-dimensional SR-XRD patterns of the characteristic (004), (220), and (444) reflections in three different states (before loading, under high strain, and after unloading) for the non-hysteretic Co20 sample are exhibited in Figure 12f. It is observed that the diffraction spots exhibit a significant diffuse scattering intensity as a result of strain, which indicates that stress-induced structural fluctuations could result in the discussed continuous phase transition.

4.1.2. Inelastic X-Ray Scattering (IXS)

To study the phonon excitations in condensed matter (meV region for the photon energy), it requires a high energy resolution of at least $\Delta E/E \approx 10^{-7}$.[321] Thanks to the especially high resolution and extremely small beam size (of the order of a few tens of a micrometer) in synchrotron sources, the IXS technique can be applied to study the electronic/magnetic structure/collective excitations, element-specific lattice vibrations, atomic dynamics/phonon dispersion, *etc.* For example, nuclear resonant inelastic X-ray scattering (NRIXS), which is intrinsically sensitive to lattice dynamics and provides the vibrational (phonon) density of states (VDOS)[322] is successfully applied to study different MCMs such as $La(Fe,Si)_{13}$ based,[176,322,323] $(Mn,Fe)_2(P,Si)$ based,[324] FeRh,[325] NiMn-based Heusler materials.[326] Gruner et al.[176] utilized NRIXS in the $LaFe_{13-x}Si_x$ system and unearthed that there are significant changes in the element-resolved VDOS across the FOMT, which originate from the itinerant electron metamagnetism related to Fe and lead to a pronounced magneto-elastic softening. Their experimental results indicate a strong interaction of all relevant degrees of freedom

© 2024 Wiley-VCH GmbH

16146840, 0, Downloaded from https://onlinelibrary.wiley.com/doi/10.1002/aenm.202400369 by Tu Delft, Wiley Online Library on [08/04/2024]. See the Terms and Conditions (https://onlinelibrary.wiley.com/terms-and-conditions) on Wiley Online Library for rules of use; OA articles are governed by the applicable Creative Commons License

(i.e., vibrational, magnetic, and electronic) in materials with a strong ME coupling and provide insightful understanding of the GMCE and into abnormal lattice thermal expansion phenomena. Moreover, the IXS data collected by Besssas et al.[324] indicated that in the $(Mn,Fe)_{1.95}(P,Si)$ compound the magnetic transition primarily affects the Fe vibrational modes, whereas the Mn vibrational modes are essentially not influenced. Nevertheless, Δs_m cannot completely compensate the Fe vibrational entropy change, indicating that the electronic entropy should be included. In combination with the ^{57}Fe nuclear inelastic scattering, it is proposed that an electronic topological transition may be concomitant to the magnetic transition and could contribute notably to the coupling between magnetic and elastic degrees of freedom. Furthermore, to better understand the entanglement of phonons and spins in the well-known Invar Fe-Ni alloys, Lohaus and coworkers[327] present experimental measurements of the phonon (NRIXS) and magnetic (synchrotron Mössbauer spectroscopy (SMS)) entropies under pressure. The phonon spectra were measured at pressures up to 21.3 GPa and the same conditions for the SMS. It is noticed that the Invar behavior derives from the competition between phonons and spins. For instance, the phonon contribution to thermal expansion compensates the magnetic contribution over the 0–3 GPa pressure range, while the compensation disappeared when pressures above 3 GPa. It is suggested that this kind of competition between phonon and spin interactions is responsible for the famous Invar effect.

4.1.3. X-Ray Total Scattering

The synchrotron total scattering contains both the Bragg scattering and the diffuse scattering of crystalline (or non-crystalline) materials. The crystal structural information of the atomic long-range order in well-crystallized materials can be deduced from the Bragg peaks. The short-range order information in disordered structures, can quantitatively be described by the atomic pair distribution function (PDF). Furthermore, for non-crystalline (glassy, liquid, and amorphous) and nanoscale materials, the PDF analysis has been widely used to determine their local structure. The analysis principles of the atomic PDF have been described in great detail in refs. [311,328]. For the PDF analysis, the importance of data corrections and qualities at higher Q values ($F(Q) = Q(S(Q)\text{-}1)$, where $F(Q)$ is the experimental reduced structure function and $S(Q)$ is the total scattering function) needs to be stressed. In total scattering experiments, normally the Q range should be as wide as possible, potentially $Q \geq 30$ Å^{-1},[328] which generally requires high-energy X-rays. Recently reported studies related to the X-ray total scattering coupled PDF analysis on MCMs are discussed below:

The MnSb compound with T_C = 577 K has been studied for waste-heat recovery MCE applications.[329] Kurzman et al.[330] utilized the PDF method combined with DFT calculations to study the structural relaxation around interstitial manganese (Mn_i) in ferromagnetic $Mn_{1+x}Sb$ ($0.03 < x < 0.23$) alloys. A significant positional disorder of Mn_i is found with the observation of a weak diffuse signal near the symmetry-forbidden (001) reflection that indicates a correlated disorder arising from Mn_i clustering. Subsequently, the structural relaxation (short-range structural distortions) significantly influences the Mn_i coordination environment and enhances the electronic localization. This study proves the importance of the degree of correlated local disorder structures in MnSb materials. Zhang et al.[331] applied X-ray total scattering in $Mn_3Ga_xN_x$ ($0.5 < x < 0.7$) to probe the local and intermediate structures and their influence on the phase transition. The PDF analysis excluded the formation of any metallic clusters or impurity phase of binary nitrides in the crystal structure besides MnO. Combining SR-XRD and neutron powder diffraction (NPD) data, it is concluded that the partial atomic arrangement at the lattice sites (partial occupancy of Mn at the 1*a* sites due to Ga deficiency) is responsible for the stabilization of FIM ordering in this family. Several experimental PDF studies have been reported for $La(Fe,Si)_{13}$[332] and $(Mn,Fe)_2(P,Si)$[333] compounds. Petkov et al.[334] introduced the in situ PDF analysis as a function of temperature and magnetic field for $Gd_5(Ge,Si)_4$ based compounds. The results indicate that nearby Gd atoms markedly rearrange during the FM-PM transition. Most importantly, it is noticed that even the local and average crystal structures for all $Gd_5Si_xGe_{4-x}$ alloys (x = 0.2, 0.7, 1.7) samples are the same in the PM state. However, in the low-temperature FM state, different structures are observed on the basis of different PDF fitting models (orthorhombic Gd_5Ge_4; orthorhombic Gd_5Si_4; monoclinic phase (space group $P112_1/a$)). For instance, contrary to the findings of Rietveld analysis (orthorhombic phase), the PDF analysis indicates that the local structure of the FM state for the x = 0.2 and 0.7 samples corresponds to a monoclinic structure. The authors further ascribe the local structural changes to the emergence of lattice distortions/strain during the transition, where Gd-*X* slabs slide with respect to one another, and distinct Si-Si and Ge-Ge dimers are formed.[334] Compared with the Ge-rich and Si-rich samples, it is believed that the subtle distortions may be larger in the intermediate x = 1.7 sample and can further serve as a bridge linking the monoclinic PM phase and nominally orthorhombic (but locally monoclinic) FM phase. This investigation highlights the importance of the X-ray total scattering coupled with atomic PDF analysis to capture the dynamic evolution processes of strongly coupled phase transitions.

4.1.4. X-Ray Absorption Spectroscopy (XAS) and X-Ray Magnetic Circular Dichroism (XMCD)

XAS is widely employed to probe the local atomic and electronic structure around the absorbing atoms. This method has the advantage that it is element-specific and non-destructive. Synchrotron radiation facilities can easily cover the energy range of 3–35 keV for the *K* and *L* absorption edges of elements with atomic number $Z > 18$ (Ar), whereas the elements with an absorption energy below 3 keV can be performed under ultra-high vacuum conditions to avoid attenuation and absorption by the air.[335] There are two main regions in the XAS: the X-ray absorption near edge structure (XANES) and the extended X-ray absorption fine structure (EXAFS). The XANES, spans from the absorption edge up to about 100 eV above, while the EXAFS is in the energy range above the XANES region; typically from 100 to 1000 eV above the absorption edge.[336] The analysis of XANES and the EXAFS provides information about the structural descriptors involving the bond distances/angles, interatomic distances, oxidation state, coordination numbers, and symmetry

© 2024 Wiley-VCH GmbH

16146840, 0, Downloaded from https://onlinelibrary.wiley.com/doi/10.1002/aenm.202400369 by Tu Delft, Wiley Online Library on [08/04/2024]. See the Terms and Conditions (https://onlinelibrary.wiley.com/terms-and-conditions) on Wiley Online Library for rules of use; OA articles are governed by the applicable Creative Commons License

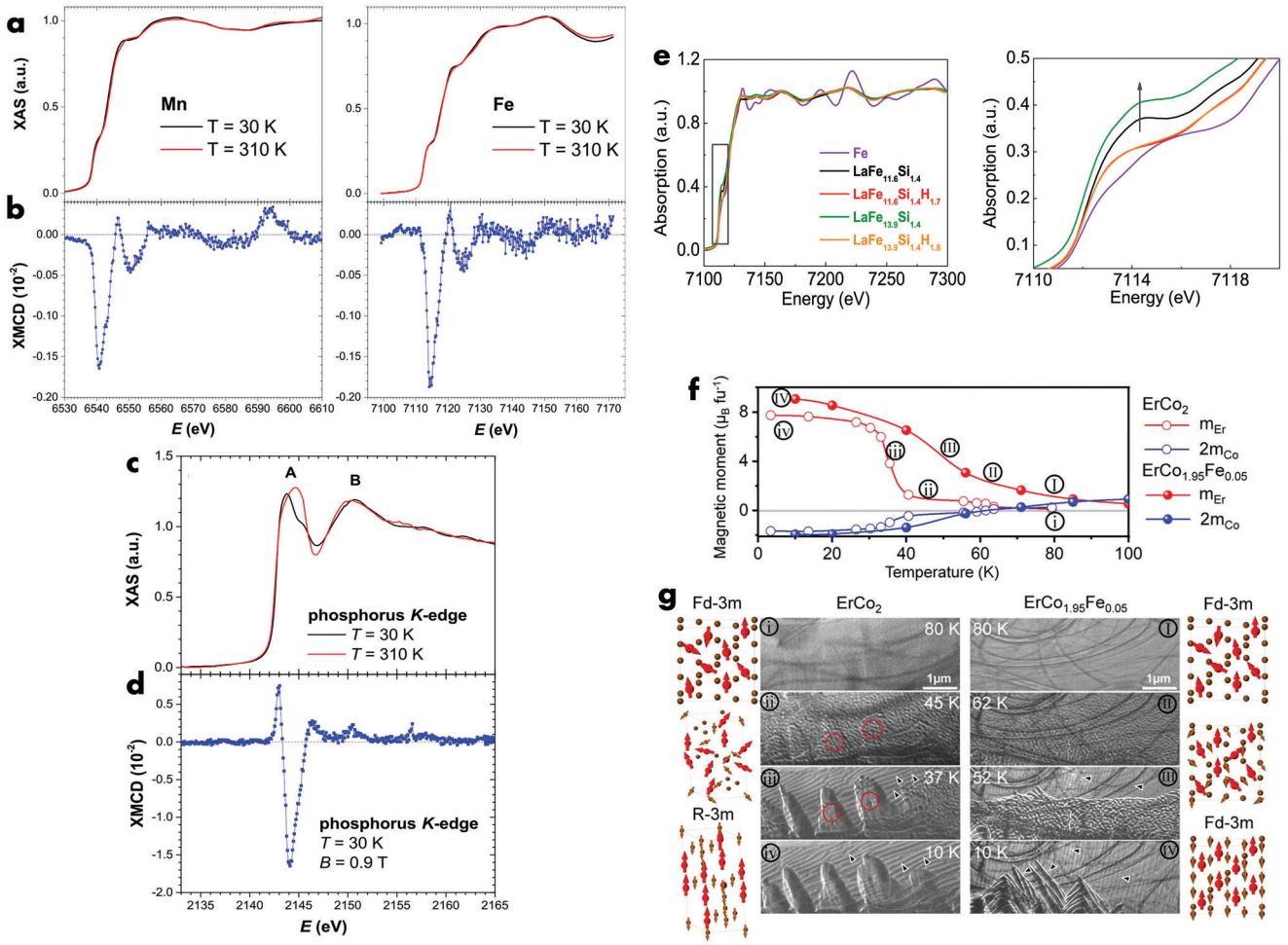

Figure 13. a) XAS spectra for $MnFe_{0.95}P_{0.66}Si_{0.34}$ at 30 and 310 K for the K-edge of Mn and Fe, respectively. b) Corresponded XMCD spectra at 30 K and applied field B = 0.9 T. c) XAS *K*-edge of P spectra at 30 and 310 K. d) Corresponded XMCD spectrum at 30 K and 0.9 T, normalized to the edge jump. a–d) Reproduced with permission[340] Copyright 2015, American Physical Society. e) (left) Fe *K*-edge XANES spectra of $La(Fe,Si)_{13}H_x$ based compounds. (right) Enlarged image of the rectangle area from (left) Reproduced with permission.[175] Copyright 2018, Elsevier. f) Temperature-dependent magnetic moments from XMCD for $ErCo_2$ and $ErCo_{1.95}Fe_{0.05}$ alloys. g) Magnetic domain evolution examined using cryogenic Lorentz microscopy in the Fresnel mode. The crystal structure changes for these two samples are also demonstrated in a unit cell. f,g)[355] Reproduced under the terms of the CC BY license. Copyright 2022, Author(s).

of the absorbing atom. Note that the requirements for good surface XANES and EXAFS spectra are different, which is especially important for bulk intermetallic samples with surface oxidation property. The principles of the XAS technique can be found in the literature.[337,338] Another important spectroscopic technique, XMCD, is a variant of XAS and can provide fingerprints about the magnetic properties of materials, such as the magnetic moment and magnetic anisotropy. XMCD involves measuring the difference in the absorption of left and right circularly polarized X-rays by a magnetically ordered material. Utilization of the XAS and XMCD techniques can reveal the evolution of the electronic structure and magnetic properties across the phase transition, and is thereby especially suitable for the phonon-electron-magnon coupled MCMs such as $Gd_5(Si_2Ge_2)$,[339] $(Mn,Fe)_2(P,X)$-based compounds (X = As, Ge, Si),[340–343] $La(Fe,Si)_{13}$-based materials,[175,344] NiMn-X based magnetic Heusler compounds (X = Ga, In, Sn, Sb),[345–348] FeRh,[349,350] Mn_3XC (X = Ga, Sn) based antiperovskites,[351] Mn-M-X (M = Co, Ni and X = Si, Ge),[352,353] Laves phase compounds,[354,355] GdNi alloys.[356] Recent advances in the application of synchrotron XAS and XMCD techniques on MCMs are summarized below:

Guillou et al.[340] utilized the XAS and XMCD spectra to study the changes near the *K*-edges of P, Mn, and Fe on the FOMT in $(Mn,Fe)_2(P,Si,B)$ compounds. As shown in **Figure 13a**, it is found that for Mn and Fe, the similarity of the *K*-edge XAS absorption spectra above and below the ferromagnetic transition suggests that the local electronic structure of Mn/Fe are barely affected (no changes in valence state or coordination numbers) by the FOMT. The similarity in integrated values of the XMCD spectra for Mn/Fe *K*-edges in Figure 13b suggests that the orbital moments are comparable for these atoms. However, as shown in Figure 13c, the *K*-edge XAS of P shows pronounced changes, which is a fingerprint for changes in the electronic structure

© 2024 Wiley-VCH GmbH

16146840, 0, Downloaded from https://onlinelibrary.wiley.com/doi/10.1002/aenm.202400369 by Tu Delft, Wiley Online Library on [08/04/2024]. See the Terms and Conditions (https://onlinelibrary.wiley.com/terms-and-conditions) on Wiley Online Library for rules of use; OA articles are governed by the applicable Creative Commons License

(possible changes in the electron redistribution/metal-metalloid bonding) during the transition. Interestingly, these XMCD results for the P edge in Figure 13d show an intense signal of 1.6% with respect to the edge jump. This indicates that nonmagnetic P can be magnetically polarized in the ferromagnetic state in this material family, which could result from the polarization of the metalloid *p* states due to the hybridization with the metal 3*d* states. Shao et al.[175] applied the XANES and EXAFS spectra to the $La(Fe,Si)_{13}H_x$ based materials with itinerant metamagnetism. The results of the EXAFS spectra at the La L_3-edge and the Fe *K*-edge prove that the interstitial H atoms preferentially occupy the 24*d* site. The XANES spectra of the La edge provide evidence of valence electron transfer from H to Fe, indicating a close relation between the electronic structure and H absorption. For instance, as present in Figure 13e, compared with the non-hydrogenated and hydrogenated samples, the white line (peak at around 5486 eV) of the La L_3 absorption edge decreased for the hydrogenated samples. Such a change is related to number of *d* symmetry empty states near the Fermi energy of La, which is ascribed to the localized La–H bond. This study emphasizes the importance of a dopant with a different electronegativity for the itinerant electron magnetism in MCMs. Moreover, Tang et al.[355] evaluated the phase transition processes in $Er(Ho)Co_2$-based Laves compounds by temperature-dependent XMCD measurements with *in-situ* Lorentz microscopy. As shown in Figure 13f, the magnetic moment of the Er and Co atoms for the $ErCo_2$ (FOMT) and $ErCo_{1.95}Fe_{0.05}$ (SOMT) alloys, extracted from XMCD (Er $M_{4,5}$ and Co $L_{2,3}$ absorption edges) show that the Co moments at low temperatures are opposite to the Er for both samples, while the Er moments are continuously enhanced upon cooling via the magnetic momentum alignment. To estimate the magnetic changes in real space, XMCD was combined with in situ Lorentz microscopy, which shows the formation of fine and maze-like magnetic domain structures for both samples. However, obvious an strain contrast has been noticed (red circles in Figure 13g) originating from the cubic/rhombohedral structural transformation in the FOMT $ErCo_2$ sample, whereas it is not found in the SOMT $ErCo_{1.95}Fe_{0.05}$ sample. Recently, new MCE-dedicated instrumentation associated with XAS and XMCD experiments has been developed at beamline ID12 of the ESRF.[357] The instrumentation can offer the possibility to measure XAS, XMCD, and XRD simultaneously with various macroscopic properties (magnetization, magnetostriction, magnetocaloric, magnetoresistance) under strictly the same experimental conditions, as a function of magnetic field (up to 17 T) and temperature (5- 325 K). It will be promising for the further mechanism understanding of MCMs.

4.1.5. Synchrotron X-Ray Tomography

The high-energy synchrotron radiation-based X-ray tomography techniques provide unique advantages such as i) non-destructive characterization; ii) multi-scale spatial resolution; iii) high temporal resolution to acquire detailed information on the microstructure evolutions, phase changes, interfacial interactions, 3D cracking and damaging, crystalline orientation, diffusion modes, and so on. The 3D tomography data are reconstructed from a series of high-spatial resolution two-dimensional (2D) digital radiographs (usually >1000) of the bulk samples, which need to be rotated successively by a small angle increment or continuous rotation for one radiograph.[358] In principle, there are two categories of reconstruction algorithms based on the transform processes (named analytic and iterative methods). Currently, depending on the configuration of setups, different modalities of techniques like parallel-beam synchrotron X-ray computed tomography, transmission X-ray tomography, scanning transmission X-ray tomography and micro-X-ray fluorescence are available from micrometer to nanometer scale.[359,360] For magnetocaloric research, the lab-based X-ray tomography techniques have been successfully applied for some cases, e.g., $(Mn,Fe)_2(P,Si)$-based compounds,[361] $La(Fe,Si)_{13}$-based compounds,[182,183,362–365] 3D printed $La_{0.6}Ca_{0.4}MnO_3$ and $La(Fe,Si)_{13}$ materials[366,367] to obtain the information like damage/porosity in compacted samples (i.e. bed structure)/composites, density, homogeneity, defects/cracks distribution and interfaces between the layers. But the relatively low spatial resolution of laboratory-based setups (the minimum voxel size is generally of εm size) prevents the acquisition of details with nanometer-size dimensions. Here we offer a few remarks by way of introduction of synchrotron-based X-ray tomography on other functional materials (e.g., self-healing metals[368,369]), so that others may be inspired for comparable experiments on MCMs. Using the synchrotron X-ray nano-tomography Fang et al. studied the self-healing behavior of creep damage by precipitation in binary Fe-Au,[370] Fe-W,[371] and ternary Fe-Au-W[372] alloys. The technique provides a unique combination of nanofocus (≈ 20 nm) and a very high photon flux (up to 10^{12} photons s^{-1} at $\Delta E/E \approx 1\%$). The 3D microstructure of unhealed and healed creep damage in an Fe–Au (1 at.% Au) alloy has been resolved. The creep cavities and the Au-rich precipitates formed within the creep cavities could be monitored inside the Fe-Au matrix with a nanoscale resolution (smallest voxel size of 25 nm). They further determined the size, shape (e.g., spherical, equiaxed, rod, sheet, and complex-shaped objects), and spatial distribution of the cavities and precipitates in creep-failed samples submitted to creep at various constant loads and a fixed temperature of 550 °C. By analyzing different stages of Au precipitation, the proposed self-healing mechanism was further identified.

At synchrotron X-ray sources there are continuous efforts to realize a combined increase in flux, increase in resolution, and decrease in effective beam size.[373] Furthermore, the availability of 2D single photon counting detectors strongly improves the signal-to-noise and the versatility also improves the modality of specific techniques, which continuously opens new windows for future advanced studies on MCMs.

4.2. Neutron Scattering

The unique properties of the neutron make it a power tool for fundamental research on condensed matter including MCMs. The thermal neutron has a de Broglie wavelength of about 1.8 Å, which is comparable to interatomic distances in condensed matter. As a result, the interference effect allows the neutron to resolve structure information for condensed matter. Secondly, the neutron is neutral without charge and can thus not only be directly scattered by the nuclei, but also penetrate deeply into bulk

© 2024 Wiley-VCH GmbH

16146840, 0, Downloaded from https://onlinelibrary.wiley.com/doi/10.1002/aenm.202400369 by Tu Delft, Wiley Online Library on [08/04/2024]. See the Terms and Conditions (https://onlinelibrary.wiley.com/terms-and-conditions) on Wiley Online Library for rules of use; OA articles are governed by the applicable Creative Commons License

samples. Neutron scattering is able to detect light elements (e.g., hydrogen, carbon, nitrogen), as well as distinguishing elements with similar atomic numbers Z (e.g., Mn and Fe), in strong contrast to X-ray diffraction. Besides, the large penetration length of the neutron makes a variety of sample environments (external pressure, magnetic field, stress, electric field, and etc.) available for in situ neutron experiments. Thirdly, the neutron carries a magnetic moment and therefore it can be scattered by magnetic moments of an unpaired electron in a magnetic material. This enables neutron scattering to determine the magnetic structure as well as spin dynamics for magnetic materials. Additionally, neutrons may transfer part of the kinetic energies to a sample through inelastic neutron scattering (INS), which offers unique insight into the diverse excitations and dynamics in condensed matter (e.g., lattice and magnetic excitations) due to the comparable energies between the neutron and the excitations. Currently, intense neutron beams for fundamental research are produced at two types of neutron sources, i.e., reactor sources and spallation sources. The fission of a radioactive nuclide (e.g., ^{235}U) yields an intense and continuous neutron beam in reactor-based neutron sources, including the High Flux Isotope Reactor (HFIR) at Oak Ridge National Laboratory (ORNL, US), National Institute of Standards and Technology (NIST, US), Institute Laue-Langevin (ILL, France), Heinz Maier-Leibnitz Center (FRM II, Germany) and the Australian Centre for Neutron Scattering (ANSTO, Australia). Spallation sources are based on accelerator technology, which have become more prevalent in recent decades due to the well-defined time structure of the neutron beam as well as the lower safety concerns compared to reactor sources. In general, spallation sources employ an accelerator to produce a pulsed, high-energy proton beam that strikes a neutron-rich target (e.g., tungsten, lead and mercury). The spallation process releases about 15–30 neutrons per proton and hence yields an intense neutron pulse. Spallation sources include the Spallation Neutron Source (SNS) at ORNL in the US, Neutron and Muon Source (ISIS) at Rutherford Appleton Laboratory in UK, the Japan Proton Accelerator Research Complex (J-PARC) in Japan, the China Spallation Neutron Source (CSNS) in China, the European Spallation Source (ESS) in Sweden, and the Spallation Neutron Source (SINQ) at Paul Scherrer Institute (PSI) in Switzerland. It should be noted that SINQ is an exception to the spallation sources, which produce a continuous neutron beam due to its unique design. Fundamental physics and typical applications of neutron techniques have been well documented in previous reviews[222,374–377] and books.[378–380] Below are some examples of the typical applications of different neutron techniques in MCMs.

4.2.1. Neutron Diffraction (ND)

High-performance MCMs are usually characterized by a strong coupling between spin, lattice, and electron degrees of freedom, which manifests itself by a first-order MS/ME transition accompanied by a GMCE. ND is able to simultaneously detect the magnetic and structural transitions and is thereby thus well suited for the fundamental research on MCMs. The following selected examples demonstrate the vital role that the ND plays in exploring the MS/ME coupling and tailoring the magnetocaloric performance of MCMs. Dung et al.[141] performed temperature-dependent ND on the $(Mn,Fe)_2(P,Si)$ MCMs. The large difference in the coherent neutron scattering length (b_c) between Mn (−3.75 fm) and Fe (9.45 fm) allows the unambiguous determination of the 3*f* and 3*g* site occupations in the hexagonal structure.[381] They found that the Mn prefers to sit on the 3*g* Wyckoff site surrounded by five P/Si atoms forming a square pyramid, while the Fe occupies the 3*f* site surrounded by four P/Si atoms forming a tetrahedron.[141] The different coordination environments between the Mn and Fe atoms lead to the so-called "mixed magnetism",[139–141,143] which is manifested by the contrasting temperature dependence of the Mn and Fe magnetic moments. The mixed magnetism uncovered by the ND experiments provides essential insight into the origin of GMCE in $(Mn,Fe)_2(P,Si)$ MCMs (described more in detail in Section 3.1). Similarly, ND experiments on the $LaFe_{11.6-x}Co_xSi_{1.4}$ alloys successfully clarified the Co site occupancies on the two Fe sublattices (i.e., 8*b* and 96*i*) in the $NaZn_{13}$-type cubic structure due to the considerable difference in the b_c between Co (2.49 fm) and Fe (9.45 fm),[381] which lays the foundation for the in-depth understanding of the physical property evolution by Co substitution.[382] The ability to detect light atoms makes ND a unique technique to resolve the site occupation of light doping atoms (e.g., nitrogen, carbon, and boron) in MCMs. Miao et al.[152] reported different doping effects between the B and C atoms on the T_C of the $(Mn,Fe)_2(P,Si)$ MCMs. ND studies on the B- and N-doped $(Mn,Fe)_2(P,Si)$ alloys reveal that B substitutes the Si on the 1*b* site, while N sits on both the 1*b* and interstitial 6*j*/6*k* sites. The replacement of Si by the B shortens the Fe-Mn interatomic distance, enhancing the magnetic coupling between the Fe and Mn moments and thus raising the T_C. In contrast, the occupation of N on the interstitial 6*j*/6*k* site brings a relatively small interatomic distance (of ≈1.5 Å) between the Fe and the nearest N neighbors. This induces a strong *p*-*d* hybridization between the Fe and N atoms, causing a reduction in the splitting of the Fe *d* band and hence a decrease in T_C. As a result, ND has greatly contributed to the understanding of the tuning mechanism with light atoms on the ME transition in $(Mn,Fe)_2(P,Si)$ MCMs. Similar ND studies have also been performed to explore the effect of hydrogen absorption on the ME transition in $La(Fe,Si)_{13}$ MCMs.[383] Hao et al.[198] performed hydrostatic pressure-dependent ND measurements on $La(Fe,Co,Si)_{13}$ alloys. They found that hydrostatic pressure enlarges the unit-cell volume and sharpens the first-order ME transition via shortening the intra-icosahedral Fe-Fe bonds in the $NaZn_{13}$-type cubic structure, which unveils the microscopic origin of the observed enhancement of MCE by hydrostatic pressure in $La(Fe,Co,Si)_{13}$ MCMs.[198] Miao et al.[159] reported magnetic field-dependent ND studies on $(Mn,Fe)_2(P,Si)$ alloys. The field-induced first-order PM-FM transition is well captured by the ND measurements, which allows a quantitative description of the reversibility of the ME transition and the MCE in a cyclic magnetic field.[159] Besides, ND has successfully been applied to determine a variety of magnetic structures (e.g., collinear AFM, spiral AFM and incommensurate SDW), as well as their thermal evolution, in $GdPO_4$,[384] $MnFe_4Si_3$,[385] NdCuSi,[386] $NdMnO_3$,[387] $Ln_3CrGa_4O_{12}$ (Ln = Tb, Dy, Ho),[388] *MM'X*,[389–391] MnPtGa,[392] HoB_2,[393] $HoAl_2Ge_2$,[394] $(Sc,Ti)Fe_2$[395] MCMs. Additionally, the magnetic, nuclear, and spin-incoherent scattering cross sections can unambiguously be

© 2024 Wiley-VCH GmbH

16146840, 0, Downloaded from https://onlinelibrary.wiley.com/doi/10.1002/aenm.202400369 by Tu Delft, Wiley Online Library on [08/04/2024]. See the Terms and Conditions (https://onlinelibrary.wiley.com/terms-and-conditions) on Wiley Online Library for rules of use; OA articles are governed by the applicable Creative Commons License

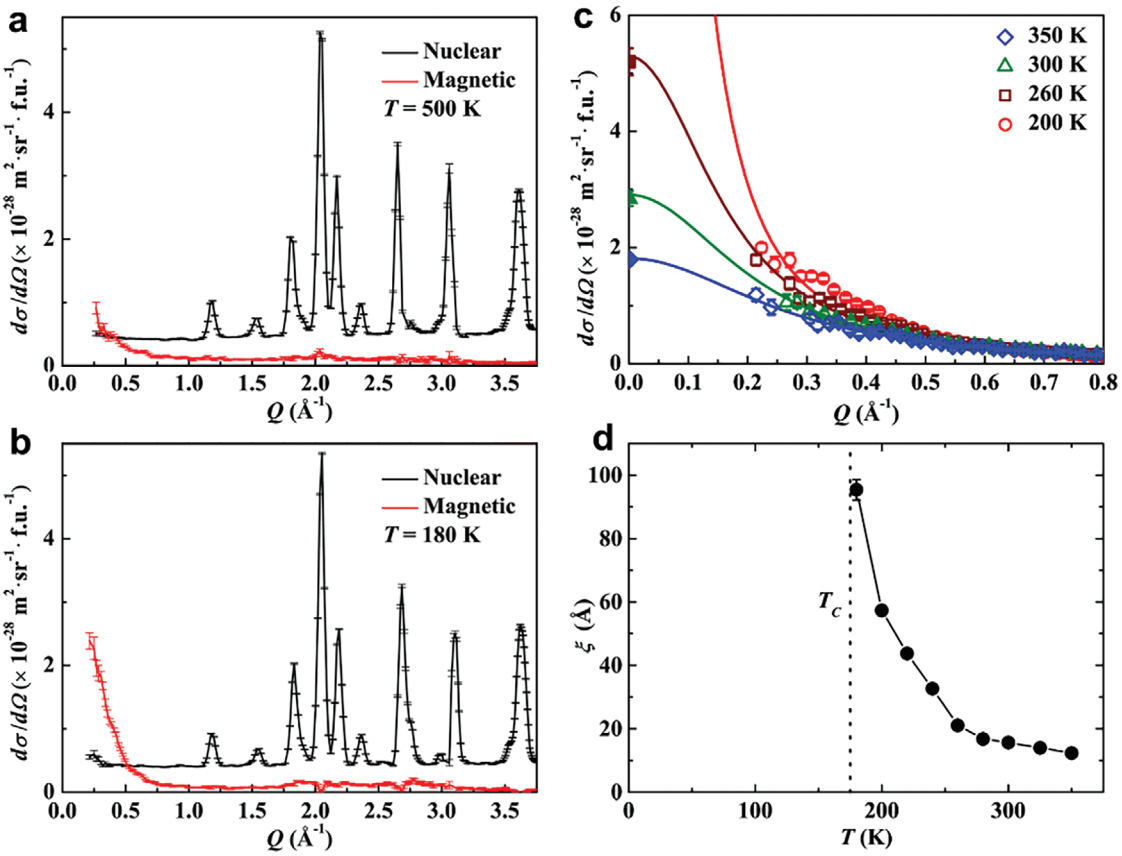

Figure 14. Polarized ND results on the $Mn_{1.70}Fe_{0.25}P_{0.50}Si_{0.50}$ alloy.[148] Separated magnetic and nuclear scattering cross section measured at a) 500 K and b) 180 K. c) Fit to the magnetic scattering cross section and d) the derived magnetic correlation length as a function of temperature. Reproduced with permission. Copyright 2016, American Physical Society.

separated by polarized ND measurements,[396] which enables the characterization of spatial correlations of magnetic spins (i.e., magnetic short-range order) in the PM state. Miao et al.[148] performed polarized ND experiments in the PM regime of $(Mn,Fe)_2(P,Si)$ MCMs. Noticeable magnetic scattering was observed close to $Q = 0$ at $T = 2.85T_C$ and the scattered intensity increases as the sample was cooled approaching T_C, indicating the enhancement of the magnetic short-range order by FM correlations (**Figure** 14a–c). The FM correlation length (ξ) is calculated to be 12.4 Å at $T = 2T_C$, which increases to 95.8 Å at $T = 1.03T_C$ and tends to diverge at T_C (Figure 14d). The thermal evolution of the correlation length provides a clear physical picture for the nucleation and growth of the magnetic correlations across the ME transition in $(Mn,Fe)_2(P,Si)$ MCMs.

4.2.2. Inelastic Neutron Scattering (INS)

Binisko et al. performed INS measurements on single crystals of Mn_5Si_3[397] and $MnFe_4Si_3$[398] that show an inverse and direct MCE, respectively.[399] INS results reveal that the field-induced noncollinear AFM to collinear AFM transition in Mn_5Si_3 is accompanied by the appearance of significant spin fluctuations, leading to an increase in the magnetic entropy and the observed inverse MCE.[397] In contrast, the field-induced PM to FM transition in $MnFe_4Si_3$ is associated with the suppression of the spin fluctuations, which causes a decrease in the magnetic entropy and is responsible for the direct MCE.[398] The crucial role of spin fluctuation in the FOMT and the GMCE has also been highlighted by INS studies in $La(Fe,Si)_{13}$[400] and HoF_3[401] MCMs. Additionally, INS measurements on the Fe_2P MCM show the presence of unusual acoustic-phonon modes with nonzero energy gaps in the FM phase.[402] The energy gap disappears at the first-order FM-PM transition, indicating a strong magnon-phonon coupling in Fe_2P, which is responsible for the strong ME transition and the resultant GMCE in Fe_2P.[402] Stonaha et al.[403] measured vibrational density of states (DOS) and phonon dispersion in the $Ni_{45}Mn_{36.6}In_{13.4}Co_5$ Heusler alloy using INS. The phonon dispersion measurements reveal that the low-energy transverse optic phonon is strongly coupled to the magnetic structure.[403] An abrupt increase in the vibrational entropy (of $\approx 0.22\ k_B$ per atom) was observed at the FM-PM transition of the austenite phase due to the strong ME coupling, which can contribute to the total entropy change together with the increased magnetic entropy.[403] Note that even the coupling of lattice, magnetic, and electronic degrees of freedom cannot be separated precisely, the INS technique can consider the lattice and magnetic degrees of freedom simultaneously, with respect to both static and dynamic effects for the magneto-structural or magneto-elastic coupled materials.[397,400,404]

© 2024 Wiley-VCH GmbH

16146840, 0, Downloaded from https://onlinelibrary.wiley.com/doi/10.1002/aenm.202400369 by Tu Delft, Wiley Online Library on [08/04/2024]. See the Terms and Conditions (https://onlinelibrary.wiley.com/terms-and-conditions) on Wiley Online Library for rules of use; OA articles are governed by the applicable Creative Commons License

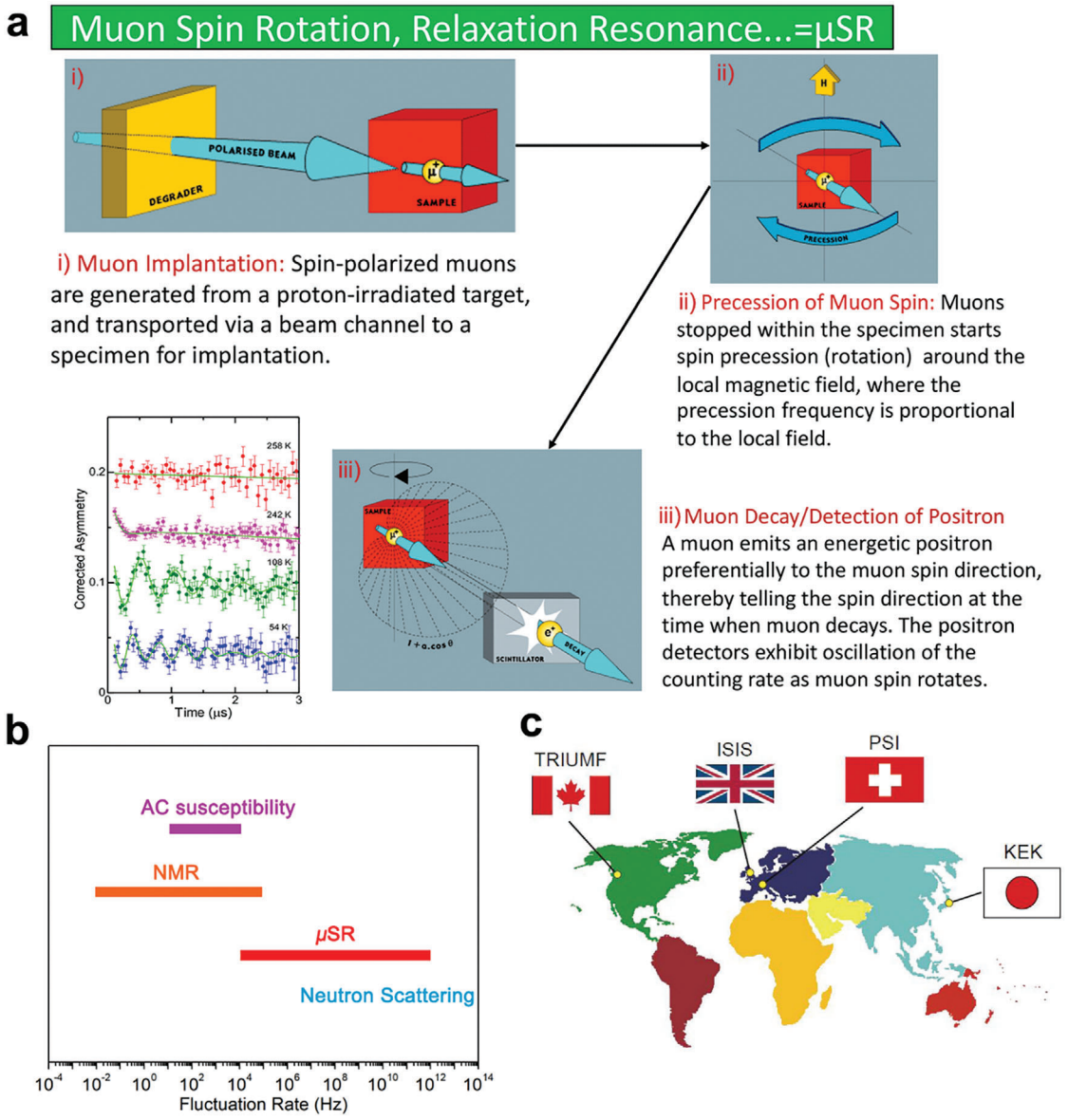

Figure 15. a) Schematic illustration of the working principle of εSR.[410] b) Time windows for different experimental probes on magnetism. c) Large-scale εSR facilities in the world.

4.3. Muon Spin Spectroscopy

Muons are elementary spin-½ particles belonging to the same family (i.e., lepton) as electrons. They are formed by a two-body decay of pions that are produced by collisions between high-energy proton beams and carbon nuclei in a graphite target. One interesting feature of muons is that they are almost completely spin-polarized opposite to their momenta due to the violation of parity involved in the production process.[405] Associated with the spin-½ character of the muon its magnetic moment experiences Larmor precession in a local magnetic field. A collection of muon techniques termed εSR (i.e., muon spin rotation, relaxation, and resonance) allows one to directly follow the evolution of the muon-spin direction (**Figure 15a**). A major difference between the μSR technique and those involving neutrons and X-rays (see Sections 4.1 and 4.2) is that scattering is not involved in the former. Neutron/X-ray scattering techniques take advantage of the change in energy and/or momentum of a scattered neutron/photon to extract structural and/or magnetic information. In contrast, muons are implanted into a sample and reside there with a lifetime τ_ε of 2.2 εs before a spontaneous decay into a positron (for positively charged muons, ε^+) or an electron (for negatively charged muons, ε^-) and a neutrino-antineutrino pair. Usually, positive muons are used in μSR experiments since they can be implanted into the region with a large electron density, where physicists working on magnetism, superconductivity, etc. are mostly interested in. The decay process of muons also involves a weak interaction and thus shows parity violation,[405] leading to a propensity for the emitted positron to emerge predominantly along the muon-spin direction.

© 2024 Wiley-VCH GmbH

16146840, 0, Downloaded from https://onlinelibrary.wiley.com/doi/10.1002/aenm.202400369 by Tu Delft, Wiley Online Library on [08/04/2024]. See the Terms and Conditions (https://onlinelibrary.wiley.com/terms-and-conditions) on Wiley Online Library for rules of use; OA articles are governed by the applicable Creative Commons License

Therefore, the analysis of the angular distribution of an ensemble of emitted positrons with respect to the initial muon-spin direction provides key information on the local magnetic field distributions and their fluctuations at the implanted site with high sensitivity (down to 10^{-5} T) on a time scale that complements the time scales probed by nuclear magnetic resonance (NMR) and neutron scattering (Figure 15b). μSR spectrometers are available at four main muon facilities in the world (Figure 15c), i.e., the PSI located in Switzerland, the Tri-University Meson Facility (TRIUMF) in Canada, the high energy accelerator research organization (KEK) Meson Science Laboratory in Japan and the ISIS Rutherford Appleton Laboratory (RAL) in the UK. Additionally, a new muon source is currently under construction at the China Spallation Neutron Source (CSNS). The fundamentals and application of the μSR techniques have been described extensively in a couple of review papers.[406–409]

The local probe nature of the μSR makes it extremely sensitive to spatially and/or temporally inhomogeneous magnetism, so it is an ideal probe of short-range order of disordered magnetic moments as well as their dynamics in magnetic (including magnetocaloric) materials. Miao et al.[148] performed zero-field μSR measurements at different temperatures for the $(Mn,Fe)_2(P,Si)$ MCMs. They observed a fast damping behavior in the μSR spectra above T_C, indicating a dynamic internal magnetic field at the muon's interstitial site. The muon-spin relaxation rate increases upon cooling and diverges in the vicinity of T_C, which can be ascribed to the slowing down of the magnetic fluctuations. The combined polarized neutron scattering and μSR results enable the extraction of the magnetic correlation time in the PM regime of the $(Mn,Fe)_2(P,Si)$ materials. They found that the magnetic correlation time is in the microsecond time scale at temperatures between $1.03T_C$ and $1.86T_C$ for the $(Mn,Fe)_2(P,Si)$ materials. The authors proposed that the strong short-range magnetic correlations in the PM state are crucial for the metamagnetic transition and unique mixed magnetism that are at the origin of GMCE in $(Mn,Fe)_2(P,Si)$ materials. Consequently, μSR offers a unique and effective tool to explore the temporal correlation of magnetic moments in MCMs, which can provide essential insight into the magnetic phase transition and MCE. Besides that, μSR is also a useful tool to detect coexisting and competing magnetic ground states at the microscopic level, which has been well demonstrated in frustrated systems.[411–415] Combining multiple techniques (X-ray, neutron, and muon), it was found that the competition between embedded ferromagnetic (FM) clusters and the antiferromagnetic (AFM) matrix contributed to the magneto-elastic (magneto-volume) effect in layered perovskite $PrBaCo_2O_{5.5+x}$ ($0 \leq x \leq 0.41$) materials, which points to a new and universal underlying mechanism for the magneto-elastic effect.[416] For instance, the results of muon spin polarization under zero field and under various magnetic fields indicate the fluctuation rates of FM-clusters, and the strength of frustrated FM-AFM interaction varies spatially, due to the inhomogeneous distribution of FM-cluster size and its hole density. Ofer et al.[411] reported an extensive μSR study on the EuL_2O_4 polycrystalline compounds (L = lanthanides Lu, Eu, Yb, and Gd) with quasi-1D "zigzag" chains of the L atoms. The high neutron absorption cross section of Eu makes it challenging to perform neutron scattering experiments on such compounds. Therefore, μSR has a competitive advantage in distinguishing magnetic interactions for materials containing elements that strongly adsorb neutrons. For the $EuLu_2O_4$ compound, where the lanthanide Lu has zero magnetic moment, an oscillating signal was observed in the zero-field μSR spectrum, indicating the presence of a static AFM order between Eu^{2+} ions. With an increase in the lanthanide moment (e.g., L = Yb), the zero-field μSR spectrum is characteristic of an incommensurate spin-density-wave order. Contrastingly, a slow relaxation instead of an oscillation is observed in the zero-field μSR spectrum for the $EuGd_2O_4$ compound that possesses a large lanthanide magnetic moment. This reveals that the static AFM order is perturbed with an increase in the magnetic moment along the quasi-1D zigzag chains and eventually becomes a dynamic AFM order. Owing to the complicated low-dimensional magnetic structure as well as the strong magnetic frustration, the EuL_2O_4 compounds do not show an abrupt decrease in the Δs_m and ΔT_{ad} at temperatures well below T_C, making them competitive candidates for active magnetic refrigeration down to very low temperatures.[417] It should be noted that the interpretation of μSR data is sometimes challenging because of the lack of precise information on the interstitial site that is occupied by the implanted muons, which may be unveiled by complementary first-principles simulations and nuclear magnetic resonance experiments.[418]

4.4. Positron Annihilation Spectroscopy (PAS)

As demonstrated in **Figure 16**a, different types of lattice defects are widely present in ordered crystals. These defects can strongly affect the functionality of the material. PAS is a non-destructive testing method that can obtain detailed information (type, size, structure, and concentration) of open-volume defects in solids, such as vacancies, cavities, dislocations, and grain boundaries with a remarkable sensitivity of 10^{-7}, which stems from its long diffusion length (>100 nm in most materials). This allows a positron to probe about 10^7 atoms before annihilation.[419] If the grain size is less than 100 nm, the positrons will most likely diffuse out to the grain boundaries before annihilation. In nanocrystalline materials, therefore, the annihilation gamma rays will mainly carry information about the structure of the intercrystalline regions and the grain boundaries.[420] It should be careful to analysis the PAS results related to intercrystalline information when the grain size is in the true nanometric regime, because it is possible all positrons are annihilated at the grain boundaries.[420,421] The unique capabilities of PAS result from the positron-electron pair annihilation process, which is accompanied by the emission of two γ rays. It can yield detailed information on both the electron density and the electron momentum in the region near the positron annihilation site,[422] as shown in Figure 16b. The fundamental physical properties of positron annihilation in condensed matter have been reported elsewhere.[422–426] As shown in Figure 16c, the three most important PAS techniques are angular correlation (AC), Doppler broadening (DB), and positron annihilation lifetime spectroscopy (PALS).[423] For example, the positron lifetime spectroscopy enables us to identify the type of defects in solids and determine their corresponded concentrations, while the coincidence measurement of the Doppler broadening identifies the local chemical environment of the defects.[427] The PAS techniques have been

© 2024 Wiley-VCH GmbH

16146840, 0, Downloaded from https://onlinelibrary.wiley.com/doi/10.1002/aenm.202400369 by Tu Delft, Wiley Online Library on [08/04/2024]. See the Terms and Conditions (https://onlinelibrary.wiley.com/terms-and-conditions) on Wiley Online Library for rules of use; OA articles are governed by the applicable Creative Commons License

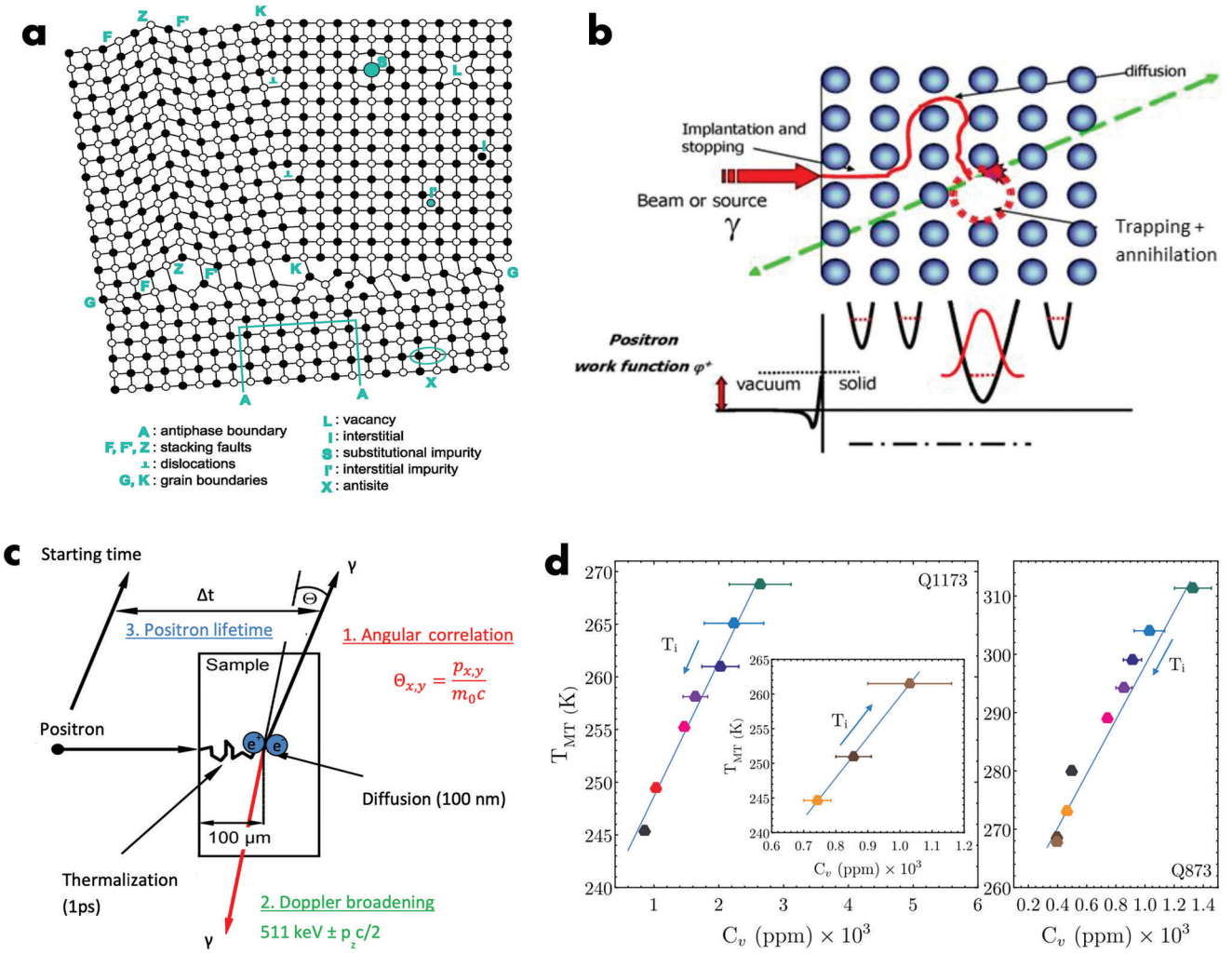

Figure 16. a) Schematic structure of ordered crystals showing the different types of lattice defects.[438] Reproduced under the terms of the CC-BY-NC-ND 4.0. license. Copyright 2023, American Chemical Society. b) Potential well for a positron in a perfect lattice and vacancy defect in a lattice. When the positron is trapped at neutral or negatively charged open-volume defects, the wave function of positron is localized at the defect because the Coulomb repulsion is decreased due to the missing ion core. This will lower the potential sensed by the positron creating a local potential well. Besides, when the trapping happens, the overlap of the wavefunction of positrons and core electrons is strongly reduced while wavefunction of valence electrons extends farther into the open space, which leads to increased annihilation probability with valence electrons and a corresponding sharper momentum distribution. c) Schematic overview of positron annihilation and three widely used PAS techniques, where θ is angle and p are the momentum components. c,d) Reproduced under the terms of CC-BY license.[439] Copyright 2018, W. Shi. d) T_{MT} as a function of vacancy concentration (C_v) for the samples (left: Q1173-quenching from 1173 K; right: Q873-quenching from 873 K). The inset is the corresponded enlarged display. Reproduced with permission.[238] Copyright 2019, American Physical Society.

widely applied for defect characterization among different functional materials. Here, we limit our scenario only to MCMs since the lattice defects play important roles in magnetism and phase transition,[428,429] as illustrated by recent studies on the MCE in Ni-based magnetic Heusler compounds,[236–238,430–433] FeRh,[434] and magnetic oxide ceramics.[435,436] Merida et al.[431] studied the influence of quenched-in defects from different quenching temperatures (673-1173 K) and the annealing treatments in $Ni_{53}Mn_{26}Ga_{21}$ compound. The PAS results show that the concentration of retained vacancies becomes higher with increasing the quenching temperature. And the initial vacancy concentration of samples (poly-crystal/single-crystal) quenched from 1173 K range between 1000 and 2000 ppm.[432] Similarly, Unzueta et al.[237] applied PALS measurements complemented with DFT electron-positron theoretical calculations in $Ni_{50}Mn_{50-x}Sn_x$ ($x = 25, 20, 15, 13, 10$) and $Ni_{50}Mn_{50-y}In_y$ ($y = 25, 20, 16, 13$) samples to identify the vacancy defects. Combining theory and experiments, it is found that Ni vacancies (V_{Ni}) are the main type of lattice defects (concentration ≥ 500 ppm) in NiMn-Z (Z = Ga, Sn, In) samples. The characteristic V_{Ni}-related positron lifetime ranges from 181 to 191 ps. Furthermore, the same group of authors[238] further experimentally demonstrated a direct relationship between vacancies and the shift in the martensitic transformation temperature (T_{MT}) in a $Ni_{55}Fe_{17}Ga_{28}$ alloy utilizing PALS. As shown in Figure 16d, it is noted that the vacancy concentration can be helpful for the fine-tuning of T_{MT}, e.g., resulting

© 2024 Wiley-VCH GmbH

16146840, 0, Downloaded from https://onlinelibrary.wiley.com/doi/10.1002/aenm.202400369 by Tu Delft, Wiley Online Library on [08/04/2024]. See the Terms and Conditions (https://onlinelibrary.wiley.com/terms-and-conditions) on Wiley Online Library for rules of use; OA articles are governed by the applicable Creative Commons License

in shifts up to ≈50 K. This highlights the importance of the often neglected lattice defects in tuning T_{MT} in Ni-based martensitic alloys. The PALS measurements, together with electron-positron DFT calculations, confirm that V_{Ni} are also the most probable defects responsible for changes in the transition temperature of NiFeGa compounds. Based on the HRTEM and PAS results, Zhang et al.[236] demonstrated that vacancy-type lattice defects are widely present in the all-*d*-metal NiCoMnTi Heusler compounds, which suggests that defect engineering can be applied to control the GMCE. Additionally, it is interesting to consider the possibility that changes in the nature of the itinerant electrons take place across the phase transition by modifications in the electron density of states (DOS) near the Fermi level. Significant changes in the DOS would presumably affect the momentum space distribution and should therefore be detectable, e.g., by the positron AC method.[437] However, Zimmer et al.[437] did not find significant changes in the electronic structure of FeRh during AFM to FM transition, although they cannot exclude the possibility that the effect is strongly reduced by averaging over all crystallographic directions in the polycrystalline sample. Moreover, the shape of the minority spin Fermi surface of Ni_2MnGa compounds has been verified experimentally using 2D angular correlation of positron annihilation radiation (2D-ACAR), which can provide a projection of the underlying 3D electron-positron momentum density.[430] The momentum distribution contains information about the occupied regions of reciprocal space, and hence about the Fermi surface.[430] Interestingly, the authors point out that the found Fermi surface nesting is only part of the process that leads electrons to destabilize the lattice. This process is able to greatly enhance the effect of electron-phonon coupling for particular wavevectors, which could play an important role in determining the atomic modulations associated with the various martensitic phenomena.

4.5. High Magnetic Pulse Fields

How to precisely determine the ΔT_{ad} under strictly adiabatic conditions, one of the most important parameters for the evaluation of MCE performance, is pivotal for the development of MCMs. Also, combined time-dependent experimental magnetization changes and ΔT_{ad} until the completely transformed state are of key importance to understand the dynamics of the phase transition and the physical properties behind it. Recently, high magnetic pulse fields have become a workable method for the investigations of MCMs.[440] The short duration of magnetic-field pulses (10–100 ms) ensures the adiabatic condition for the determination of ΔT_{ad}, and it also matches the targeted operation frequency of magnetic refrigerators (10–100 Hz).[441,442] The possibility to measure in wide temperature range (10 – 400 K) allows us to investigate MCMs from near room-temperature applications to low-temperature gas liquefaction.[440] Most FOMT materials can be transformed completely in field strengths up to 50 T and beyond.[440] Moreover, the high field-change rates offer us the possibilities to observe the dynamic effects of phase transitions driven by nucleation and growth. In **Figure 17a**, the main components for the pulsed high magnetic fields and the typical time dependence of a pulsed field are exhibited. The setup for direct pulse-field measurements of ΔT_{ad} is shown in Figure 17b. The experimental methods related to the pulsed high magnetic fields have been applied for several MCMs such as Ho_2Fe_{17},[443] rare earth-based Laves phase compounds,[90,444,445] Gd,[446,447] $MnFe_4Si_3$,[448] FeRh,[449] $(Mn,Fe)_2(P,Si)$,[450] MnCoSi,[451] $La(Fe, Si)_{13}$,[452] and NiMn-based Heusler compounds.[441,442,453–455] Technical details and advances about the pulsed high magnetic fields on different MCMs have recently been reviewed.[440] In this subsection, the following examples of MCMs in pulsed magnetic fields are discussed:

Zavareh and co-workers[452] performed magnetization, magnetostriction, and MCE measurements in magnetic fields up to 60 T for two $LaFe_{11.74}Co_{0.13}Si_{1.13}$ (FOMT) and $LaFe_{11.21}Co_{0.65}Si_{1.11}$ (SOMT) samples. In both compounds, the highest reached ΔT_{ad} was 20 K at 50 T. The magnetoelastic coupling is quantified using the magnetostriction data (based on a general local-moment volume magnetostriction theory). The type of phase transition for the two compounds is distinguished using the Bean-Rodbell criterion. As shown in Figure 17c, Gottschall et al.[446] applied the direct measurements of ΔT_{ad} in the benchmark material Gd in pulsed high magnetic fields up to 62 T, where a very large ΔT_{ad} = 60.5 K is observed. The field-dependent ΔT_{ad} is found to follow the familiar mean-field expression with a leading term in $H^{2/3}$ and a correction term in $H^{4/3}$. The calculations predict a complete disappearance of the maximum ΔT_{ad} near T_C in higher fields (140 T) and an emergence of a new very broad maximum far above T_C. Nevertheless, Zhang et al.[451] directly measured ΔT_{ad} in different initial temperatures (down to 18 K) and pulsed magnetic fields (up to 40 T) in the strong magnetoelastic coupled $Mn_{1.02}Co_{0.98}Si$ compound. These measurements presented a moderate MCE performance (maximum $\Delta T_{ad} = -3.1$ K for $\Delta\mu_0 H = 13$ T). Furthermore, the magnetization measurements in pulsed (and static) magnetic fields indicate that the ME coupling is significantly enhanced for increasing fields, resulting in an improved saturation magnetization. The metamagnetic transition is continuously pushed to lower temperatures in higher fields. As shown in Figure 17d, the phase diagram constructed from the experimental transition temperatures T_t and the critical magnetic fields $\mu_0 H_{cr}$ indicate that the transition is terminated below 18 K and that ferromagnetism is stabilized for fields above 22.3 T. The saturation of $\mu_0 H_{cr}$ at low temperatures is understood in terms of the energy barrier for nucleation. This study reveals how the strong ME coupling changes under pulsed magnetic fields in a representative MnCoSi sample, which provides unique insights into these MCMs and their behavior in high magnetic fields.

In this section, we demonstrated the effectiveness of different large-scale scientific facilities and emphasized the importance of multimodal studies with different techniques. For instance, neutron scattering and the synchrotron X-ray techniques are both versatile tools to investigate matter on length scales ranging all the way from a subatomic scale through nano and micrometer extensions to macroscopic entities that often provide complementary information. Some other lab-based techniques like advanced electron microscopies (special aberration-corrected transmission electron microscope (AC-TEM), scanning transmission electron microscopy (STEM)) and high-resolution Mössbauer spectroscopy can provide structural information in real space and probe changes in the local coordination environment in energy domain across the phase transition. The

© 2024 Wiley-VCH GmbH

16146840, 0, Downloaded from https://onlinelibrary.wiley.com/doi/10.1002/aenm.202400369 by Tu Delft, Wiley Online Library on [08/04/2024]. See the Terms and Conditions (https://onlinelibrary.wiley.com/terms-and-conditions) on Wiley Online Library for rules of use; OA articles are governed by the applicable Creative Commons License

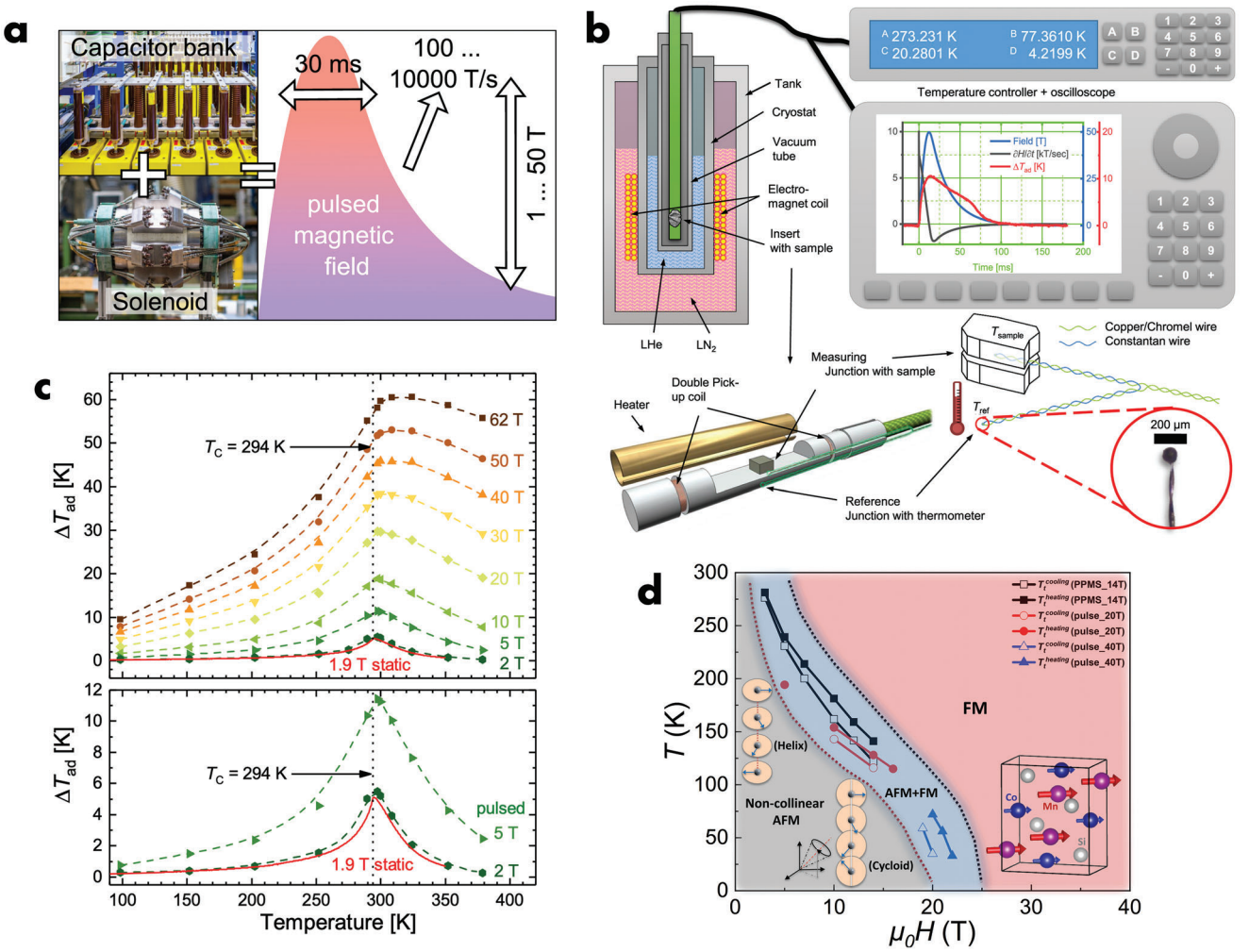

Figure 17. a) Left: main components (large capacitor bank and non-destructive solenoids) for the high magnetic pulse fields up to 95 T. Right: the typical time dependence of a pulsed field.[440] Note that the high static magnetic fields can be generated through resistive coils in the range of 30–35 T, and larger static magnetic fields (up to 40–45 T) can be produced by hybrid magnets.[456] b) Experimental set-up for direct pulse-field measurements of the ΔT_{ad}.[440] a,b) Reproduced under the terms of the CC BY license. Copyright 2023, Author(s). c) Top: ΔT_{ad} as a function of temperature in different magnetic fields for pure Gd. The solid line points to the ΔT_{ad} under quasistatic conditions. Bottom: the low-field region. Reproduced with permission.[446] Copyright 2019, American Physical Society. d) Phase diagram T-$\varepsilon_0 H$ constructed from T_t as a function of the $\varepsilon_0 H$ (combining the static and pulse fields) for the $Mn_{1.02}Co_{0.98}Si$ compound. The inset shows the orthorhombic structure for the MnCoSi system. Reproduced with permission.[451] Copyright 2023, American Physical Society.

combination of the modalities of different advanced characterization techniques enables us to obtain multiple sources of information in spatial and time scale in unprecedented detail and helps shed light on the physics responsible for the MCE in new emerging MCMs. It demonstrates their importance in boosting the development of advanced MCMs and will continue to open up new opportunities to tackle diverse scientific problems related to the MCE.

5. Opportunities, Challenges, and Perspective

With the further development of advanced characterization techniques and improved computational abilities (big data science), it is believed that the understanding, finding, and designing of new MCMs will be accelerated. For example, the currently known MCMs are mainly found by low-efficiency trial-and-error experiments that typically rely on empirical structure-property relationships, which always require a significant investment in time and resources.[457] Alternatively, high-throughput computational screening based on DFT calculations has been successfully applied to provide accurate and time-effective predictions of new MCMs and their magnetic properties with the input of a relatively small amount of experimental data from various databases.[457–460] On the other hand, the emerging artificial intelligence (AI) computation techniques, such as machine learning (ML) and deep learning (DL), have extended their abilities to the field of magnetocaloric energy conversion, resulting in the discovery of MCMs[168,169,461–464] or the optimization of magnetocaloric prototypes.[465–467] For instance, training the ML algorithm in $(Mn,Fe)_2(P,Si)$ based materials predicted

© 2024 Wiley-VCH GmbH

16146840, 0, Downloaded from https://onlinelibrary.wiley.com/doi/10.1002/aenm.202400369 by Tu Delft, Wiley Online Library on [08/04/2024]. See the Terms and Conditions (https://onlinelibrary.wiley.com/terms-and-conditions) on Wiley Online Library for rules of use; OA articles are governed by the applicable Creative Commons License

optimized compositions that showed an excellent MCE.[168,169] In addition, the GMCE working window can thereby be further expanded to cryogenic magnetic refrigeration (below 77 K), which had never been achieved before.[168] Meanwhile, advanced manufacturing technologies like additive manufacturing (AM) have shown substantial advances in recent years, which has with the aid of digital design guided the energy sources to consolidate feedstock materials layer by layer to build various 3D objects.[468] This AM approach can overcome the challenges associated with the fabrication of complex regenerator architectures with a large surface-to-volume ratio. Moreover, it can assist in the design of intricate and complex geometrical structures for specific magnetocaloric energy conversation scenarios. In addition, it may also offer solutions to some long-standing issues related to MCMs, such as brittleness and phase inhomogeneities, by precise manipulation of microstructure using a rapid solidification rate in a highly localized region.[43] For example, Hou et al.[469] introduced the powder-feed laser-directed-energy deposition (a kind of AM technique) to optimize the Ni–Ti-based elastocaloric materials and engineer the eutectic nanocomposite microstructure with high materials efficiency, extremely small hysteresis, and remarkable extended fatigue life (the repeatable caloric performance extended over 1 million cycles). Beyond doubt, the abovementioned intelligent computation with characteristics of lower cost, time saving, effectiveness, and precision, integrated with advanced manufacturing like AM,[470] would definitely boost the objective of topological optimization and discovery of MCMs, and further facilitate and strengthen practical implementation of magnetocaloric techniques for energy conservation and environmental friendliness. To achieve real industrialization for magnetocaloric products, several challenges should be addressed: i) designing and finding better MCMs, ii) developing suitable low-cost (rare-earth free) strong permanent magnetic fields, iii) optimizing systems and manufacturing costs. About the advanced MCMs, different perspectives like reversibility, availability, criticality, and corrosion-resistance should give priority. Since the magnetic field source is the most expensive part of any magnetocaloric conversion device, the volume of applied magnetic sources should be used as efficiently as possible.[36] In the past 10 years, encouraging progress has been made in solid-state magnetocaloric energy conversion, continuously hosting great potential for providing greener alternatives to existing air-compression technologies. For the next 10 years, the research on the magnetocaloric effect is expected to profit from the rapid evolution in advanced experimental characterization techniques, progressive manufacturing technologies, and notable advances in high-performance computational methods. It is expected that the gap between the advanced MCMs and the cutting-edge engineering technologies will be bridged to bring this technology towards large-scale applications.

Acknowledgements

F.Q.Z. greatly appreciates the supervision of N. van Dijk and E. Brück during his Ph.D. F.Q.Z also appreciates the inspiring discussions with Y.R. The authors greatly thank the discussions with R. I. Smith, M. Avdeev, D. Vadim, D. Chernyshov, E. Bykov, and T. Gottschall. This work was supported by the open research fund of CSNS (Grant No. KFKT2022B04, KFKT2022A05). F.Q.Z. and Y.R. acknowledge financial support from the City University of Hong Kong (Project No. 9610533). X.F.M. acknowledges financial support from the National Natural Science Foundation of China (Grant No. U1832191).)

Conflict of Interest

The authors declare no conflict of interest.

Keywords

advanced characterization, magnetocaloric energy conversion, magnetocaloric material, multimodal studies

Received: January 23, 2024
Revised: February 20, 2024
Published online:

[1] International Energy Agency, The Future of Cooling: Opportunities for Energy-efficient Air Conditioning Report, **2018**.
[2] J. N. Li, A. Torelló, V. Kovacova, U. Prah, A. Aravindhan, T. Granzow, T. Usui, S. Hirose, E. Defay, *Science* **2023**, *382*, 801.
[3] J. Lyubina, *J. Phys. D Appl. Phys.* **2017**, *50*, 053002.
[4] International Renewable Energy Agency, World Energy Transitions Outlook 2023: 1.5°C Pathway, Vol. *1*, **2023**.
[5] P. Patel, O. Gutfleisch, *MRS Bull.* **2018**, *43*, 918.
[6] European Commission, EU 2050 long-term strategy, https://ec.europa.eu/clima/eu-action/climate-strategies-targets/2050-long-term-strategy_en (accessed: October 2023).
[7] People's Republic of China State Council Information Office, China's policies and actions to address climate change, https://www.gov.cn/zhengce/2021-10/27/content_5646697.htm (accessed: October 2023).
[8] O. Gutfleisch, M. A. Willard, E. Brück, C. H. Chen, S. G. Sankar, J. P. Liu, *Adv. Mater.* **2011**, *23*, 821.
[9] V. Franco, J. S. Blazquez, J. J. Ipus, J. Y. Law, L. M. Moreno-Ramirez, A. Conde, *Prog. Mater. Sci.* **2018**, *93*, 112.
[10] V. K. Pecharsky, K. A. Gschneidner, *Phys. Rev. Lett.* **1997**, *78*, 4494.
[11] O. Tegus, E. Brück, K. H. J. Buschow, F. R. de Boer, *Nature* **2002**, *415*, 150.
[12] F. X. Hu, B. G. Shen, J. R. Sun, X. X. Zhang, *Chinese Phys.* **2000**, *9*, 550.
[13] H. Johra, K. Filonenko, P. Heiselberg, C. Veje, S. Dall'Olio, K. Engelbrecht, C. Bahl, *Renew Energy* **2019**, *136*, 115.
[14] M. Gueltig, F. Wendler, H. Ossmer, M. Ohtsuka, H. Miki, T. Takagi, M. Kohl, *Adv. Energy Mater.* **2017**, *7*, 1601879.
[15] A. Waske, D. Dzekan, K. Sellschopp, D. Berger, A. Stork, K. Nielsch, S. Fähler, *Nat. Energy* **2019**, *4*, 68.
[16] P. Weiss, A. Piccard, *J. Theor. Appl. Phys.* **1917**, *7*, 103.
[17] W. F. Giauque, D. P. MacDougall, *Phys. Rev.* **1933**, *43*, 0768.
[18] P. Debye, *Ann. Phys.* **1926**, *386*, 1154.
[19] W. F. Giauque, *J. Am. Chem. Soc.* **1927**, *49*, 1864.
[20] A. Tiselius, Presentation Speech, **1949**, Nobel prize chem.
[21] G. V. Brown, *J. Appl. Phys.* **1976**, *47*, 3673.
[22] S. S. Rosenblum, W. A. Steyert, W. P. Pratt, *Los Alamos National Lab.* **1977**.
[23] M. P. Annaorazov, K. A. Asatryan, G. Myalikgulyev, S. A. Nikitin, A. M. Tishin, A. L. Tyurin, *Cryogenics* **1992**, *32*, 867.
[24] M. P. Annaorazov, S. A. Nikitin, A. L. Tyurin, K. A. Asatryan, A. K. Dovletov, *J. Appl. Phys.* **1996**, *79*, 1689.
[25] Z. B. Guo, Y. W. Du, J. S. Zhu, H. Huang, W. P. Ding, D. Feng, *Phys. Rev. Lett.* **1997**, *78*, 1142.

 © 2024 Wiley-VCH GmbH

16146840, 0, Downloaded from https://onlinelibrary.wiley.com/doi/10.1002/aenm.202400369 by Tu Delft, Wiley Online Library on [08/04/2024]. See the Terms and Conditions (https://onlinelibrary.wiley.com/terms-and-conditions) on Wiley Online Library for rules of use; OA articles are governed by the applicable Creative Commons License

[26] V. K. Pecharsky, *Nat. Mater.* **2016**, *15*, 1059.
[27] A. Smith, *Eur. Phys. J H* **2013**, *38*, 507.
[28] A. Kitanovski, *Adv. Energy Mater.* **2020**, *10*, 1903741
[29] F. X. Hu, B. G. Shen, J. R. Sun, Z. H. Cheng, G. H. Rao, X. X. Zhang, *Appl. Phys. Lett.* **2001**, *78*, 3675.
[30] A. Planes, L. Manosa, M. Acet, *J. Phys.-Condens Mat.* **2009**, *21*, 233201.
[31] J. Liu, T. Gottschall, K. P. Skokov, J. D. Moore, O. Gutfleisch, *Nat. Mater.* **2012**, *11*, 620.
[32] N. T. Trung, L. Zhang, L. Caron, K. H. J. Buschow, E. Brück, *Appl. Phys. Lett.* **2010**, *96*, 172504.
[33] E. K. Liu, W. H. Wang, L. Feng, W. Zhu, G. J. Li, J. L. Chen, H. W. Zhang, G. H. Wu, C. B. Jiang, H. B. Xu, F. de Boer, *Nat. Commun.* **2012**, *3*, 873.
[34] X. Moya, N. D. Mathur, *Science* **2020**, *370*, 797.
[35] L. Mañosa, A. Planes, *Adv. Mater.* **2017**, *29*, 1603607.
[36] T. Gottschall, K. P. Skokov, M. Fries, A. Taubel, I. Radulov, F. Scheibel, D. Benke, S. Riegg, O. Gutfleisch, *Adv. Energy Mater.* **2019**, *9*, 1901322.
[37] V. Chaudhary, X. Chen, R. V. Ramanujan, *Prog. Mater. Sci.* **2019**, *100*, 64.
[38] X. Moya, S. Kar-Narayan, N. D. Mathur, *Nat. Mater.* **2014**, *13*, 439.
[39] A. Smith, C. R. H. Bahl, R. Bjork, K. Engelbrecht, K. K. Nielsen, N. Pryds, *Adv. Energy Mater.* **2012**, *2*, 1288.
[40] A. Greco, C. Aprea, A. Maiorino, C. Masselli, *Int J Refrig* **2019**, *106*, 66.
[41] L. Mañosa, A. Planes, *Appl. Phys. Lett.* **2020**, *116*, 050501.
[42] A. Alahmer, M. Al-Amayreh, A. O. Mostafa, M. Al-Dabbas, H. Rezk, *Energies* **2021**, *14*, 4662.
[43] H. L. Hou, S. X. Qian, I. Takeuchi, *Nat. Rev. Mater.* **2022**, *7*, 633.
[44] J. Mao, G. Chen, Z. F. Ren, *Nat. Mater.* **2021**, *20*, 454.
[45] T. Correia, Q. Zhang, *Electrocaloric Materials New Generation of Coolers*, Springer, Berlin **2014**.
[46] Fraunhofer IPM, Magnetocaloric system, https://www.ipm.fraunhofer.de/en/bu/energy-converters-thermal/expertise/caloric-systems/magnetocaloric-systems.html (accessed: October 2023).
[47] Y. K. Zhang, J. H. Wu, J. He, K. Wang, G. X. Yu, *Renew. Sust. Energy Rev.* **2021**, *143*, 110933.
[48] General Electric, Not Your Average Fridge Magnet: These High-Tech Magnets Will Keep Your Butter (and Beer) Cold, https://www.ge.com/news/reports/not-your-average-fridge-magnet (accessed: October 2023).
[49] K. Lawler, Premiere of Cutting-Edge Cooling Appliance at CES **2015**, https://www.astronautics.com/premiere-of-cutting-edge-cooling-appliance-at-ces-2015/ (accessed: October 2023).
[50] M. Irving, Magnetic fridge eliminates gases drastically reduces energy use, https://newatlas.com/cooltech-commercial-magnetic-cooling/43874/ (accessed: October 2023).
[51] S. Lionte, M. Risser, C. Muller, *International Journal of Refrigeration* **2021**, *122*, 256.
[52] A. T. D. Nakashima, F. P. Fortkamp, N. M. de Sá, V. M. A. dos Santos, G. Hoffmann, G. F. Peixer, S. L. Dutra, M. C. Ribeiro, J. A. Lozano, J. R. Barbosa, *Int. J. Refrig.* **2021**, *122*, 110.
[53] G. F. Peixer, M. C. R. Silva, A. Lorenzoni, G. Hoffmann, D. dos Santos, G. M. do Rosário, E. Pagnan, H. F. Teza, P. M. Silva, S. L. Dutra, M. C. Ribeiro, M. A. A. Rosa, A. Döring, B. P. Vieira, A. T. D. Nakashima, P. A. P. Wendhausen, C. S. Teixeira, J. A. Lozano, J. R. Barbosa, *Int. J. Refrig.* **2023**, *151*, 1.
[54] B. F. Yu, M. Liu, P. W. Egolf, A. Kitanovski, *Int. J. Refrig.* **2010**, *33*, 1029.
[55] H. Johra, K. Filonenko, P. Heiselberg, C. Veje, T. Lei, S. Dall'Olio, K. Engelbrecht, C. Bahl, *Build Simul.-China* **2018**, *11*, 753.
[56] S. Dall'Olio, M. Masche, J. Liang, A. R. Insinga, D. Eriksen, R. Bjork, K. K. Nielsen, A. Barcza, H. A. Vieyra, N. V. Beek, H. N. Bez, K. Engelbrecht, C. R. H. Bahl, *Int. J. Refrig.* **2021**, *132*, 243.
[57] D. P. Quijano, C. I. Ferreira, E. Bruck, *Appl. Therm. Eng.* **2023**, *232*, 120962.
[58] B. Huang, J. W. Lai, D. C. Zeng, Z. G. Zheng, B. Harrison, A. Oort, N. H. van Dijk, E. Brück, *Int. J. Refrig.* **2019**, *104*, 42.
[59] Z. G. Qi, *Renew. Sust. Energy Rev.* **2014**, *38*, 754.
[60] B. Torregrosa-Jaime, J. M. Corberán, C. Vasile, C. Muller, M. Risser, J. Payá, *Int. J. Refrig.* **2014**, *37*, 156.
[61] C. Zimm, A. Boeder, B. Mueller, K. Rule, S. L. Russek, *MRS Bull.* **2018**, *43*, 274.
[62] T. V. Christiaanse, Ph.D. thesis, University of Victoria, **2018**.
[63] S. Nosan, U. Tomc, J. Klemenc, A. Kitanovski, *J. Magn. Magn. Mater.* **2023**, *584*, 171121.
[64] A. Firth, B. Zhang, A. D. Yang, *Appl. Energy* **2019**, *235*, 1314.
[65] D. Enescu, E. O. Virjoghe, *Renew. Sust. Energy Rev.* **2014**, *38*, 903.
[66] T. A. Edison, U.S. Patent 380100A **1888**.
[67] T. A. Edison, U.S. Patent 476983A **1892**.
[68] J. Stefan, *Ann. Phys.* **1889**, *274*, 427.
[69] N. Tesla, U.S. Patent 396121A **1889**.
[70] N. Tesla, U.S. Patent 428057A **1890**.
[71] L. Brillouin, H. Iskenderian, *Electrical Commun.* **1948**, *25*, 300.
[72] L. D. Kirol, J. I. Mills, *J. Appl. Phys.* **1984**, *56*, 824.
[73] T. Christiaanse, E. Brück, *Metallurgical and Materials Transactions E* **2014**, *1*, 36.
[74] S. Hur, S. Kim, H. S. Kim, A. Kumar, C. Kwon, J. Shin, H. Kang, T. H. Sung, J. Ryu, J. M. Baik, H. C. Song, *Nano Energy* **2023**, *114*, 108596.
[75] R. A. Kishore, S. Priya, *Renew. Sust. Energy Rev.* **2018**, *81*, 33.
[76] J. Joseph, E. Fontana, T. Devillers, N. M. Dempsey, M. Kohl, *Adv. Funct. Mater.* **2023**, *33*, 2301250.
[77] C. Rodrigues, A. Pires, I. Gonçalves, D. Silva, J. OIiveira, A. Pereira, J. Ventura, *Adv. Funct. Mater.* **2022**, *32*, 2110288.
[78] X. L. Liu, H. Zhang, H. D. Chen, Z. H. Ma, K. M. Qiao, L. L. Xie, Z. Q. Ou, J. Wang, F. X. Hu, B. G. Shen, *Appl. Therm. Eng.* **2023**, *221*, 119827.
[79] J. Joseph, M. Ohtsuka, H. Miki, M. Kohl, *Joule* **2020**, *4*, 2718.
[80] L. Fink, K. Nielsch, S. Fahler, *J. Alloy Compd.* **2023**, *966*, 171435.
[81] H. D. Chen, Z. H. Ma, X. L. Liu, K. M. Qiao, L. L. Xie, Z. X. Li, J. Shen, W. Dai, Z. Q. Ou, H. Yibole, O. Tegus, S. V. Taskaev, K. Chu, Y. Long, H. Zhang, *Appl. Energy* **2022**, *306*, 117999.
[82] S. Ahmim, M. Almanza, V. Loyau, F. Mazaleyrat, A. Pasko, F. Parrain, M. LoBue, *J. Magn. Magn. Mater.* **2021**, *540*, 168428.
[83] D. Dzekan, A. Diestel, D. Berger, K. Nielsch, S. Fähler, *Sci. Technol. Adv. Mater.* **2021**, *22*, 643.
[84] M. Fries, Z. Gercsi, S. Ener, K. P. Skokov, O. Gutfleisch, *Acta Mater.* **2016**, *113*, 213.
[85] D. Dzekan, A. Waske, K. Nielsch, S. Fähler, *APL Mater.* **2021**, *9*, 011105.
[86] X. L. Liu, H. D. Chen, J. Y. Huang, K. M. Qiao, Z. Y. Yu, L. L. Xie, R. V. Ramanujan, F. X. Hu, K. Chu, Y. Long, H. Zhang, *Nat. Commun.* **2023**, *14*, 4811.
[87] T. Numazawa, K. Kamiya, T. Utaki, K. Matsumoto, *Cryogenics* **2014**, *62*, 185.
[88] H. Zhang, R. Gimaev, B. Kovalev, K. Kamilov, V. Zverev, A. Tishin, *Physica B* **2019**, *558*, 65.
[89] N. Terada, H. Mamiya, *Nat. Commun.* **2021**, *12*, 1212.
[90] W. Liu, E. Bykov, S. Taskaev, M. Bogush, V. Khovaylo, N. Fortunato, A. Aubert, H. B. Zhang, T. Gottschall, J. Wosnitza, F. Scheibel, K. Skokov, O. Gutfleisch, *Appl. Mater. Today* **2022**, *29*, 101624.
[91] F. Guillou, A. K. Pathak, D. Paudyal, Y. Mudryk, F. Wilhelm, A. Rogalev, V. K. Pecharsky, *Nat. Commun.* **2018**, *9*, 2925.
[92] W. Liu, F. Scheibel, T. Gottschall, E. Bykov, I. Dirba, K. Skokov, O. Gutfleisch, *Appl. Phys. Lett.* **2021**, *119*, 022408.

© 2024 Wiley-VCH GmbH

16146840, 0, Downloaded from https://onlinelibrary.wiley.com/doi/10.1002/aenm.202400369 by Tu Delft, Wiley Online Library on [08/04/2024]. See the Terms and Conditions (https://onlinelibrary.wiley.com/terms-and-conditions) on Wiley Online Library for rules of use; OA articles are governed by the applicable Creative Commons License

[93] C. Archipley, J. Barclay, K. Meinhardt, G. Whyatt, E. Thomsen, J. Holladay, J. Cui, I. Anderson, S. Wolf, *Cryogenics* **2022**, *128*, 103588.
[94] J. Barclay, K. Brooks, J. Cui, J. Holladay, K. Meinhardt, E. Polikarpov, E. Thomsen, *Cryogenics* **2019**, *100*, 69.
[95] H. Ansarinasab, M. Fatimah, Y. Khojasteh-Salkuyeh, *J. Energy Storage* **2023**, *65*, 107304.
[96] EU project, https://www.hylical.eu/, **2022**.
[97] A. Usman, F. Xiong, W. Aftab, M. L. Qin, R. Q. Zou, *Adv. Mater.* **2022**, *34*, 2202457.
[98] T. B. Freeman, K. E. O. Foster, C. J. Troxler, C. W. Irvin, A. Aday, S. K. S. Boetcher, A. Mahvi, M. K. Smith, A. Odukomaiya, *Adv. Energy Mater.* **2023**, *13*, 2204208.
[99] S. W. Li, L. H. He, H. L. Lu, J. Z. Hao, D. K. Wang, F. R. Shen, C. Song, G. J. Liu, P. F. Du, Y. D. Wang, D. Y. Cong, *Acta Mater.* **2023**, *249*, 118852.
[100] D. J. Sharar, B. F. Donovan, R. J. Warzoha, A. A. Wilson, A. C. Leff, B. M. Hanrahan, *Appl. Phys. Lett.* **2019**, *114*, 143902.
[101] O. Dumont, G. F. Frate, A. Pillai, S. Lecompte, M. De Paepe, V. Lemort, *J. Energy Storage* **2020**, *32*, 101756.
[102] Z. Zhang, K. Li, S. C. Lin, R. Q. Song, D. H. Yu, Y. D. Wang, J. F. Wang, S. Kawaguchi, Z. Zhang, C. Y. Yu, X. D. Li, J. Chen, L. H. He, R. Mole, B. Yuan, Q. Y. Ren, K. Qian, Z. L. Cai, J. G. Yu, M. C. Wang, C. Y. Zhao, X. Tong, Z. D. Zhang, B. Li, *Sci. Adv.* **2023**, *9*, eadd037.
[103] J. Liu, J. Y. Li, *J. Magn. Magn. Mater.* **2022**, *564*, 170183.
[104] N. Petelin, K. Vozel, K. Klinar, A. Kitanovski, *Iscience* **2022**, *25*, 105517.
[105] S. Pajovic, S. V. Boriskina, *Phys. Rev. Appl.* **2023**, *20*, 014053.
[106] D. N. Ba, Y. L. Zheng, L. Becerra, M. Marangolo, M. Almanza, M. LoBue, *Phys. Rev. Appl.* **2021**, *15*, 064045.
[107] H. Han, A. Kan, Y. Jin, P. Xia, W. Tang, China. Patent CN202297193-U **2012**.
[108] S. Arora, *J. Power Sources* **2018**, *400*, 621.
[109] M. Al-Nimr, O. Haddad, L. Al-Samamah, *Energy* **2023**, *283*, 129131.
[110] M-ERA.NET, https://www.m-era.net/materipedia/2021/coolbatman, **2022**.
[111] Y. Jung, M. Kim, T. Kim, J. Ahn, J. W. Lee, S. H. Ko, *Nano-Micro Lett.* **2023**, *15*, 160.
[112] F. Q. Zhang, C. Taake, B. W. Huang, X. M. You, H. Ojiyed, Q. Shen, I. Dugulan, L. Caron, N. van Dijk, E. Brück, *Acta Mater.* **2022**, *224*, 117532.
[113] J. H. Belo, A. L. Pires, J. P. Araújo, A. M. Pereira, *J. Mater. Res.* **2019**, *34*, 134.
[114] I. Nkurikiyimfura, Y. M. Wang, Z. D. Pan, *Renew. Sust. Energy Rev.* **2013**, *21*, 548.
[115] S. Pal, A. Datta, S. Sen, A. Mukhopdhyay, K. Bandopadhyay, R. Ganguly, *J. Magn. Magn. Mater.* **2011**, *323*, 2701.
[116] A. Kitanovski, P. W. Egolf, *Int. J. Refrig.* **2010**, *33*, 449.
[117] V. Chaudhary, Z. Wang, A. Ray, I. Sridhar, R. V. Ramanujan, *J. Phys. D Appl. Phys.* **2017**, *50*, 03LT03.
[118] K. Rajamani, E. Juffermans, L. Granelli, A. D. C. Rabaneda, W. Rohlfs, M. ter Brake, T. van der Meer, M. Shahi, *Appl. Energ.* **2024**, *355*, 122253.
[119] Y. S. Li, M. Garst, J. Schmalian, S. Ghosh, N. Kikugawa, D. A. Sokolov, C. W. Hicks, F. Jerzembeck, M. S. Ikeda, Z. H. Hu, B. J. Ramshaw, A. W. Rost, M. Nicklas, A. P. Mackenzie, *Nature* **2022**, *607*, 276.
[120] A. W. Rost, R. S. Perry, J. F. Mercure, A. P. Mackenzie, S. A. Grigera, *Science* **2009**, *325*, 1360.
[121] M. S. Reis, N. Ma, *Phys. Open* **2020**, *4*, 100028.
[122] Z. Y. Wei, E. K. Liu, J. H. Chen, Y. Li, G. D. Liu, H. Z. Luo, X. K. Xi, H. W. Zhang, W. H. Wang, G. H. Wu, *Appl. Phys. Lett.* **2015**, *107*, 022406.
[123] A. Chirkova, K. P. Skokov, L. Schultz, N. V. Baranov, O. Gutfleisch, T. G. Woodcock, *Acta Mater.* **2016**, *106*, 15.
[124] P. A. E. Murgatroyd, K. Routledge, S. Durdy, M. W. Gaultois, T. W. Surta, M. S. Dyer, J. B. Claridge, S. N. Savvin, D. Pelloquin, S. Hébert, J. Alaria, *Adv. Funct. Mater.* **2021**, *31*, 2100108.
[125] J. Y. Law, V. Franco, *J. Mater. Res.* **2023**, *38*, 37.
[126] F. Scheibel, T. Gottschall, A. Taubel, M. Fries, K. P. Skokov, A. Terwey, W. Keune, K. Ollefs, H. Wende, M. Farle, M. Acet, O. Gutfleisch, M. E. Gruner, *Energy Technol-Ger* **2018**, *6*, 1397.
[127] J. B. Goodenough, *J. Solid State Chem.* **1973**, *7*, 428.
[128] S. Rundqvist, F. Jellinek, *Acta Chem. Scand.* **1959**, *13*, 425.
[129] R. Wappling, L. Haggstrom, T. Ericsson, S. Devanarayanan, E. Karlsson, B. Carlsson, S. Rundqvist, *J. Solid State Chem.* **1975**, *13*, 258.
[130] L. Lundgren, G. Tarmohamed, O. f. Beckman, B. Carlsson, S. Rundqvist, *Phys. Scr.* **1978**, *17*, 39.
[131] R. Zach, M. Guillot, R. Fruchart, *J. Magn. Magn. Mater.* **1990**, *89*, 221.
[132] M. Bacmann, J. L. Soubeyroux, R. Barrett, D. Fruchart, R. Zach, S. Niziol, R. Fruchart, *J. Magn. Magn. Mater.* **1994**, *134*, 59.
[133] D. T. C. Thanh, E. Brück, O. Tegus, J. C. P. Klaasse, K. H. J. Buschow, *J. Magn. Magn. Mater.* **2007**, *310*, E1012.
[134] D. T. C. Thanh, E. Brück, N. T. Trung, J. C. P. Klaasse, K. H. J. Buschow, Z. Q. Ou, O. Tegus, L. Caron, *J. Appl. Phys.* **2008**, *103*, 07B318.
[135] N. T. Trung, Z. Q. Ou, T. J. Gortenmulder, O. Tegus, K. H. J. Buschow, E. Brück, *Appl. Phys. Lett.* **2009**, *94*, 102513.
[136] F. Guillou, G. Porcari, H. Yibole, N. van Dijk, E. Bruck, *Adv. Mater.* **2014**, *26*, 2671.
[137] H. Yibole, F. Guillou, L. Zhang, N. H. van Dijk, E. Brück, *J. Phys. D Appl. Phys.* **2014**, *47*, 075002.
[138] M. J. Neish, M. P. Oxley, J. Guo, B. C. Sales, L. J. Allen, M. F. Chisholm, *Phys. Rev. Lett.* **2015**, *114*, 106101.
[139] X. F. Miao, L. Caron, P. Roy, N. H. Dung, L. Zhang, W. A. Kockelmann, R. A. de Groot, N. H. van Dijk, E. Brück, *Phys. Rev. B* **2014**, *89*, 174429.
[140] N. H. Dung, Z. Q. Ou, L. Caron, L. Zhang, D. T. C. Thanh, G. A. de Wijs, R. A. de Groot, K. H. J. Buschow, E. Brück, *Adv. Energy Mater.* **2011**, *1*, 1215.
[141] N. H. Dung, L. Zhang, Z. Q. Ou, L. Zhao, L. van Eijck, A. M. Mulders, M. Avdeev, E. Suard, N. H. van Dijk, E. Brück, *Phys. Rev. B* **2012**, *86*, 045134.
[142] H. Yibole, F. Guillou, L. Caron, E. Jimenez, F. M. F. de Groot, P. Roy, R. de Groot, N. H. van Dijk, E. Brück, *Phys. Rev. B* **2015**, *91*, 014429.
[143] M. F. J. Boeije, P. Roy, F. Guillou, H. Yibole, X. F. Miao, L. Caron, D. Banerjee, N. H. van Dijk, R. A. de Groot, E. Brück, *Chem. Mater.* **2016**, *28*, 4901.
[144] P. Roy, E. Torun, R. A. de Groot, *Phys. Rev. B* **2016**, *93*, 094110.
[145] H. Yibole, F. Guillou, Y. K. Huang, G. R. Blake, A. J. E. Lefering, N. H. van Dijk, E. Brück, *Appl. Phys. Lett.* **2015**, *107*, 162403.
[146] B. C. Sales, M. A. Susner, B. S. Conner, J. Q. Yan, A. F. May, *Phys. Rev. B* **2015**, *92*, 104429.
[147] L. L. Bao, W. Meijuan, H. Yibole, Z. Q. Ou, F. Guillou, *J. Alloy Compd.* **2024**, *970*, 172612.
[148] X. F. Miao, L. Caron, J. Cedervall, P. C. M. Gubbens, P. D. de Réotier, A. Yaouanc, F. Qian, A. R. Wildes, H. Luetkens, A. Amato, N. H. van Dijk, E. Brück, *Phys. Rev. B* **2016**, *94*, 014426.
[149] X. F. Miao, Y. Mitsui, A. I. Dugulan, L. Caron, N. V. Thang, P. Manuel, K. Koyama, K. Takahashi, N. H. van Dijk, E. Brück, *Phys. Rev. B* **2016**, *94*, 094426.
[150] X. M. You, M. Maschek, N. H. H. van Dijk, E. Bruck, *Entropy-Switz* **2022**, *24*, 2.
[151] I. Batashev, G. A. de Wijs, N. H. van Dijk, E. Brück, *J. Magn. Magn. Mater.* **2021**, *537*, 168179.
[152] X. F. Miao, N. V. Thang, L. Caron, H. Yibole, R. I. Smith, N. H. van Dijk, E. Brück, *Scripta Mater.* **2016**, *124*, 129.

© 2024 Wiley-VCH GmbH

16146840, 0, Downloaded from https://onlinelibrary.wiley.com/doi/10.1002/aenm.202400369 by Tu Delft, Wiley Online Library on [08/04/2024]. See the Terms and Conditions (https://onlinelibrary.wiley.com/terms-and-conditions) on Wiley Online Library for rules of use; OA articles are governed by the applicable Creative Commons License

[153] F. Q. Zhang, I. Batashev, Q. Shen, Z. Y. Wu, R. I. Smith, G. A. de Wijs, N. van Dijk, E. Brück, *Acta Mater.* **2022**, *234*, 118057.
[154] J. W. Lai, B. W. Huang, X. F. Miao, N. V. Thang, X. M. You, M. Maschek, L. van Eijck, D. C. Zeng, N. van Dijk, E. Bruck, *J. Alloy Compd.* **2019**, *803*, 671.
[155] Z. Q. Ou, N. H. Dung, L. Zhang, L. Caron, E. Torun, N. H. van Dijk, O. Tegus, E. Brück, *J. Alloy Compd.* **2018**, *730*, 392.
[156] X. F. Miao, Patent 0925–8388 **2019**.
[157] J. T. Feng, F. J. Qian, D. N. Shi, H. Yang, *Appl. Phys.* **2019**, *9*, 358.
[158] S. Y. Hu, X. F. Miao, J. Liu, Z. Q. Ou, M. Q. Cong, O. Haschuluu, Y. Y. Gong, F. J. Qian, Y. R. You, Y. J. Zhang, F. Xu, E. Brück, *Intermetallics* **2019**, *114*, 106602.
[159] X. F. Miao, Y. Gong, F. Q. Zhang, Y. R. You, L. Caron, F. J. Qian, W. H. Guo, Y. J. Zhang, Y. Y. Gong, F. Xu, N. van Dijk, E. Brück, *J. Mater. Sci. Technol.* **2022**, *103*, 165.
[160] H. Wada, K. Nakamura, K. Katagiri, T. Ohnishi, K. Yamashita, A. Matsushita, *Jpn. J. Appl. Phys.* **2014**, *53*, 063001.
[161] D. M. Liu, H. Zhang, S. B. Wang, W. Q. Xiao, Z. L. Zhang, N. Tian, C. X. Liu, M. Yue, Q. Z. Huang, J. X. Zhang, J. W. Lynn, *J. Alloy Compd.* **2015**, *633*, 120.
[162] S. Kim, H. Shin, I. Chu, K. Lee, K. H. Lee, W. Lee, *J. Alloy Compd.* **2022**, *890*, 161798.
[163] P. Wlodarczyk, L. Hawelek, M. Kowalczyk, M. Kaminska, P. Zackiewicz, M. Polak, M. Hreczka, A. Kolano-Burian, *Solid State Sci.* **2016**, *56*, 23.
[164] F. Q. Zhang, S. Smits, A. Kiecana, I. Batashev, Q. Shen, N. van Dijk, E. Brück, *J. Alloy Compd.* **2023**, *933*, 167802.
[165] F. Q. Zhang, I. Batashev, N. van Dijk, E. Brück, *Scripta Mater.* **2023**, *226*, 115253.
[166] J. W. Lai, X. M. You, I. Dugulan, B. W. Huang, J. Liu, M. Maschek, L. van Eijck, N. Dijk, E. Brück, *J. Alloy Compd.* **2020**, *821*, 153451.
[167] X. F. Miao, W. Y. Wang, H. X. Liang, F. J. Qian, M. Q. Cong, Y. J. Zhang, A. Muhammad, Z. J. Tian, F. Xu, *J. Mater. Sci.* **2020**, *55*, 6660.
[168] J. W. Lai, A. Bolyachkin, N. Terada, S. Dieb, X. Tang, T. Ohkubo, H. Sepehri-Amin, K. Hono, *Acta Mater.* **2022**, *232*, 117942.
[169] D. F. Tu, J. Q. Yan, Y. B. Xie, J. Li, S. Feng, M. X. Xia, J. G. Li, P. L. Alex, *J. Mater. Sci. Technol.* **2022**, *96*, 241.
[170] X. F. Miao, C. X. Wang, T. W. Liao, S. H. Ju, J. J. Zha, W. Y. Wang, J. Liu, Y. J. Zhang, Q. Y. Ren, F. Xu, L. Caron, *Acta Mater.* **2023**, *242*, 118453.
[171] D. E. Schipper, Z. H. Zhao, H. Thirumalai, A. P. Leitner, S. L. Donaldson, A. Kumar, F. Qin, Z. M. Wang, L. C. Grabow, J. M. Bao, K. H. Whitmire, *Chem. Mater.* **2018**, *30*, 3588.
[172] Y. Zhang, H. J. Zhang, Y. Y. Feng, L. Liu, Y. Wang, *ACS Appl. Mater. Interfaces* **2015**, *7*, 26684.
[173] X. F. Miao, S. Y. Hu, F. Xu, E. Brück, *Rare Met.* **2018**, *37*, 723.
[174] F. Q. Zhang, Ph.D. thesis, Delft University of Technology, **2022**.
[175] Y. Y. Shao, B. F. Lu, M. X. Zhang, J. Liu, *Acta Mater.* **2018**, *150*, 206.
[176] M. E. Gruner, W. Keune, B. Roldan Cuenya, C. Weis, J. Landers, S. I. Makarov, D. Klar, M. Y. Hu, E. E. Alp, J. Zhao, M. Krautz, O. Gutfleisch, H. Wende, *Phys. Rev. Lett.* **2015**, *114*, 057202.
[177] A. Fujita, *Acta Mater.* **2019**, *169*, 162.
[178] K. P. Skokov, A. Y. Karpenkov, D. Y. Karpenkov, I. A. Radulov, D. Günzing, B. Eggert, A. Rogalev, F. Wilhelm, J. Liu, Y. Shao, K. Ollefs, M. E. Gruner, H. Wende, O. Gutfleisch, *Appl. Phys. Rev.* **2023**, *10*, 031408.
[179] V. Hardy, R. Hamane, F. Veillon, M. Risser, F. Guillou, *Acta Mater.* **2022**, *231*, 117869.
[180] H. Zhang, Y. J. Sun, E. Niu, F. X. Hu, J. R. Sun, B. G. Shen, *Appl. Phys. Lett.* **2014**, *104*, 062407.
[181] M. X. Zhang, Y. Ouyang, Y. F. Zhang, J. Liu, *J. Alloy Compd.* **2020**, *823*, 153846.
[182] Y. Y. Shao, Y. F. Liu, K. Wang, M. X. Zhang, J. Liu, *Acta Mater.* **2020**, *195*, 163.
[183] L. Y. Miao, X. Lu, Z. Y. Wei, Y. F. Zhang, Y. X. Zhang, J. Liu, *Acta Mater.* **2023**, *245*, 118635.
[184] J. Lyubina, U. Hannemann, L. F. Cohen, M. P. Ryan, *Adv. Energy Mater.* **2012**, *2*, 1323.
[185] J. Liu, M. X. Zhang, Y. Y. Shao, A. R. Yan, *Ieee T Magn.* **2015**, *51*, 2501502.
[186] I. A. Radulov, D. Y. Karpenkov, K. P. Skokov, A. Y. Karpenkov, T. Braun, V. Brabänder, T. Gottschall, M. Pabst, B. Stoll, O. Gutfleisch, *Acta Mater.* **2017**, *127*, 389.
[187] Y. X. Wang, H. Zhang, E. K. Liu, X. C. Zhong, K. Tao, M. L. Wu, C. F. Xing, Y. N. Xiao, J. Liu, Y. Long, *Adv. Electron. Mater.* **2018**, *4*, 1700636.
[188] H. Zhang, J. Liu, M. X. Zhang, Y. Y. Shao, Y. Li, A. Yan, *Scripta Mater.* **2016**, *120*, 58.
[189] C. X. Lu, Q. M. Wu, H. F. Wang, X. J. Wang, L. W. Li, *J. Alloy Compd.* **2021**, *872*, 159553.
[190] A. Funk, J. Freudenberger, A. Waske, M. Krautz, *Mater. Today Energy* **2018**, *9*, 223.
[191] M. Krautz, L. Beyer, A. Funk, A. Waske, B. Weise, J. Freudenberger, T. Gottschall, *Mater. Design* **2020**, *193*, 108832.
[192] A. Fujita, S. Fujieda, K. Fukamichi, Y. Yamazaki, Y. Iijima, *Mater. Trans.* **2002**, *43*, 1202.
[193] S. H. Xie, J. Q. Li, Y. H. Zhuang, *J. Magn. Magn. Mater.* **2007**, *311*, 589.
[194] Y. F. Chen, F. Wang, B. G. Shen, G. J. Wang, J. R. Sun, *J. Appl. Phys.* **2003**, *93*, 1323.
[195] M. Balli, M. Rosca, D. Fruchart, D. Gignoux, *J. Magn. Magn. Mater.* **2009**, *321*, 123.
[196] L. M. Moreno-Ramírez, C. Romero-Muñiz, J. Y. Law, V. Franco, A. Conde, I. A. Radulov, F. Maccari, K. P. Skokov, O. Gutfleisch, *Acta Mater.* **2019**, *175*, 406.
[197] J. W. Lai, H. Sepehri-Amin, X. Tang, J. Li, Y. Matsushita, T. Ohkubo, A. T. Saito, K. Hono, *Acta Mater.* **2021**, *220*, 117286.
[198] J. Z. Hao, F. X. Hu, J. T. Wang, F. R. Shen, Z. B. Yu, H. B. Zhou, H. Wu, Q. Z. Huang, K. M. Qiao, J. Wang, J. He, L. H. He, J. R. Sun, B. G. Shen, *Chem. Mater.* **2020**, *32*, 1807.
[199] L. M. Moreno-Ramírez, C. Romero-Muñiz, J. Y. Law, V. Franco, A. Conde, I. A. Radulov, F. Maccari, K. P. Skokov, O. Gutfleisch, *Acta Mater.* **2018**, *160*, 137.
[200] Y. F. Liu, X. Q. Fu, Q. Yu, M. X. Zhang, J. Liu, *Acta Mater.* **2021**, *207*, 116687.
[201] A. Davarpanah, I. Radulov, N. Shayanfar, F. Maccari, K. Skokov, J. Amaral, O. Gutfleisch, *J. Phys. D Appl. Phys.* **2021**, *54*, 225001.
[202] Y. J. Yan, C. S. Liu, W. C. Lu, Y. Sun, W. T. Zhu, X. L. Nie, X. H. Sang, W. Y. Zhao, Q. J. Zhang, *J. Alloy Compd.* **2022**, *910*, 164858.
[203] V. Paul-Boncour, L. Bessais, *Magnetochemistry* **2021**, *7*, 13.
[204] Y. Y. Shao, X. F. Miao, Y. J. Zhang, F. Xu, J. Liu, *J. Magn. Magn. Mater.* **2022**, *564*, 170057.
[205] B. Pulko, J. Tusek, J. D. Moore, B. Weise, K. Skokov, O. Mityashkin, A. Kitanovski, C. Favero, P. Fajfar, O. Gutfleisch, A. Waske, A. Foredos, *J. Magn. Magn. Mater.* **2015**, *375*, 65.
[206] S. Tavares, K. S. Yang, M. A. Meyers, *Prog. Mater. Sci.* **2023**, *132*, 101017.
[207] F. Heusler, *Verh. DPG* **1903**, *5*, 219.
[208] F. Heusler, W. Starck, E. Haupt, *Verh. Dtsch. Phys. Ges* **1903**, *5*, 219.
[209] I. K. Zasimchuk, V. V. Kokorin, V. V. Martynov, A. V. Tkachenko, V. A. Chernenko, *Phys. Metals Metallogr.* **1990**, *69*, 104.
[210] K. Ullakko, J. K. Huang, C. Kantner, R. C. OHandley, V. V. Kokorin, *Appl. Phys. Lett.* **1996**, *69*, 1966.
[211] F. X. Hu, B. G. Shen, J. R. Sun, *Appl. Phys. Lett.* **2000**, *76*, 3460.
[212] F. X. Hu, B. G. Shen, J. R. Sun, G. H. Wu, *Phys. Rev. B* **2001**, *64*, 132412.
[213] Y. Sutou, Y. Imano, N. Koeda, T. Omori, R. Kainuma, K. Ishida, K. Oikawa, *Appl. Phys. Lett.* **2004**, *85*, 4358.

© 2024 Wiley-VCH GmbH

16146840, 0, Downloaded from https://onlinelibrary.wiley.com/doi/10.1002/aenm.202400369 by Tu Delft, Wiley Online Library on [08/04/2024]. See the Terms and Conditions (https://onlinelibrary.wiley.com/terms-and-conditions) on Wiley Online Library for rules of use; OA articles are governed by the applicable Creative Commons License

[214] R. Kainuma, Y. Imano, W. Ito, Y. Sutou, H. Morito, S. Okamoto, O. Kitakami, K. Oikawa, A. Fujita, T. Kanomata, K. Ishida, *Nature* **2006**, *439*, 957.
[215] Z. D. Han, D. H. Wang, C. L. Zhang, S. L. Tang, B. X. Gu, Y. W. Du, *Appl. Phys. Lett.* **2006**, *89*, 182507.
[216] T. Krenke, E. Duman, M. Acet, E. F. Wassermann, X. Moya, L. Mañosa, A. Planes, *Nat. Mater.* **2005**, *4*, 450.
[217] O. Heczko, H. Seiner, S. Fähler, *MRS Bull.* **2022**, *47*, 618.
[218] C. Felser, A. Hirohata, *Heusler Alloys*, Springer, Berlin **2015**.
[219] X. Z. Liang, X. J. Jiang, J. L. Gu, J. Bai, Z. Q. Guan, Z. Z. Li, H. L. Yan, Y. D. Zhang, C. Esling, X. Zhao, L. Zuo, *Scripta Mater.* **2021**, *204*, 114140.
[220] C. Felser, L. Wollmann, S. Chadov, G. H. Fecher, S. S. P. Parkin, *APL Mater.* **2015**, *3*, 041518.
[221] C. Felser, A. Hirohata, *Heusler Alloys Properties, Growth, Applications*, Springer, Berlin **2016**.
[222] N. A. Río-López, P. Lázpita, D. Salazar, V. I. Petrenko, F. Plazaola, V. Chernenko, J. M. Porro, *Metals-Basel* **2021**, *11*, 829.
[223] V. G. de Paula, M. S. Reis, *Chem. Mater.* **2021**, *33*, 5483.
[224] T. Bachagha, J. J. Sunol, *Metals-Basel* **2023**, *13*, 111.
[225] K. Alvarez, H. Y. Kim, S. Miyazaki, *J. Mater. Sci. Technol.* **2009**, *25*, 649.
[226] E. S. Belosludtseva, N. N. Kuranova, N. I. Kourov, V. G. Pushin, A. N. Uksusnikov, *Tech. Phys.* **2015**, *60*, 1330.
[227] T. Graf, C. Felser, S. S. P. Parkin, *Prog. Solid State Ch.* **2011**, *39*, 1.
[228] Z. N. Ni, X. M. Guo, X. T. Liu, Y. Y. Jiao, F. B. Meng, H. Z. Luo, *J. Alloy Compd.* **2019**, *775*, 427.
[229] Z. Q. Guan, J. Bai, J. L. Gu, X. Z. Liang, D. Liu, X. J. Jiang, R. K. Huang, Y. D. Zhang, L. D. Esling, X. Zhao, L. Zuo, *J. Mater. Sci. Technol.* **2021**, *68*, 103.
[230] C. C. Ma, K. Liu, X. Q. Han, S. Yang, N. Ye, J. C. Tang, *J. Magn. Magn. Mater.* **2020**, *493*, 165733.
[231] H. N. Bez, A. K. Pathak, A. Biswas, N. Zarkevich, V. Balema, Y. Mudryk, D. D. Johnson, V. K. Pecharsky, *Acta Mater.* **2019**, *173*, 225.
[232] K. Liu, X. Q. Han, K. Yu, C. C. Ma, Z. S. Zhang, Y. Song, S. C. Ma, H. Zeng, C. C. Chen, X. H. Luo, S. U. Rehman, Z. C. Zhong, *Intermetallics* **2019**, *110*, 106472.
[233] K. Liu, S. C. Ma, C. C. Ma, X. Q. Han, K. Yu, S. Yang, Z. S. Zhang, Y. Song, X. H. Luo, C. C. Chen, S. U. Rehman, Z. C. Zhong, *J. Alloy Compd.* **2019**, *790*, 78.
[234] Z. Q. Guan, J. Bai, S. D. Sun, J. L. Gu, X. Z. Liang, Y. D. Zhang, C. Esling, X. Zhao, L. Zuo, *Appl. Mater. Today* **2022**, *29*, 101634.
[235] Y. Li, L. Qin, H. G. Zhang, L. W. Li, *Chinese Phys. B* **2022**, *31*, 087103.
[236] F. Q. Zhang, Z. Y. Wu, J. L. Wang, W. Y. Chen, Z. D. Wu, x. Chi, C. L. Zhao, S. Eijt, H. Schut, X. D. Bai, Y. Ren, N. van Dijk, E. Brück, *Acta Mater.* **2024**, *234*, 118057.
[237] I. Unzueta, V. Sánchez-Alarcos, V. Recarte, J. I. Pérez-Landazábal, N. Zabala, J. A. García, F. Plazaola, *Phys. Rev. B* **2019**, *99*, 064108.
[238] I. Unzueta, D. A. de R-Lorente, E. Cesari, V. Sánchez-Alarcos, V. Recarte, J. I. Pérez-Landazábal, J. A. García, F. Plazaola, *Phys. Rev. Lett.* **2019**, *122*, 165701.
[239] Y. X. Zhang, H. Zeng, G. Yu, K. Liu, S. C. Ma, K. Yang, X. W. Zhao, G. Yuan, X. H. Luo, C. C. Chen, Z. C. Zhong, *Intermetallics* **2020**, *125*, 106882.
[240] A. Taubel, B. Beckmann, L. Pfeuffer, N. Fortunato, F. Scheibel, S. Ener, T. Gottschall, K. P. Skokov, H. B. Zhang, O. Gutfleisch, *Acta Mater.* **2020**, *201*, 425.
[241] D. Koch, B. Beckmann, N. M. Fortunato, O. N. Miroshkina, M. E. Gruner, H. B. Zhang, O. Gutfleisch, W. Donner, *J. Appl. Phys.* **2022**, *131*, 073903.
[242] F. Q. Zhang, I. Batashev, N. van Dijk, E. Brück, *Phys. Rev. Appl.* **2022**, *17*, 054032
[243] Z. Q. Guan, J. Bai, Y. Zhang, J. L. Gu, N. Morley, Y. D. Zhang, C. Esling, X. Zhao, L. Zuo, *Mater. Today Phys.* **2023**, *36*, 101183.
[244] Y. Li, X. Y. Ye, L. J. Lou, L. F. Wang, L. Qin, *J. Supercond. Nov. Magn.* **2023**, *36*, 631.
[245] A. N. Khan, L. M. Moreno-Ramírez, A. Díaz-García, J. Y. Law, V. Franco, *J. Alloy Compd.* **2023**, *931*, 167559.
[246] Q. Q. Zeng, J. L. Shen, H. N. Zhang, J. Chen, B. Ding, X. K. Xi, E. K. Liu, W. H. Wang, G. H. Wu, *J. Phys.-Condens. Mat.* **2019**, *31*, 425401.
[247] S. L. Liu, H. C. Xuan, T. Cao, L. B. Wang, Z. G. Xie, X. H. Liang, H. Li, L. Feng, F. H. Chen, P. D. Han, *Phys. Status Solidi A* **2019**, *216*, 1900563.
[248] Y. Li, S. Y. Huang, W. H. Wang, E. K. Liu, L. W. Li, *J. Appl. Phys.* **2020**, *127*, 233907.
[249] Y. Li, L. Qin, S. Y. Huang, L. W. Li, *Sci. China Mater.* **2022**, *65*, 486.
[250] S. Samanta, S. Ghosh, S. Chatterjee, K. Mandal, *J. Alloy Compd.* **2022**, *910*, 164929.
[251] F. Q. Zhang, K. Westra, Q. Shen, I. Batashev, A. Kiecana, E. Bruck, N. van Dijk, E. Brück, *J. Alloy Compd.* **2022**, *906*, 164337.
[252] S. Samanta, S. Chatterjee, J. Sinha, K. Mandal, *Phys. Rev. Mater.* **2023**, *7*, 084406.
[253] S. Y. Huang, L. Qin, Y. Li, L. W. Li, *Mater. Lett.* **2021**, *302*, 130376.
[254] F. Xu, C. Zhu, J. Wang, F. Luo, X. Q. Zhu, J. H. Xu, S. Q. Chen, J. F. Wang, G. L. Ma, F. H. Chen, Y. F. Kuang, J. He, Z. G. Sun, *J. Alloy Compd.* **2023**, *960*, 170768.
[255] D. Y. Cong, W. X. Xiong, A. Planes, Y. Ren, L. Mañosa, P. Y. Cao, Z. H. Nie, X. M. Sun, Z. Yang, X. F. Hong, Y. D. Wang, *Phys. Rev. Lett.* **2019**, *122*, 255703.
[256] A. Aznar, A. Gràcia-Condal, A. Planes, P. Lloveras, M. Barrio, J. L. Tamarit, W. X. Xiong, D. Y. Cong, C. Popescu, L. Mañosa, *Phys. Rev. Mater.* **2019**, *3*, 044406.
[257] Z. Q. Guan, J. Bai, Y. Zhang, S. D. Sun, J. L. Gu, X. Z. Liang, Y. D. Zhang, C. Esling, X. Zhao, L. Zuo, *J. Alloy Compd.* **2023**, *930*, 167477.
[258] Z. Q. Guan, J. Bai, Y. Zhang, J. L. Gu, Y. D. Zhang, C. Esling, X. Zhao, L. Zuo, *Scripta Mater.* **2023**, *229*, 115353.
[259] Z. Q. Guan, J. Bai, Y. Zhang, J. L. Gu, X. Z. Liang, Y. D. Zhang, L. D. Esling, X. Zhao, L. Zuo, *J. Appl. Phys.* **2022**, *131*, 165107.
[260] B. Beckmann, D. Koch, L. Pfeuffer, T. Gottschall, A. Taubel, E. Adabifiroozjaei, O. N. Miroshkina, S. Riegg, T. Niehoff, N. A. Kani, M. E. Gruner, L. Molina-Luna, K. P. Skokov, O. Gutfleisch, *Acta Mater.* **2023**, *246*, 118695.
[261] S. H. Li, D. Y. Cong, W. X. Xiong, Z. Chen, X. Zhang, Z. H. Nie, S. W. Li, R. G. Li, Y. K. Wang, Y. X. Cao, Y. Ren, Y. D. Wang, *ACS Appl. Mater. Interfaces* **2021**, *13*, 31870.
[262] T. Jin, Y. Jung, *Top. Catal.* **2022**, *65*, 208.
[263] S. Samanta, S. Ghosh, K. Mandal, *J. Phys.-Condens. Mat.* **2022**, *34*, 105801.
[264] M. F. Tanzim, N. Fortunato, I. Samathrakis, R. W. Xie, I. Opahle, O. Gutfleisch, H. B. Zhang, *Adv. Funct. Mater.* **2023**, *33*, 2214967.
[265] M. Marathe, H. C. Herper, *Phys. Rev. B* **2023**, *107*, 174402.
[266] K. Yu, K. Liu, S. C. Ma, X. Q. Han, Z. S. Zhang, Y. Song, Y. X. Zhang, C. C. Chen, X. H. Luo, Z. C. Zhong, *J. Magn. Magn. Mater.* **2019**, *484*, 31.
[267] Y. C. Ling, Y. Hu, X. D. Chi, J. W. Chen, H. B. Wang, B. Niu, D. Wu, M. X. Xu, Z. D. Han, J. Du, Q. Y. Xu, *J. Appl. Phys.* **2022**, *131*, 173902.
[268] L. Peng, Q. Q. Zhang, N. Wang, Z. H. Xia, Y. J. Zhang, Z. G. Wu, E. K. Liu, Z. H. Liu, *Chinese Phys. B* **2023**, *32*, 017102.
[269] J. Dong, Z. H. Liu, X. D. Si, T. Zhou, J. Lin, Y. S. Liu, *Solid State Commun.* **2023**, *362*, 115099.
[270] J. G. Tan, Z. H. Liu, Y. J. Zhang, G. T. Li, H. G. Zhang, G. D. Liu, X. Q. Ma, *Results Phys.* **2019**, *12*, 1182.
[271] G. A. Jacob, R. J. Joseyphus, *Phys. Status Solidi A* **2021**, *218*, 2100050.
[272] Q. Q. Zeng, Z. W. Du, X. L. Han, B. B. Wang, G. H. Wu, E. K. Liu, *Acta Mater.* **2024**, *262*, 119429.
[273] S. Sanvito, C. Oses, J. K. Xue, A. Tiwari, M. Zic, T. Archer, P. Tozman, M. Venkatesan, M. Coey, S. Curtarolo, *Sci. Adv.* **2017**, *3*, e1602241.

© 2024 Wiley-VCH GmbH

16146840, 0, Downloaded from https://onlinelibrary.wiley.com/doi/10.1002/aenm.202400369 by Tu Delft, Wiley Online Library on [08/04/2024]. See the Terms and Conditions (https://onlinelibrary.wiley.com/terms-and-conditions) on Wiley Online Library for rules of use; OA articles are governed by the applicable Creative Commons License

[274] Y. L. Han, M. X. Wu, Y. Feng, Z. X. Cheng, T. T. Lin, T. Yang, R. Khenata, X. T. Wang, *IUCrJ* **2019**, *6*, 465.
[275] G. J. Li, L. Xu, Z. W. Ding, Z. H. Cao, *Appl. Phys. Lett.* **2023**, *123*, 022401.
[276] G. J. Li, E. K. Liu, W. H. Wang, G. H. Wu, *Phys. Rev. B* **2023**, *107*, 134440.
[277] D. B. Miracle, O. N. Senkov, *Acta Mater.* **2017**, *122*, 448.
[278] J. Y. Law, V. Franco, *APL Mater.* **2021**, *9*, 080702.
[279] M. S. Lucas, D. Belyea, C. Bauer, N. Bryant, E. Michel, Z. Turgut, S. O. Leontsev, J. Horwath, S. L. Semiatin, M. E. McHenry, C. W. Miller, *J. Appl. Phys.* **2013**, *113*, 17A923.
[280] A. Perrin, M. Sorescu, M. T. Burton, D. E. Laughlin, M. Mchenry, *Jom-Us* **2017**, *69*, 2125.
[281] A. Perrin, M. Sorescu, V. Ravi, D. E. Laughlin, M. E. McHenry, *AIP Adv.* **2019**, *9*, 035329.
[282] D. D. Belyea, M. S. Lucas, E. Michel, J. Horwath, C. W. Miller, *Sci. Rep.-Uk* **2015**, *5*, 15755.
[283] K. N. Wu, C. Liu, Q. Li, J. T. Huo, M. C. Li, C. T. Chang, Y. F. Sun, *J. Magn. Magn. Mater.* **2019**, *489*, 165404.
[284] S. Vorobiov, O. Pylypenko, Y. Bereznyak, I. Pazukha, E. Cizmar, M. Orendác, V. Komanicky, *Appl. Phys. a-Mater.* **2021**, *127*, 179.
[285] J. T. Huo, L. S. Huo, H. Men, X. M. Wang, A. Inoue, J. Q. Wang, C. T. Chang, R. W. Li, *Intermetallics* **2015**, *58*, 31.
[286] J. T. Huo, L. S. Huo, J. W. Li, H. Men, X. M. Wang, A. Inoue, C. T. Chang, J. Q. Wang, R. W. Li, *J. Appl. Phys.* **2015**, *117*, 073902.
[287] W. Sheng, J. Q. Wang, G. Wang, J. T. Huo, X. M. Wang, R. W. Li, *Intermetallics* **2018**, *96*, 79.
[288] L. Luo, H. X. Shen, Y. Bao, H. Yin, S. D. Jiang, Y. J. Huang, S. Guo, S. Y. Gao, D. W. Xing, Z. Li, J. F. Sun, *J. Magn. Magn. Mater.* **2020**, *507*, 166856.
[289] Y. K. Zhang, B. B. Wu, D. Guo, J. Wang, Z. M. Ren, *Chinese Phys. B* **2021**, *30*, 017501.
[290] L. W. Li, C. Xu, Y. Yuan, S. Q. Zhou, *Mater. Res. Lett.* **2018**, *6*, 413.
[291] Y. K. Zhang, J. Zhu, S. Li, J. Wang, Z. M. Ren, *J. Mater. Sci. Technol.* **2022**, *102*, 66.
[292] Z. Q. Dong, Z. J. Wang, S. H. Yin, *Intermetallics* **2020**, *124*, 106879.
[293] W. H. Zhu, L. Ma, M. F. He, Z. K. Li, H. Z. Zhang, Q. R. Yao, G. H. Rao, K. P. Su, X. C. Zhong, Z. W. Liu, X. Q. Gao, *Adv. Eng. Mater.* **2023**, *25*, 2201770.
[294] K. Sarlar, A. Tekgül, I. Kucuk, *Curr. Appl. Phys.* **2020**, *20*, 18.
[295] K. Sarlar, A. Tekgül, I. Kucuk, *Ieee Magn. Lett.* **2019**, *10*, 2109905.
[296] Y. K. Zhang, J. Zhu, Z. H. Hao, W. X. Hao, Z. J. Mo, L. W. Li, *Mater. Design* **2023**, *229*, 111894.
[297] Y. K. Zhang, P. Xu, J. Zhu, S. M. Yan, J. C. Zhang, L. W. Li, *Mater. Today Phys* **2023**, *32*, 101031.
[298] Y. Sun, W. J. Lv, Y. Liang, Y. Gao, W. J. Cui, Y. J. Yan, W. Y. Zhao, Q. J. Zhang, X. H. Sang, *Scripta Mater.* **2023**, *223*, 115068.
[299] H. B. C. Yin, J. Y. Law, Y. J. Huang, V. Franco, H. X. Shen, S. D. Jiang, Y. Bao, J. F. Sun, *Mater. Design* **2021**, *206*, 109824.
[300] H. B. C. Yin, J. Y. Law, Y. J. Huang, H. X. Shen, S. D. Jiang, S. Guo, V. Franco, J. F. Sun, *Sci. China Mater.* **2022**, *65*, 1134.
[301] H. Yin, J. Q. Wang, Y. J. Huang, H. X. Shen, S. Guo, H. B. Fan, J. T. Huo, J. F. Sun, *J. Mater. Sci. Technol.* **2023**, *149*, 167.
[302] L. L. Shao, L. Xue, Q. Luo, K. B. Yin, Z. R. Yuan, M. Y. Zhu, T. Liang, Q. S. Zeng, L. T. Sun, B. L. Shen, *J. Mater. Sci. Technol.* **2022**, *109*, 147.
[303] Y. N. Yin, F. F. Shi, G. Q. Liu, X. J. Tan, J. Jiang, A. Tiwari, B. H. Li, *Appl. Phys. Lett.* **2022**, *120*, 082404.
[304] J. Y. Law, L. M. Moreno-Ramírez, A. Díaz-García, A. Martín-Cid, S. Kobayashi, S. Kawaguchi, T. Nakamura, V. Franco, *J. Alloy Compd.* **2021**, *855*, 157424.
[305] J. Y. Law, A. Díaz-García, L. M. Moreno-Ramírez, V. Franco, *Acta Mater.* **2021**, *212*, 116931.
[306] Z. Zheng, X. Chen, H. Y. Wang, S. Da, G. Wang, Z. Qiu, D. Zeng, Q. Xia, *J. Alloy Compd.* **2023**, *966*, 171483.
[307] Y. Guo, T. T. Zhang, Z. S. Zhang, B. Chen, W. H. Guo, S. Pan, Y. Gong, Y. Q. Bai, Y. Y. Gong, J. Liu, X. F. Miao, F. Xu, *APL Mater.* **2022**, *10*, 091107.
[308] A. K. Cheetham, A. P. Wilkinson, *Angew. Chem. Int. Edit.* **1992**, *31*, 1557.
[309] S. Mobilio, F. Boscherini, C. Meneghini, *Synchrotron Radiation Basics, Methods and Applications*, Springer, Berlin **2015**.
[310] D. J. Duke, *Synchrotron Radiation: Production and Properties*, Oxford University Press, Oxford, UK **2000**.
[311] Y. Ren, X. B. Zuo, *Small Methods* **2018**, *2*, 1800064.
[312] A. Shabalin, PhD thesis, Universitat Hamburg, **2015**.
[313] R. Fosbinder, D. Orth, *Essentials of Radiologic Science*, McGraw-Hill, New York **2011**.
[314] P. S. Rahimabadi, M. Khodaei, K. R. Koswattage, *X-Ray Spectrom.* **2020**, *49*, 348.
[315] X. S. Liu, W. L. Yang, Z. Liu, *Adv. Mater.* **2014**, *26*, 7710.
[316] H. L. Yan, Y. D. Zhang, N. Xu, A. Senyshyn, H. G. Brokmeier, C. Esling, X. Zhao, L. Zuo, *Acta Mater.* **2015**, *88*, 375.
[317] S. Singh, P. Kushwaha, F. Scheibel, H. P. Liermann, S. R. Barman, M. Acet, C. Felser, D. Pandey, *Phys. Rev. B* **2015**, *92*, 020105(R).
[318] D. Huang, T. Y. Ma, D. E. Brown, S. H. Lapidus, Y. Ren, J. R. Gao, *Chem. Mater.* **2021**, *33*, 2837.
[319] M. Maschek, X. You, M. F. J. Boeije, D. Chernyshov, N. H. van Dijk, E. Brück, *Phys. Rev. B* **2018**, *98*, 224413.
[320] H. Y. Chen, Y. D. Wang, Z. H. Nie, R. G. Li, D. Y. Cong, W. J. Liu, F. Ye, Y. Z. Liu, P. Y. Cao, F. Y. Tian, X. Shen, R. H. Yu, L. Vitos, M. H. Zhang, S. L. Li, X. Y. Zhang, H. Zheng, J. F. Mitchell, Y. Ren, *Nat. Mater.* **2020**, *19*, 712.
[321] N. Biniskos, *PhD thesis, ILL* **2018**.
[322] J. Landers, S. Salamon, W. Keune, M. E. Gruner, M. Krautz, J. Zhao, M. Y. Hu, T. S. Toellner, E. E. Alp, O. Gutfleisch, H. Wende, *Phys. Rev. B* **2018**, *98*, 024417.
[323] A. Terwey, M. E. Gruner, W. Keune, J. Landers, S. Salamon, B. Eggert, K. Ollefs, V. Brabander, I. Radulov, K. Skokov, T. Faske, M. Y. Hu, J. Zhao, E. E. Alp, C. Giacobbe, O. Gutfleisch, H. Wende, *Phys. Rev. B* **2020**, *101*, 064415.
[324] D. Bessas, M. Maschek, H. Yibole, J. W. Lai, S. M. Souliou, I. Sergueev, A. I. Dugulan, N. H. van Dijk, E. Brück, *Phys. Rev. B* **2018**, *97*, 094303.
[325] M. Wolloch, M. E. Gruner, W. Keune, P. Mohn, J. Redinger, F. Hofer, D. Suess, R. Podloucky, J. Landers, S. Salamon, F. Scheibel, D. Spoddig, R. Witte, B. Roldan Cuenya, O. Gutfleisch, M. Y. Hu, J. Zhao, T. Toellner, E. E. Alp, M. Siewert, P. Entel, R. Pentcheva, H. Wende, *Phys. Rev. B* **2016**, *94*, 174435.
[326] O. N. Miroshkina, B. Eggert, J. Lill, B. Beckmann, D. Koch, M. Y. Hu, T. Lojewski, S. Rauls, F. Scheibel, A. Taubel, M. Sob, K. Ollefs, O. Gutfleisch, H. Wende, M. E. Gruner, M. Friák, *Phys. Rev. B* **2022**, *106*, 214302.
[327] S. H. Lohaus, M. Heine, P. Guzman, C. M. Bernal-Choban, C. N. Saunders, G. Shen, O. Hellman, D. Broido, B. Fultz, *Nat. Phys.* **2023**, *19*, 1642.
[328] S. J. L. Billinge, *Philos. T R Soc. A* **2019**, *377*, 20180413.
[329] J. A. Cooley, M. K. Horton, E. E. Levin, S. H. Lapidus, K. A. Persson, R. Seshadri, *Chem. Mater.* **2020**, *32*, 1243.
[330] J. A. Kurzman, A. J. Martinolich, J. R. Neilson, *Phys. Rev. B* **2015**, *92*, 184414.
[331] X. H. Zhang, Q. Yuan, T. L. Gao, Y. Ren, H. Wu, Q. Z. Huang, J. G. Zhao, X. J. Wang, Y. Yuan, C. Xu, Y. F. Hu, J. J. Dynes, J. G. Zhou, S. Q. Zhou, Y. Liu, B. Song, *J. Mater. Chem. C* **2018**, *6*, 13336.
[332] R. H. Kou, C. Geng, X. Su, *J. Magn. Magn. Mater.* **2022**, *562*, 169750.
[333] F. Benjamin, *APS March Meeting* **2022**.

© 2024 Wiley-VCH GmbH

16146840, 0, Downloaded from https://onlinelibrary.wiley.com/doi/10.1002/aenm.202400369 by Tu Delft, Wiley Online Library on [08/04/2024]. See the Terms and Conditions (https://onlinelibrary.wiley.com/terms-and-conditions) on Wiley Online Library for rules of use; OA articles are governed by the applicable Creative Commons License

[334] V. Petkov, T. D. Rao, A. M. Abeykoon, J. R. Galeano-Cabral, K. Y. Wei, *Phys. Rev. Mater.* **2022**, *6*, 104407.
[335] A. A. Hummer, A. Rompel, in *Advances in Protein Chemistry and Structural Biology*, Vol. *93*, Elsevier Academic Press, Cham, Switzerland **2013**, p. 257.
[336] C. Antoniak, *Beilstein J Nanotech* **2011**, *2*, 237.
[337] F. De Groot, *Chem. Rev.* **2001**, *101*, 1779.
[338] J. Van Bokhoven, C. Lamberti, *X-Ray Absorption and X-Ray Emission Spectroscopy Theory and Applications*, John Wiley & Sons, Hoboken, NJ **2015**.
[339] Y. C. Tseng, D. Haskel, J. C. Lang, S. Sinogeikin, Y. Mudryk, V. K. Pecharsky, K. A. Gschneidner, *Phys. Rev. B* **2007**, *76*, 014411.
[340] F. Guillou, K. Ollefs, F. Wilhelm, A. Rogalev, A. N. Yaresko, H. Yibole, N. H. van Dijk, E. Brück, *Phys. Rev. B* **2015**, *92*, 224427.
[341] H. Yibole, F. Guillou, L. Caron, E. Jiménez, F. M. F. de Groot, P. Roy, R. de Groot, N. H. van Dijk, E. Brück, *Phys. Rev. B* **2015**, *91*, 014429.
[342] K. H. Kim, W. J. Son, S. J. Kwon, I. G. Kim, D. S. Yang, Y. N. Ham, *Electron. Mater. Lett.* **2016**, *12*, 255.
[343] B. Wurentuya, H. Yibole, F. Guillou, Z. Q. Ou, Z. D. Zhang, O. Tegus, *Physica B* **2018**, *544*, 66.
[344] B. Eggert, J. Lill, D. Günzing, C. Pillich, A. Terwey, I. A. Radulov, F. Wilhelm, A. Rogalev, M. Rovezzi, K. Skokov, *arXiv* **2023**, arXiv:2304.03065.
[345] S. Roy, E. Blackburn, S. M. Valvidares, M. R. Fitzsimmons, S. C. Vogel, M. Khan, I. Dubenko, S. Stadler, N. Ali, S. K. Sinha, J. B. Kortright, *Phys. Rev. B* **2009**, *79*, 235127.
[346] V. N. Antonov, L. V. Bekenov, S. Uba, A. Bonda, L. Uba, *J. Alloy Compd.* **2017**, *695*, 1826.
[347] S. Sun, H. Qin, H. Wang, R. Ning, Y. Zhao, J. Zhu, Z. Gao, D. Cong, Y. Wang, W. Cai, *Mater. Today Energy* **2020**, *18*, 100533.
[348] R. Y. Umetsu, H. Yasumura, Y. Narumi, Y. Kotani, T. Nakamura, H. Nojiri, R. Kainuma, *J. Alloy Compd.* **2022**, *890*, 161590.
[349] D. J. Keavney, Y. Choi, M. V. Holt, V. Uhlír, D. Arena, E. E. Fullerton, P. J. Ryan, J. W. Kim, *Sci Rep-Uk* **2018**, *8*, 1778.
[350] Y. J. Zhang, J. H. Chen, K. Ikeda, K. Yamagami, Y. Wang, Y. Choi, A. Yasui, J. Ma, Y. H. Lin, C. W. Nan, H. Wadati, *J. Alloy Compd.* **2022**, *921*, 166080.
[351] K. R. Priolkar, E. T. Dias, G. Aquilanti, Ö. Çakir, M. Acet, A. K. Nigam, *J Phys Conf Ser* **2016**, *712*, 012117.
[352] F. Guillou, F. Wilhelm, O. Tegus, A. Rogalev, *Appl. Phys. Lett.* **2016**, *108*, 122405.
[353] F. Guillou, A. Hen, F. Wilhelm, A. Rogalev, *J. Phys.: Conf. Ser.* **2017**, *903*, 012043.
[354] F. Garcia, L. C. Sampaio, A. Y. Takeuchi, H. Tolentino, A. Fontaine, *J. Appl. Phys.* **2000**, *87*, 5881.
[355] X. Tang, H. Sepehri-Amin, N. Terada, A. Martin-Cid, I. Kurniawan, S. Kobayashi, Y. Kotani, H. Takeya, J. Lai, Y. Matsushita, T. Ohkubo, Y. Miura, T. Nakamura, K. Hono, *Nat. Commun.* **2022**, *13*, 1817.
[356] C. W. Chuang, H. J. Lin, F. M. F. de Groot, F. H. Chang, C. T. Chen, Y. Y. Chin, Y. F. Liao, K. D. Tsuei, J. A. Chelvane, R. Nirmala, A. Chainani, *Phys. Rev. B* **2020**, *101*, 115137.
[357] A. Aubert, G. Gomez, K. Skokov, F. Wilhelm, H. Wende, A. Rogalev, O. Gutfleisch, K. Ollefs, presented at 2023 IEEE International Magnetic Conference-Short Papers (INTERMAG Short Papers), Sendai, Japan, May **2023**.
[358] Y. Luo, S. C. Wu, Y. N. Hu, Y. N. Fu, *Front Mech Eng-Prc* **2018**, *13*, 461.
[359] C. T. Cao, M. F. Toney, S. K. Sham, R. Harder, P. R. Shearing, X. H. Xiao, J. J. Wang, *Mater. Today* **2020**, *34*, 132.
[360] F. C. Tang, Z. B. Wu, C. Yang, M. Osenberg, A. Hilger, K. Dong, H. Markötter, I. Manke, F. Sun, L. B. Chen, G. L. Cui, *Small Methods* **2021**, *5*, 2100557.
[361] A. Funk, M. Zeilinger, A. Miehe, D. Sopu, J. Eckert, F. Dötz, A. Waske, *Chem. Eng. Sci.* **2018**, *175*, 84.
[362] M. Krautz, A. Funk, K. P. Skokov, T. Gottschall, J. Eckert, O. Gutfleisch, A. Waske, *Scripta Mater.* **2015**, *95*, 50.
[363] B. Weise, K. Sellschopp, M. Bierdel, A. Funk, M. Bobeth, M. Krautz, A. Waske, *J. Appl. Phys.* **2016**, *120*, 125103.
[364] A. Waske, L. Giebeler, B. Weise, A. Funk, M. Hinterstein, M. Herklotz, K. Skokov, S. Fähler, O. Gutfleisch, J. Eckert, *Phys Status Solidi-R* **2015**, *9*, 136.
[365] A. Waske, E. Lovell, A. Funk, K. Sellschopp, A. Rack, L. Giebeler, P. F. Gostin, S. Fähler, L. F. Cohen, *APL Mater.* **2016**, *4*, 106101.
[366] V. Sharma, L. Balderson, R. Heo, O. Bishop, C. S. M. Hunt, E. E. Carpenter, R. L. Hadimani, H. Zhao, R. Barua, *J. Alloy Compd.* **2022**, *920*, 165891.
[367] K. D. N'dri, N. Charpentier, L. Hirsinger, A. Gilbin, T. Barriere, *Powder Technol.* **2023**, *425*, 118616.
[368] S. S. Zhang, N. van Dijk, S. van der Zwaag, *Acta Metall Sin-Engl* **2020**, *33*, 1167.
[369] N. van Dijk, S. van der Zwaag, *Adv. Mater. Interfaces* **2018**, *5*, 1800226.
[370] H. Fang, C. D. Versteylen, S. Zhang, Y. Yang, P. Cloetens, D. Ngan-Tillard, E. Brück, S. van der Zwaag, N. H. van Dijk, *Acta Mater.* **2016**, *121*, 352.
[371] H. Fang, N. Szymanski, C. D. Versteylen, P. Cloetens, C. Kwakernaak, W. G. Sloof, F. D. Tichelaar, S. Balachandran, M. Herbig, E. Brück, S. van der Zwaag, N. H. van Dijk, *Acta Mater.* **2019**, *166*, 531.
[372] Y. Fu, H. Fang, F. Monaco, P. Cloetens, F. D. Tichelaar, J. G. van Meel, E. Bruck, S. van der Zwaag, N. H. van Dijk, *Acta Mater.* **2022**, *239*, 118266.
[373] N. van Dijk, in *Encyclopedia of Materials: Metals and Alloys*, Elsevier, Cham, Switzerland **2022**, p. 682.
[374] S. C. Vogel, H. G. Priesmeyer, *Rev Mineral Geochem* **2006**, *63*, 27.
[375] R. J. Harrison, *Rev Mineral Geochem* **2006**, *63*, 113.
[376] S. M. Yusuf, A. Kumar, *Appl. Phys. Rev.* **2017**, *4*, 031303.
[377] N. Fomin, J. Fry, R. W. Pattie, G. L. Greene, *Annu Rev Nucl Part S* **2022**, *72*, 151.
[378] T. Chatterji, *Neutron Scattering from Magnetic Materials* **2006**.
[379] A. Furrer, J. Mesot, T. Strässle, *Neutron Scattering in Condensed Matter Physics*, World Scientific, Singapore **2009**.
[380] G. L. Squires, *Introduction to the Theory of Thermal Neutron Scattering*, Cambridge University Press, Cambridge, MA **2012**.
[381] J. Dawidowski, J. R. Granada, J. R. Santisteban, F. Cantargi, L. A. R. Palomino, in *Experimental Methods in the Physical Sciences*, Vol. *44*, Elsevier, Cham, Switzerland **2013**, p. 471.
[382] H. B. Zhou, Z. B. Yu, F. X. Hu, J. T. Wang, F. R. Shen, J. Z. Hao, L. H. He, Q. Z. Huang, Y. H. Gao, B. J. Wang, Z. Yin, Z. Y. Tian, J. Wang, Y. Z. Chen, J. R. Sun, T. Y. Zhao, B. G. Shen, *Acta Mater.* **2023**, *260*, 119312.
[383] X. Y. Hai, C. Mayer, C. V. Colin, S. Miraglia, *J. Magn. Magn. Mater.* **2016**, *400*, 344.
[384] E. Palacios, J. A. Rodríguez-Velamazán, M. Evangelisti, G. J. McIntyre, G. Lorusso, D. Visser, L. J. de Jongh, L. A. Boatner, *Phys. Rev. B* **2014**, *90*, 214423.
[385] P. Hering, K. Friese, J. Voigt, J. Persson, N. Aliouane, A. Grzechnik, A. Senyshyn, T. Brückel, *Chem. Mater.* **2015**, *27*, 7128.
[386] S. Gupta, K. G. Suresh, A. Das, A. K. Nigam, A. Hoser, *APL Mater.* **2015**, *3*, 066102.
[387] A. Kumar, S. M. Yusuf, C. Ritter, *Phys. Rev. B* **2017**, *96*, 014427.
[388] P. Mukherjee, S. E. Dutton, *Adv. Funct. Mater.* **2017**, *27*, 1701950.
[389] Q. Y. Ren, W. D. Hutchison, J. L. Wang, A. J. Studer, S. J. Campbell, *Chem. Mater.* **2018**, *30*, 1324.
[390] F. R. Shen, H. B. Zhou, F. X. Hu, J. T. Wang, S. H. Deng, B. T. Wang, H. Wu, Q. Z. Huang, J. Wang, J. Chen, L. H. He, J. Z. Hao, Z. B. Yu, F. X. Liang, T. J. Liang, J. R. Sun, B. G. Shen, *Mater. Horiz.* **2020**, *7*, 804.

© 2024 Wiley-VCH GmbH

16146840, 0, Downloaded from https://onlinelibrary.wiley.com/doi/10.1002/aenm.202400369 by Tu Delft, Wiley Online Library on [08/04/2024]. See the Terms and Conditions (https://onlinelibrary.wiley.com/terms-and-conditions) on Wiley Online Library for rules of use; OA articles are governed by the applicable Creative Commons License

[391] X. F. Miao, Y. Gong, L. Caron, Y. R. You, G. Z. Xu, D. Sheptyakov, P. Manuel, F. J. Qian, Y. J. Zhang, F. Xu, N. van Dijk, E. Brück, *Phys. Rev. Mater.* **2020**, *4*, 104407.
[392] J. A. Cooley, J. D. Bocarsly, E. C. Schueller, E. E. Levin, E. E. Rodriguez, A. Huq, S. H. Lapidus, S. D. Wilson, R. Seshadri, *Phys. Rev. Mater.* **2020**, *4*, 044405.
[393] N. Terada, K. Terashima, P. B. de Castro, C. V. Colin, H. Mamiya, T. D. Yamamoto, H. Takeya, O. Sakai, Y. Takano, H. Kitazawa, *Phys. Rev. B* **2020**, *102*, 094435.
[394] F. Gao, J. M. Sheng, W. J. Ren, Q. Zhang, X. H. Luo, J. Qi, M. R. Cong, B. Li, L. S. Wu, Z. D. Zhang, *Phys. Rev. B* **2022**, *106*, 134426.
[395] Y. Z. Song, M. Xu, X. Q. Zheng, C. Zhou, N. K. Shi, Q. Z. Huang, S. G. Wang, Y. Jiang, X. R. Xing, J. Chen, *J. Mater. Sci. Technol.* **2023**, *147*, 102.
[396] O. Scharpf, H. Capellmann, *Phys. Status Solidi A-Appl. Res.* **1993**, *135*, 359.
[397] N. Biniskos, K. Schmalzl, S. Raymond, S. Petit, P. Steffens, J. Persson, T. Brückel, *Phys. Rev. Lett.* **2018**, *120*, 257205.
[398] N. Biniskos, S. Raymond, K. Schmalzl, A. Schneidewind, J. Voigt, R. Georgii, P. Hering, J. Persson, K. Friese, T. Brückel, *Phys. Rev. B* **2017**, *96*, 104407.
[399] Songlin, Dagula, O. Tegus, E. Brück, J. C. P. Klaasse, F. R. de Boer, K. H. J. Buschow, *J. Alloy Compd.* **2002**, *334*, 249.
[400] Z. Zhang, H. B. Zhou, R. Mole, C. Y. Yu, Z. Zhang, X. G. Zhao, W. J. Ren, D. H. Yu, B. Li, F. X. Hu, B. G. Shen, Z. D. Zhang, *Phys. Rev. Mater.* **2021**, *5*, L071401.
[401] R. J. C. Dixey, A. Wildes, P. W. Doheny, G. B. G. Stenning, P. J. Saines, *APL Mater.* **2023**, *11*, 041126.
[402] J. Cedervall, M. S. Andersson, E. K. Delczeg-Czirjak, D. Iusan, M. Pereiro, P. Roy, T. Ericsson, L. Häggström, W. Lohstroh, H. Mutka, M. Sahlberg, P. Nordblad, P. P. Deen, *Phys. Rev. B* **2019**, *99*, 174437.
[403] P. J. Stonaha, M. E. Manley, N. M. Bruno, I. Karaman, R. Arroyave, N. Singh, D. L. Abernathy, S. Chi, *Phys. Rev. B* **2015**, *92*, 140406(R).
[404] B. Li, Z. D. Zhang, *Sci. Sin. Phys., Mech. Astronom.* **2021**, *51*, 067505.
[405] R. L. Garwin, G. Gidal, L. M. Lederman, M. Weinrich, *Phys. Rev.* **1957**, *108*, 1589.
[406] P. D. deReotier, A. Yaouanc, *J Phys-Condens Mat* **1997**, *9*, 9113.
[407] S. J. Blundell, *Contemp. Phys.* **1999**, *40*, 175.
[408] P. Bakule, E. Morenzoni, *Contemp. Phys.* **2004**, *45*, 203.
[409] L. Nuccio, L. Schulz, A. J. Drew, *J. Phys. D Appl. Phys.* **2014**, *47*, 473001.
[410] J-PARC MLF, Muon experiment, https://mlfinfo.jp/en/aboutmlf/muon.html (accessed: October 2023).
[411] O. Ofer, J. Sugiyama, J. H. Brewer, E. J. Ansaldo, M. Månsson, K. H. Chow, K. Kamazawa, Y. Doi, Y. Hinatsu, *Phys. Rev. B* **2011**, *84*, 054428.
[412] S. X. Huangfu, Z. Guguchia, D. Cheptiakov, X. F. Zhang, H. Luetkens, D. J. Gawryluk, T. Shang, F. O. von Rohr, A. Schilling, *Phys. Rev. B* **2020**, *102*, 054423.
[413] Z. Guguchia, R. Khasanov, H. Luetkens, *npj Quantum Mater.* **2023**, *8*, 41.
[414] S. X. Huangfu, Z. Guguchia, T. Shang, H. Lin, H. L. Liu, X. F. Zhang, H. Luetkens, A. Schilling, *Phys. Rev. B* **2023**, *108*, 014410
[415] K. M. Kojima, R. Kadono, M. Miyazaki, M. Hiraishi, I. Yamauchi, A. Koda, Y. Tsuchiya, H. S. Suzuki, H. Kitazawa, *Phys. Rev. Lett.* **2014**, *112*, 087203.
[416] P. Miao, X. H. Lin, A. Koda, S. Lee, Y. Ishikawa, S. Torii, M. Yonemura, T. Mochiku, H. Sagayama, S. Itoh, K. Ikeda, T. Otomo, Y. X. Wang, R. Kadono, T. Kamiyama, *Adv. Mater.* **2017**, *29*, 1605991.
[417] A. Midya, N. Khan, D. Bhoi, P. Mandal, *Appl. Phys. Lett.* **2012**, *101*, 132415.
[418] P. Bonfà, M. M. Isah, B. A. Frandsen, E. J. Gibson, E. Brück, I. J. Onuorah, R. De Renzi, G. Allodi, *Phys. Rev. Mater.* **2021**, *5*, 044411.
[419] F. A. Selim, *Mater. Charact.* **2021**, *174*, 110952.
[420] P. P. Chattopadhyay, P. M. G. Nambissan, S. K. Pabi, I. Manna, *Phys. Rev. B* **2001**, *63*, 054107.
[421] R. Wurschum, A. Seeger, *Philos Mag A* **1996**, *73*, 1489.
[422] R. W. Siegel, *Annu. Rev. Mater. Sci.* **1980**, *10*, 393.
[423] O. K. Mogensen, *Positron Annihilation in Chemistry*, Springer, Berlin **1995**.
[424] P. J. Schultz, K. G. Lynn, *Rev. Mod. Phys.* **1988**, *60*, 701.
[425] R. Krause-Rehberg, H. S. Leipner, *Positron Annihilation in Semiconductors: Defect Studies*, Springer, Berlin **1999**.
[426] C. Hugenschmidt, *Surf. Sci. Rep.* **2016**, *71*, 547.
[427] J. Cízek, *J. Mater. Sci. Technol.* **2018**, *34*, 577.
[428] K. E. H. M. Hanssen, P. E. Mijnarends, L. P. L. M. Rabou, K. H. J. Buschow, *Phys. Rev. B* **1990**, *42*, 1533.
[429] A. Seeger, M. Fähnle, *Int. J. Mater. Res.* **2022**, *93*, 1030.
[430] T. D. Haynes, R. J. Watts, J. Laverock, Z. Major, M. A. Alam, J. W. Taylor, J. A. Duffy, S. B. Dugdale, *New J. Phys.* **2012**, *14*, 035020.
[431] D. Merida, J. A. García, V. Sánchez-Alarcos, J. I. Pérez-Landazábal, V. Recarte, F. Plazaola, *Appl. Phys. Lett.* **2014**, *104*, 231905.
[432] D. Merida, J. A. García, V. Sánchez-Alarcos, J. I. Pérez-Landazábal, V. Recarte, F. Plazaola, *J. Alloy Compd.* **2015**, *639*, 180.
[433] Y. H. Wang, D. Salas, B. Medasani, P. Entel, I. Karaman, R. Arróyave, T. C. Duong, *Phys. Status Solidi B* **2018**, *255*, 1700523.
[434] W. Griggs, B. Eggert, M. O. Liedke, M. Butterling, A. Wagner, U. Kentsch, E. Hirschmann, M. Grimes, A. J. Caruana, C. Kinane, H. Wende, R. Bali, T. Thomson, *APL Mater.* **2020**, *8*, 121103.
[435] H. Y. Hu, Y. L. Su, C. F. Shi, G. S. Gong, J. Zhou, Y. Q. Wang, *J. Mater. Sci.-Mater. El* **2022**, *33*, 12113.
[436] M. S. Xu, H. Y. Dai, T. Li, K. Peng, J. Chen, Z. P. Chen, Y. C. Xue, X. Z. Cao, B. Y. Wang, *J Supercond Nov Magn* **2020**, *33*, 2881.
[437] A. Adam, L. Cser, Z. Kajcsos, G. Zimmer, *Phys. Status Solidi B* **1972**, *49*, K79.
[438] M. Reynaud, J. Serrano-Sevillano, M. Casas-Cabanas, *Chem. Mater.* **2023**, *35*, 3345.
[439] W. Q. Shi, Ph.D. thesis, Delft University of Technology **2018**.
[440] C. S. Mejía, T. Niehoff, M. Strassheim, E. Bykov, Y. Skourski, J. Wosnitza, T. Gottschall, *J Phys-Energy* **2023**, *5*, 034006.
[441] C. S. Mejía, M. G. Zavareh, A. K. Nayak, Y. Skourski, J. Wosnitza, C. Felser, M. Nicklas, *J. Appl. Phys.* **2015**, *117*, 17E710.
[442] M. G. Zavareh, C. S. Mejía, A. K. Nayak, Y. Skourski, J. Wosnitza, C. Felser, M. Nicklas, *Appl. Phys. Lett.* **2015**, *106*, 071904.
[443] Y. Skourski, M. D. Kuz'min, K. P. Skokov, A. V. Andreev, J. Wosnitza, *Phys. Rev. B* **2011**, *83*, 214420.
[444] S. Taskaev, V. Khovaylo, K. Skokov, W. Liu, E. Bykov, M. Ulyanov, D. Bataev, A. Basharova, M. Kononova, D. Plakhotskiy, M. Bogush, T. Gottschall, O. Gutfleisch, *J. Appl. Phys.* **2020**, *127*, 233906.
[445] E. Bykov, W. Liu, K. Skokov, F. Scheibel, O. Gutfleisch, S. Taskaev, V. Khovaylo, D. Plakhotskiy, C. S. Mejia, J. Wosnitza, T. Gottschall, *Phys. Rev. Mater.* **2021**, *5*, 095405.
[446] T. Gottschall, M. D. Kuz'min, K. P. Skokov, Y. Skourski, M. Fries, O. Gutfleisch, M. G. Zavareh, D. L. Schlagel, Y. Mudryk, V. Pecharsky, J. Wosnitza, *Phys. Rev. B* **2019**, *99*, 134429.
[447] L. Beyer, B. Weise, J. Freudenberger, J. K. Hufenbach, T. Gottschall, M. Krautz, *J. Magn. Magn. Mater.* **2021**, *536*, 168115.
[448] N. Maraytta, Y. Skourski, J. Voigt, K. Friese, M. G. Herrmann, J. Persson, J. Wosnitza, S. M. Salman, T. Brückel, *J. Alloy Compd.* **2019**, *805*, 1161.
[449] A. P. Kamantsev, A. A. Amirov, Y. S. Koshkid'ko, C. S. Mejía, A. V. Mashirov, A. M. Aliev, V. V. Koledov, V. G. Shavrov, *Phys Solid State+* **2020**, *62*, 160.
[450] M. Fries, T. Gottschall, F. Scheibel, L. Pfeuffer, K. P. Skokov, I. Skourski, M. Acet, M. Farle, J. Wosnitza, O. Gutfleisch, *J. Magn. Magn. Mater.* **2019**, *477*, 287.
[451] F. Q. Zhang, E. Bykov, T. Gottschall, N. van Dijk, E. Brück, *Phys. Rev. B* **2023**, *107*, 214431.

© 2024 Wiley-VCH GmbH

16146840, 0, Downloaded from https://onlinelibrary.wiley.com/doi/10.1002/aenm.202400369 by Tu Delft, Wiley Online Library on [08/04/2024]. See the Terms and Conditions (https://onlinelibrary.wiley.com/terms-and-conditions) on Wiley Online Library for rules of use; OA articles are governed by the applicable Creative Commons License

[452] M. G. Zavareh, Y. Skourski, K. P. Skokov, D. Y. Karpenkov, L. Zvyagina, A. Waske, D. Haskel, M. Zhernenkov, J. Wosnitza, O. Gutfleisch, *Phys. Rev. Appl.* **2017**, *8*, 014037.
[453] T. Gottschall, K. P. Skokov, F. Scheibel, M. Acet, M. G. Zavareh, Y. Skourski, J. Wosnitza, M. Farle, O. Gutfleisch, *Phys. Rev. Appl.* **2016**, *5*, 024013.
[454] C. Salazar-Mejía, V. Kumar, C. Felser, Y. Skourski, J. Wosnitza, A. K. Nayak, *Phys. Rev. Appl.* **2019**, *11*, 054006.
[455] C. Salazar-Mejía, P. Devi, S. Singh, C. Felser, J. Wosnitza, *Phys. Rev. Mater.* **2021**, *5*, 104406.
[456] F. R. de Boer, S. Begum, in *Reference Module in Materials Science and Materials Engineering*, Elsevier, Cham, Switzerland **2017**.
[457] I. Batashev, G. A. de Wijs, E. Brück, in *Handbook of Magnetic Materials*, Elsevier, Cham, Switzerland **2021**, Vol. *30*, p. 1.
[458] J. D. Bocarsly, E. E. Levin, C. A. C. Garcia, K. Schwennicke, S. D. Wilson, R. Seshadri, *Chem. Mater.* **2017**, *29*, 1613.
[459] C. A. C. Garcia, J. D. Bocarsly, R. Seshadri, *Phys. Rev. Mater.* **2020**, *4*, 024402.
[460] K. Hu, R. W. Xie, C. Shen, H. L. Peng, H. S. Liu, H. B. Zhang, *Acta Mater.* **2023**, *259*, 119255.
[461] B. Zhang, X. Q. Zheng, T. Y. Zhao, F. X. Hu, J. R. Sun, B. G. Shen, *Chinese Phys. B* **2018**, *27*, 067503.
[462] P. B. de Castro, K. Terashima, T. D. Yamamoto, Z. F. Hou, S. Iwasaki, R. Matsumoto, S. Adachi, Y. Saito, P. Song, H. Takeya, Y. Takano, *NPG Asia Mater.* **2020**, *12*, 35.
[463] C. J. Court, A. Jain, J. M. Cole, *Chem. Mater.* **2021**, *33*, 7217.
[464] R. M. C. Pinto, J. H. Belo, J. P. Araújo, D. J. Silva, *J. Magn. Magn. Mater.* **2022**, *562*, 169706.
[465] D. J. Silva, J. Ventura, J. P. Araújo, *Energy and AI* **2020**, *2*, 100030.
[466] A. Maiorino, M. G. D. Duca, U. Tomc, J. Tusek, A. Kitanovski, C. Aprea, *Appl. Therm. Eng.* **2021**, *197*, 117375.
[467] O. Chdil, M. Bikerouin, M. Balli, O. Mounkachi, *Appl. Energy* **2023**, *335*, 120773.
[468] T. DebRoy, H. L. Wei, J. S. Zuback, T. Mukherjee, J. W. Elmer, J. O. Milewski, A. M. Beese, A. Wilson-Heid, A. De, W. Zhang, *Prog. Mater. Sci.* **2018**, *92*, 112.
[469] H. L. Hou, E. Simsek, T. Ma, N. S. Johnson, S. X. Qian, C. Cissé, D. Stasak, N. Al Hasan, L. Zhou, Y. H. Hwang, R. Radermacher, V. I. Levitas, M. J. Kramer, M. A. Zaeem, A. P. Stebner, R. T. Ott, J. Cui, I. Takeuchi, *Science* **2019**, *366*, 1116.
[470] T. DebRoy, T. Mukherjee, H. L. Wei, J. W. Elmer, J. O. Milewski, *Nat. Rev. Mater.* **2021**, *6*, 48.

Ekkes Brück obtained his Ph.D. degree from Universiteit van Amsterdam (the Netherlands) in 1991, and he is a full professor at the Faculty of Applied Sciences at Delft University of Technology and head of the section FAME. His main research interest is in materials for renewable energy and energy saving (MCE, H storage, solar cells, self-healing materials, catalysts, Li-ion batteries). His major scientific effort and scholarly contribution of the past 25 years is to establish magnetocaloric material as a new, sustainability-oriented discipline. Overall, He has published more than 440 papers with more than 19190 citations (google citations); generated 13 patents.

Yang Ren received his Ph.D. in chemical physics from the University of Groningen, the Netherlands in 1996. He is currently a chair professor and head of the Department of Physics, City University of Hong Kong. He was a lead beam line scientist for a high-energy X-ray beamline at the Advanced Photon Source. His research interests focus on the structure-property relationship studies of materials by utilizing synchrotron X-ray and neutron scattering and other techniques. His research activities include investigations of phase transition, correlated electron systems, engineering materials, nanomaterials, energy storage (battery), and conversion materials. He has published more than 920 papers with more than 50599 citations (h-index = 114).

© 2024 Wiley-VCH GmbH

16146840, 0, Downloaded from https://onlinelibrary.wiley.com/doi/10.1002/aenm.202400369 by Tu Delft, Wiley Online Library on [08/04/2024]. See the Terms and Conditions (https://onlinelibrary.wiley.com/terms-and-conditions) on Wiley Online Library for rules of use; OA articles are governed by the applicable Creative Commons License